Integrated Optical Isolators

by

Tauhid R. Zaman

Submitted to the Department of Electrical Engineering and Computer Science
in partial fulfillment of the requirements for the degree of

Master of Engineering in Electrical Engineering and Computer Science

at the

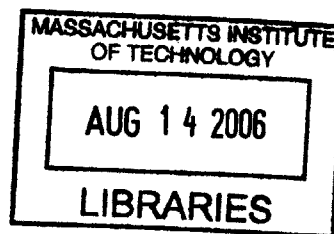MASSACHUSETTS INSTITUTE OF TECHNOLOGY

August 16, 2005

Author_____
Department of Elec............. ...g...... ....~....
                                                   .   . 1. ~~~

Certified by_____
                                                   ajeev Ram
                                                   Supervisor

Accepted by_____
                                                   ir C. Smith
Chairman, Department Committee on Graduate Theses

Integrated Optical Isolators

By

Tauhid R. Zaman

Submitted to the Department of Electrical Engineering and Computer Science

August 16, 2005

in partial fulfillment of the requirements for the degree of
Master of Engineering in Electrical Engineering and Computer Science

Abstract

Integrated optical isolators will become necessary as optical networks continue to grow and the need for monolithic integration and greater functionality increases. This thesis presents a design for a polarization independent isolator which can be monolithically integrated with semiconductor lasers. Theory and measurements are used to select a material for the isolator. A polarization independent design for the isolator is chosen with all components suitable for monolithic integration. Simulations of the isolator show it to be capable of 24 dB of isolation. Waveguide Faraday rotators, which are a component of the isolator, are fabricated and demonstrated.

Thesis Supervisor: Rajeev J. Ram
Title: Associate Professor

Acknowledgments

Thanks to my parents for always supporting me. I would like to especially thank my mother who never stopped believing in me. Also, thanks to my brother Robbie. It's good to have you in Boston and I look forward to the next four years.

Finally, I would like to thank my grandparents for raising me and showing me so much love. You two have been and always will be a driving force in my life and I would not be where I am today if it were not for the two of you. I love you both and will always appreciate what you have done for me.

Contents

List of Figures

List of Tables

Chapter 1

Introduction

Optical isolators are important components in lasers. Their main function is to eliminate noise caused by back-reflections into these lasers. The need for integrated isolators comes from the continuing growth of telecommunication networks. Monolithic integration of isolators with other optical components such as lasers would reduce costs and increase functionality.

This thesis presents the design and test of a monolithically integrated optical isolator for telecommunication networks. This chapter will begin with an explanation of how isolators actually eliminate noise in lasers and then it will then show how commercial bulk isolators function. Next, greater detail will be provided on the need for monolithically integrated isolators. Because isolators are non-reciprocal devices, they must use a non-reciprocal effect in order to function. A brief description of this phenomenon, known as Faraday rotation, will be given in this chapter. Then previous work on integrated isolators will be presented. Finally, an overview of this thesis will be given.

1.1 Motivation

1.1.1 Laser Noise Due to Back-Reflections

An optical isolator is a non-reciprocal device which allows light propagation in only one direction. It is used to prevent optical feedback in lasers and optical amplifiers. This is important because feedback can cause noise and instabilities in lasers. In semiconductor lasers used for telecommunications, the feedback is caused by back-

reflections from optical fiber at the laser output. The effect of the reflecting fiber facet is to create a double cavity state in the laser if phase coherence is maintained, or to act as an external light source if coherence is lost.

There will be fluctuations in laser intensity and frequency for both the double cavity state and external light source state. For the double cavity state, the fluctuations are due to mechanical vibrations of the fiber which change the length from the reflection point to the cavity and create phase variations. For the external light source, the fluctuations come from the random generation of locking and unlocking states due to the frequency changes caused by temperature variations of the laser diode. In either case, the intensity and frequency noise are both directly proportional to the effective reflectivity of the fiber [1]. Here effective reflectivity refers to the amount of reflected power from the fiber that actually returns to the laser cavity.

To reduce the effective reflectivity, an isolator is placed in front of the laser. The isolator will block the back-reflected light, thus reducing the intensity and frequency fluctuations. The name isolator comes from the fact that if it is placed in front of a port, then it will isolate this port from any optical power propagating towards it. Isolators are essential for any sort of laser where low noise is desired.

1.1.2 Commerical Bulk Isolators

Because isolators only allow light propagation in one direction, they are non-reciprocal devices, and therefore must utilize a non-reciprocal phenomenon in order to function. The phenomenon used in commercial bulk isolators is Faraday rotation. This is a non-reciprocal rotation of the polarization of light. It is non-reciprocal in the sense that the rotation is independent of the direction of light propagation. If light propagates through a Faraday rotating medium, after a single pass its polarization is rotated by an angle θ, and after a round-trip it is rotated by 2θ.

To use this effect in an isolator, a Faraday rotator is placed in between two polarizers, as shown in Figure 1-1. The polarizers are oriented at 45° with respect to each other. In the forward direction, light will pass through the first polarizer, be rotated 45° by the Faraday rotator, and pass through the second polarizer unattenuated. In the reverse

direction, the light will pass through the second polarizer, be rotated 45° in the same direction, and be blocked by the first polarizer. In this way isolation can be achieved. However, this design is not polarization independent. If the input light is oriented orthogonal to the first polarizer, there will be no transmission.
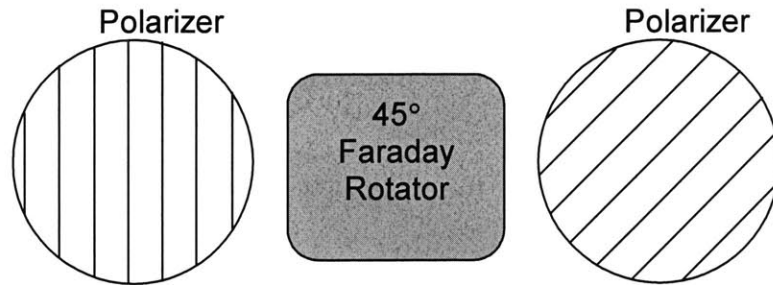
Figure 1-1: Polarization dependent bulk isolator consisting of polarizers and a Faraday rotator

Polarization independent isolators can be achieved by using birefringent walk-off plates (BWP). The basic configuration is shown in Figure 1-2. The walk-off plate separates the transverse magnetic (TM) and transverse electric (TE) polarizations. TM polarization is vertical, and TE is horizontal. The TM light is transmitted straight through, and the TE light is transmitted away from the normal of the beam splitter. In the forward direction, the light passes through the first beam-splitter, then through a Faraday rotator and half-wave plate, and finally a second beam splitter. The Faraday rotator provides a non-reciprocal 45° rotation and the half-wave plate provides a reciprocal 45° rotation. The combined effect of the non-reciprocal and reciprocal rotation transforms the TM light into TE and the TE light into TM. At the second walk-off plate, the TE is bent away from the normal and the TM passes straight through, and both beams combine at a common output. The input light thus reaches the output without attenuation. In the reverse direction, the sequence of half-wave plate and Faraday rotator leave the TE and TM light unaltered. At the first walk-off plate, the two polarizations exit at separate ports, and the input port is isolated.

BWP   BWP
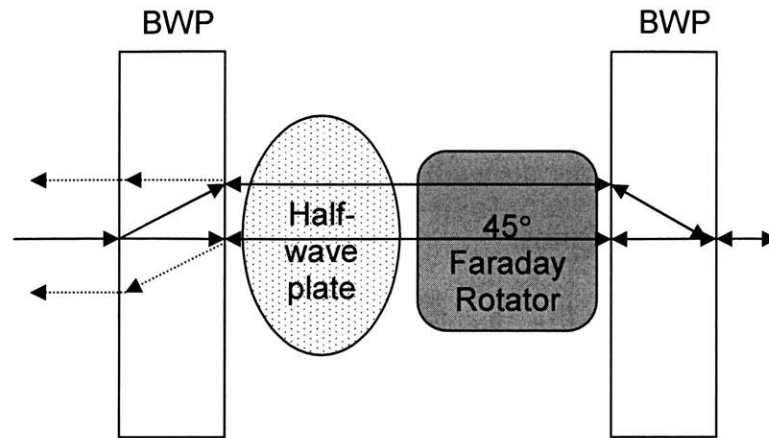
Figure 1-2: Polarization independent isolator consisting of a half-wave plate, Faraday rotator, and birefringent walk-off plates (BWP)

1.1.3 Need for Integrated Isolators

For optical communications, semiconductor lasers are used with an external isolator. Figure 1-3 shows a distributed feedback laser in a butterfly package. This isolator consists of two polarizers, a Faraday rotator, and an external magnet to bias the Faraday rotator. These components are not in integrated form with the isolator, which is the largest element in the laser package.
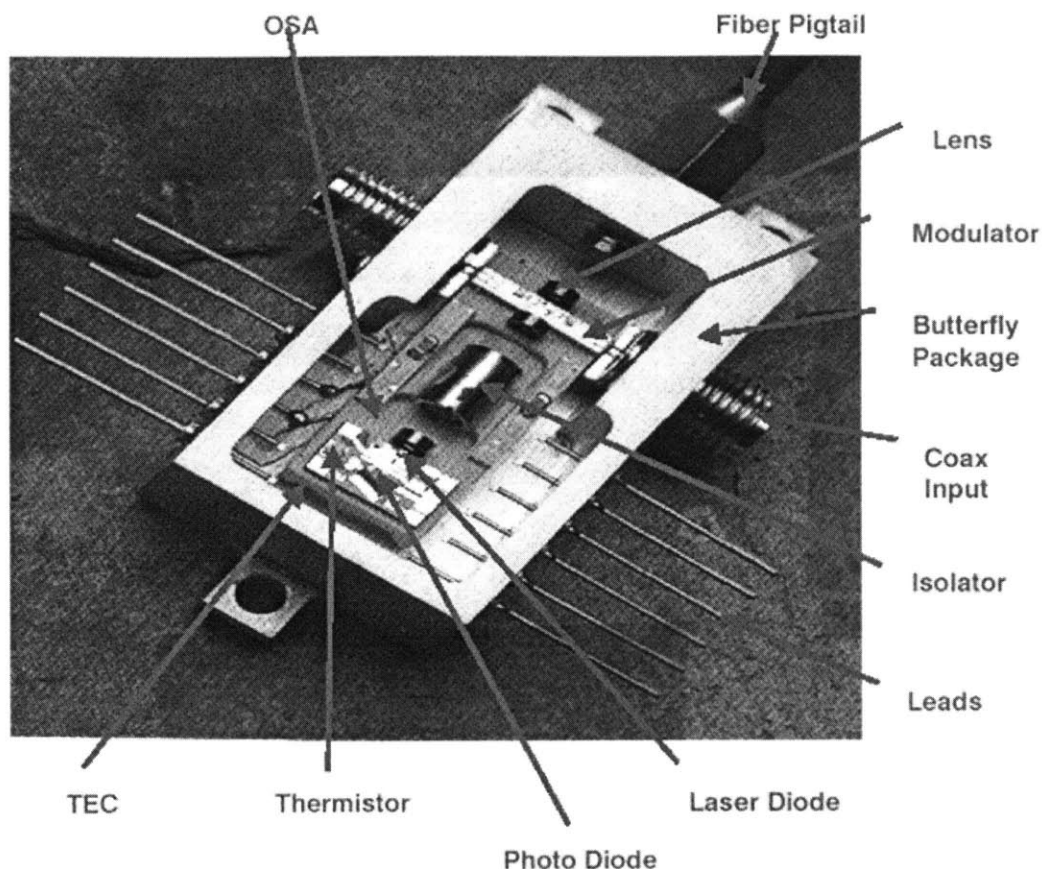
Figure 1-3: Laser package with isolator

The motivation for integrated isolators comes from the growth in optical networks. As networks become larger and more complex, greater integration of optical functions is needed in order to increase capacity while also reducing costs. An integrated isolator would have several benefits. First, it would reduce the size of the laser package and allow for several lasers to be integrated with isolators on a single chip. This would be especially useful for wavelength division multiplexed (WDM) optical networks where several different wavelengths are used to transmit information. Second, an integrated isolator would eliminate the costs associated with alignment of a separate optical component. Third, it would increase mechanical stability because it would be integrated on the same semiconductor chip as the laser.

Another technology which would require integrated optical isolators is all-optical networks. The motivation for this type of network is the need for higher network speeds.

Current communication networks use electronics to process information contained in optical data packets in order to determine their destination. Optical-networks aim to do this in the optical domain using optical switches. Research is currently being done on using semiconductor optical amplifiers (SOA) for these switches [2].

A possible optical circuit that performs a logical function in these all-optical networks is shown in Figure 1-4. This circuit consists of two stages of optical SOA switches. In order to function properly, each switch stage must be buffered so that an individual stage's function is not corrupted by noise from other stages. The main noise sources would be amplified spontaneous emission from the SOA's and any sort of back-reflection between stages. If a circuit consisted of several stages, then an isolator would be required for each switch in each stage. The circuit would become very expensive, large, and difficult to fabricate if each isolator was a separate bulk component. For this type of circuit to be practical for all-optical networks, it is essential that the isolators are in integrated form.
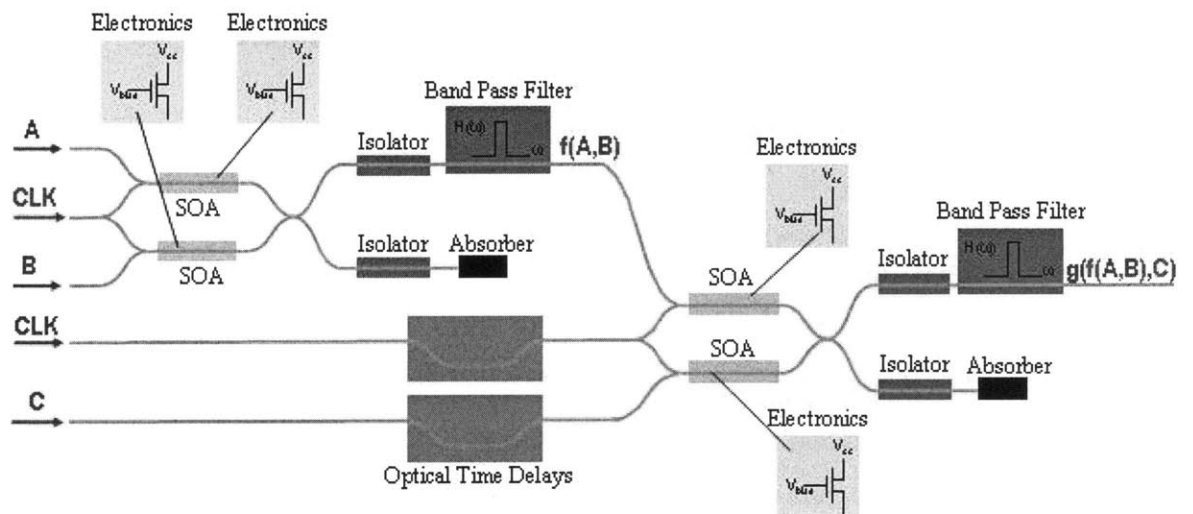
Figure 1-4: Circuit consisting of all optical SOA switches. Isolators are needed to buffer different stages of the circuit [2]

1.2 Introduction to Faraday rotation

1.2.1 Faraday Rotation from an Asymmetric Dielectric Tensor

When a magnetic field is applied in the z direction, the dielectric tensor for a material has the form

$$\overline{\overline{\varepsilon}} = \varepsilon_o \begin{bmatrix} n^2 & j\varepsilon_{xy} & 0 \\ -j\varepsilon_{xy} & n^2 & 0 \\ 0 & 0 & n^2 \end{bmatrix} \tag{1.1}$$

where n is the index of refraction and ε_{xy} is purely real. The next section discusses the physical origin of this dielectric tensor. By inserting the above expression for ε into Maxwell's equations for a source free region, one obtains

$$\nabla \bullet \overline{\overline{\varepsilon}}\overline{E} = 0 \tag{1.2}$$

$$\nabla \bullet \mu\overline{H} = 0 \tag{1.3}$$

$$\nabla \times \overline{E} = -j\omega\mu\overline{H} \tag{1.4}$$

$$\nabla \times \overline{H} = j\omega\overline{\overline{\varepsilon}}\overline{E} \tag{1.5}$$

A time harmonic dependence $e^{j\omega t}$ has been assumed in the above equations. By using the well known vector identity

$$\nabla \times \nabla \times \overline{A} = \nabla(\nabla \bullet \overline{A}) - \nabla^2\overline{A} \tag{1.6}$$

Maxwell's equations can be rewritten as

$$\nabla^2\overline{E} + \omega^2\mu\overline{\overline{\varepsilon}}\overline{E} = 0 \tag{1.7}$$

Assuming that **E** has the form $\mathbf{E}_oe^{j(\omega t-\beta z)}$, equation 3-1 becomes an eigenvalue problem:

$$\frac{\omega^2}{c^2}\begin{bmatrix} n^2 & j\varepsilon_{xy} & 0 \\ -j\varepsilon_{xy} & n^2 & 0 \\ 0 & 0 & n^2 \end{bmatrix}\begin{bmatrix} E_x \\ E_y \\ E_z \end{bmatrix} = \beta^2\begin{bmatrix} E_x \\ E_y \\ E_z \end{bmatrix} \tag{1.8}$$

Here c is the speed of light in vaccum and is equal to $1/(\mu_o\varepsilon_o)^{1/2}$. The eigenvectors and eigenvalues of Equation 1.8 fall into two categories. First, the z-component of the electric field is considered. Because it has been assumed that propagation is also in the z direction and that the material is source free, the solution is trivial:

$$\overline{E} = \begin{bmatrix} 0 \\ 0 \\ 1 \end{bmatrix}, \beta = 0 \qquad (1.9)$$

However, for the other two solutions, the eigenvectors correspond to right- and left-circularly polarized light written as E_+ and E_-, with propagation constants β_+ and β_-:

$$\overline{E_\pm} = \begin{bmatrix} 1 \\ \mu j \\ 0 \end{bmatrix}, \beta_\pm = \frac{\omega}{c}\sqrt{(n^2 \mu \varepsilon_{xy})} \qquad (1.10)$$

For isotropic, reciprocal materials, right and left circular polarizations are degenerate and have the same propagation constant. Because the phase velocity is given by ω/β, these two polarizations propagate at the same speed in isotropic, reciprocal materials. However, in a non-reciprocal material which exhibits Faraday rotation, these two polarizations are no longer degenerate and propagate at different speeds. Consider x polarized light incident on a Faraday rotating material. The light will couple to the two circular polarizations:

$$\overline{E_i} = \begin{bmatrix} E_o \\ 0 \\ 0 \end{bmatrix} = \frac{E_o}{\sqrt{2}}\left(\begin{bmatrix} 1 \\ -j \\ 0 \end{bmatrix} + \begin{bmatrix} 1 \\ j \\ 0 \end{bmatrix}\right) \qquad (1.11)$$

After propagating a distance l, the field becomes

$$\overline{E(l)} = \frac{E_o}{\sqrt{2}}\left(\begin{bmatrix} 1 \\ j \\ 0 \end{bmatrix}e^{j\beta_- l} + \begin{bmatrix} 1 \\ -j \\ 0 \end{bmatrix}e^{j\beta_+ l}\right) \qquad (1.12)$$

At this point a simplifying assumption is made: because ε_{xy} is much smaller than n^2, β is rewritten as a first order Taylor expansion:

$$\beta_\pm = \frac{\omega}{c}\left(n \mu \frac{\varepsilon_{xy}}{2n}\right) \qquad (1.13)$$

Equation 1.12 can then be rewritten as

$$\overline{E(l)} = \frac{E_o e^{j\phi}}{\sqrt{2}} \left(\begin{bmatrix} 1 \\ j \\ 0 \end{bmatrix} e^{-j\delta} + \begin{bmatrix} 1 \\ -j \\ 0 \end{bmatrix} e^{j\delta} \right) \tag{1.14}$$

where

$$\phi = \frac{\beta_+ + \beta_-}{2} l = \frac{\omega}{c} n l \tag{1.15}$$

$$\delta = \frac{\beta_+ - \beta_-}{2} l = -\frac{\omega}{c} \frac{\varepsilon_{xy}}{2n} l \tag{1.16}$$

By dropping common phase factors, Equation 1.14 becomes

$$\overline{E(l)} = E_o \left(\begin{bmatrix} 1 \\ 0 \\ 0 \end{bmatrix} \cos(\delta) + \begin{bmatrix} 0 \\ 1 \\ 0 \end{bmatrix} \sin(\delta) \right) \tag{1.17}$$

As can be seen, the polarization now has an x component of magnitude $\cos(\delta)$ and a y component of magnitude $\sin(\delta)$. This is just the input polarization rotated by an angle δ, which corresponds to the Faraday rotation. The Verdet coefficient V, which is the specific rotation per length, can be written as

$$V = \frac{\beta_+ - \beta_-}{2} = -\frac{\omega}{c} \frac{\varepsilon_{xy}}{2n} \tag{1.18}$$

1.2.2 Classical Theory of Faraday Rotation

To understand the origins of the asymmetric dielectric tensor, it is easiest to consider a single electron bound to a nucleus. The displacement r of the electron from its equilibrium position is assumed to be small, so the nuclear potential is approximated by a harmonic oscillator with oscillation frequency ω_0. If an electromagnetic field is incident on the atom, then the equation of motion for the electron is

$$m_e \frac{d^2 \overline{r}}{dt} = -m_e \omega_o^2 \overline{r} - \gamma \frac{d\overline{r}}{dt} + q\overline{E} \tag{1.19}$$

where q is the electron charge, γ is the damping constant, and m_e is the electron mass. In the above equation, the force due to the photon's magnetic field is assumed to me much

smaller than that of the electric field, and is therefore neglected. If an external magnetic field **B** is applied to the atom, the equation of motion for the electron will become:

$$m_e \frac{d^2 \bar{r}}{dt^2} = -m_e \omega_o^2 \bar{r} - \gamma \frac{d\bar{r}}{dt} + q \left(\bar{E} + \frac{d\bar{r}}{dt} \times \bar{B} \right)$$

(1.20)

If **r** is assumed to have the same $e^{j\omega t}$ time harmonic form as **E**, then Equation 1.20 can be rewritten as:

$$-m_e \omega^2 \bar{r} = -m_e \omega_o^2 \bar{r} - j\omega\gamma\bar{r} + q \left(\bar{E} + j\omega\bar{r} \times \bar{B} \right)$$

(1.21)

The polarization of a material is defined as

$$\bar{P} = qN_e \bar{r} = \bar{\bar{\varepsilon}}\bar{E}$$

(1.22)

where N_e is the electron volume density in the material, and ε is the dielectric tensor of the material. The dielectric tensor is defined here as

$$\bar{\bar{\varepsilon}} = \varepsilon_o \begin{bmatrix} n^2 & \varepsilon_{xy} & \varepsilon_{xz} \\ \varepsilon_{yx} & n^2 & \varepsilon_{yz} \\ \varepsilon_{zx} & \varepsilon_{zy} & n^2 \end{bmatrix}$$

(1.23)

If this is inserted into Equation 1.21 the result is

$$\left(m \left(\omega_o^2 - \omega^2 \right) + j\omega\gamma \right)\bar{\bar{\varepsilon}}\bar{E} = q^2 N_e \bar{E} + j\omega q \left(\bar{\bar{\varepsilon}}\bar{E} \times \bar{B} \right)$$

(1.24)

For simplicity it is now assumed that **B** is in the z direction. Then all off diagonal terms in ε become 0 except for ε_{xy} and ε_{yx}. The expressions for the remaining terms in ε are then

$$n^2 = \frac{N_e q^2}{\varepsilon_o} \frac{m^* \left(\omega_o^2 - \omega^2 \right) + j\omega\gamma}{\left(m^* \left(\omega_o^2 - \omega^2 \right) + j\omega\gamma \right)^2 - \left(\omega q B_z \right)^2}$$

(1.25)

$$\varepsilon_{xy} = \varepsilon_{yx}^* = \frac{j\omega N_e q^3 B_z}{\varepsilon_o \left(m^* \left(\omega_o^2 - \omega^2 \right) + j\omega\gamma \right)^2 - \left(\omega q B_z \right)^2}$$

(1.26)

The off-diagonal elements are complex as defined here, but to match the convention used in Section 1.2.1, they are redefined such that

$$j\varepsilon_{xy} = -j\varepsilon_{yx} = \frac{\omega N_e q^3 B_z}{\varepsilon_o \left(m^* \left(\omega_o^2 - \omega^2 \right) + j\omega\gamma \right)^2 - \left(\omega q B_z \right)^2}$$

(1.27)

The important feature to note for the dielectric tensor is that the off-diagonal terms have opposite sign. This causes ε to be a non-symmetric tensor, which breaks reciprocity in

the material. The off-diagonal terms are proportional to the magnetic field, and are responsible for the Faraday rotation. If the magnetic field changes sign, ε_{xy} will change sign, which will cause the Faraday rotation to be in the opposite direction.

For a more physical picture of the Faraday rotation, the effects of the forces on the electron are considered. The nuclear potential binding the electron to the nucleus can be modeled as a spring. The incident electromagnetic field E_i will cause the electron to oscillate with velocity v, and the magnetic field B will apply a transverse force on the electron, causing it to rotate. The radiated light will have its polarization aligned with the electronic oscillation. As the electron's oscillation direction is rotated, so is the polarization of the light it radiates. Because the force only depends on the direction of E and B, the magnetic force will be the same irrespective of the propagation direction. If light propagating in the forward direction has its polarization rotated by an angle θ, then after one round-trip, it will be rotated by 2θ and will not be in its initial polarization state. Thus, it can be seen how the magnetic field breaks reciprocity.

1.3 Previous Work on Integrated Isolators

1.3.1 Introduction

There have been two main approaches to achieving integrated optical isolators. The first approach utilizes a magnetic field applied transverse to the direction of propagation, and the second approach utilizes a magnetic field applied parallel to the direction of propagation. Two phenomena fall into former approach: non-reciprocal phase shift (NRPS) and non-reciprocal loss (NRL). The phenomenon used for the latter approach is Faraday rotation. Each approach has its own advantages and disadvantages, which are discussed in the following sections.

1.3.2 Non-Reciprocal Phase Shift (NRPS)

For NRPS, the magnetic field is applied transverse to the direction of propagation, as shown in Figure 1-5.
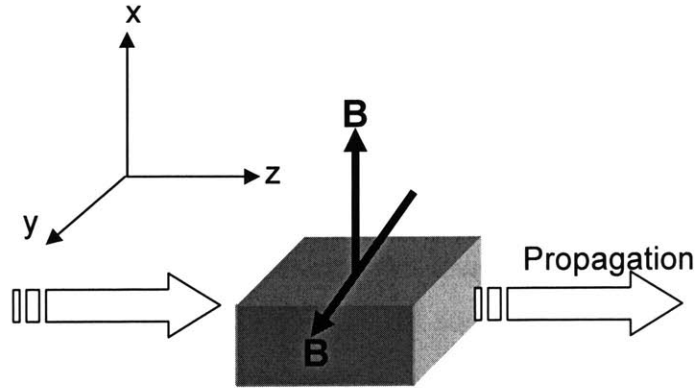
Figure 1-5: Configuration for NRPS. The magnetic field **B** is applied transverse to the direction of propagation

A magnetic field applied in the y direction will give a dielectric tensor of the form [3]

$$\overline{\overline{\varepsilon}} = \varepsilon_o \begin{bmatrix} n^2 & 0 & j\varepsilon_{xz} \\ 0 & n^2 & 0 \\ -j\varepsilon_{xz} & 0 & n^2 \end{bmatrix} \tag{1.28}$$

while a magnetic field applied in the x direction will give:

$$\overline{\overline{\varepsilon}} = \varepsilon_o \begin{bmatrix} n^2 & 0 & 0 \\ 0 & n^2 & j\varepsilon_{yz} \\ 0 & -j\varepsilon_{yz} & n^2 \end{bmatrix} \tag{1.29}$$

The NRPS is a waveguide effect, occurring because of the coupling of transverse and longitudinal field components. Waveguide modes can be divided into two types: transverse electric (TE) and transverse magnetic (TM). TE modes are dominated by an electric field in the y direction and have a negligible x component. The dominant electric field component for TM modes is in the x direction, with the y component being negligible.

The effect of the off-diagonal elements is to create different propagation constants for the forward and reverse directions. Perturbation theory can be used to calculate the difference between the forward and reverse propagation constants [4]:

$$\delta\beta_{TM} = j2\omega\varepsilon_o\varepsilon_{xz} \iint E_x^* E_z dxdy \quad \text{(TM)} \qquad (1.30)$$

$$\delta\beta_{TE} = j2\omega\varepsilon_o\varepsilon_{yz} \iint E_y^* E_z dxdy \quad \text{(TE)} \qquad (1.31)$$

where all field components are normalized to the power flow along the propagation direction. This non-reciprocal propagation constant can be used to provide a different phase for the forward and reverse direction.

To make an isolator using NRPS, a Mach-Zender configuration is used. The NRPS waveguide is placed in one arm of the isolator, and a reciprocal waveguide in the other. In the forward direction, light propagating through the two arms will be in phase at the output and interfere constructively, traveling through the output port. In the reverse direction, the two arms will be 180° out of phase due to the NRPS. Reverse propagating light will interfere destructively and not be transmitted through the input port, thus achieving isolation.
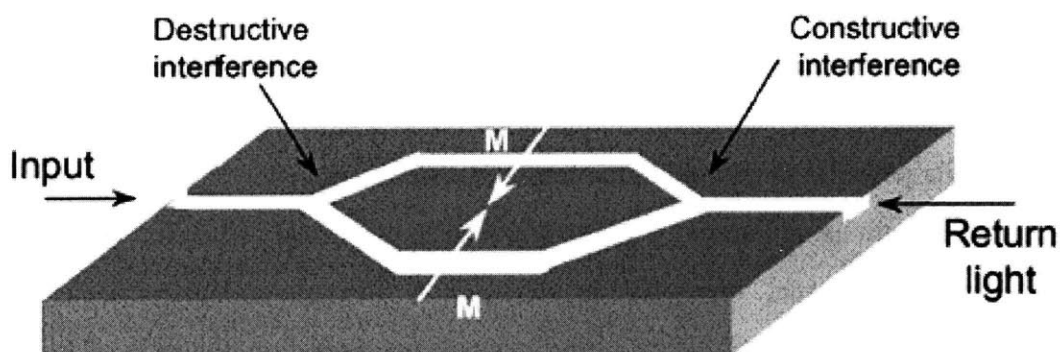
Figure 1-6: NRPS isolator in magnetic garnets. By applying opposite magnetic fields in each arm, only a 90° NRPS is required [5]

NRPS isolators with 18 dB isolation have been achieved in magnetic garnets [5]. The isolator only functioned for TM polarizations because the applied magnetic field was

applied in the horizontal direction. A diagram of the isolator is shown in Figure 1-6. It had a NRPS waveguide in each arm with opposite magnetization. Two electromagnets provided the external magnetic fields. This required the magnitude of $\delta\beta$ to only be 90° instead of 180° in each arm. This isolator is 8 mm long, with NRPS waveguides which are 3.3 mm long. The NRPS waveguides are made from a bismuth-, lutetium-, and neodymium-iron garnet film $(Bi,Lu,Nd)_3(Fe,Al)_5O_{12}$.

NRPS can also be achieved for both TM and TE polarizations by applying an external magnetic field at 45° to achieve in-plane and out-of-plane magnetizations [4]. This technique could be used to make polarization independent NRPS isolators.

NRPS attracted attention because unlike Faraday rotation, it did not have the strict phase matching requirements for the TE and TM modes, which will be discussed in a later section. The main disadvantage of NRPS when compared to Faraday rotation is that it is an inherently weaker effect. Using Equation 1.18, the Verdet coefficient for a Faraday rotator can be expressed as

$$V = \frac{\omega}{c} \frac{\varepsilon_{xy}}{2n}$$ (1.32)

The ratio of the NRPS to the Verdet coefficient is then

$$\left|\frac{\delta\beta_{TM}}{V}\right| = \left|j4c\varepsilon_o n \iint E_x E_z dx dy\right|$$ (1.33)

This ratio is proportional to the normalized overlap integral of the transverse and longitudinal electric field components. This integral is much less than 1 because most of the mode power is contained in the transverse field component. To see the difference in isolator length using Faraday rotation and NRPS, numerical values for V and $\delta\beta$ are used for a magnetic garnet waveguide in reference 4. Because an isolator needs either a 45° Faraday rotation or a 90° NRPS in the balanced configuration, the ratio of the length of a NRPS isolator to a Faraday rotator isolator for the material in reference 4 is

$$\frac{L_{NRPS}}{L_{FR}} = \frac{\dfrac{90}{\delta\beta}}{\dfrac{45}{V}} = \frac{1.85}{0.05} = 38.4$$ (1.34)

As can be seen, using Faraday rotation can reduce the isolator length by an order of magnitude.

1.3.3 Non-Reciprocal Loss (NRL)

In the derivation of the NRPS, it was assumed that the off diagonal elements (ε_{ij}) in the permittivity tensor were purely real, leading to only a change in the real part of the propagation constant, which corresponded to a phase shift. However, if this term were to have an imaginary component, then the imaginary part of the propagation constant would be changed. This would lead to different loss in the forward and reverse directions. By incorporating this effect with an optical gain medium, such as a semiconductor optical amplifier (SOA), an isolator can be made. If the gain is adjusted appropriately, the loss in the forward direction can be compensated, while the loss in the reverse direction will still be large enough to attenuate any reverse propagating light.

NRL isolators have been made by placing an absorbing magnetic layer on top of an SOA, as shown in Figure 1-7 [6]. This isolator showed a theoretical isolation of 119 dB/cm for the TM mode. The best experimentally demonstrated NRL isolators to date can provide isolations of 32 dB/cm [7]. The advantage of NRL isolators is that they do not need to be placed in Mach-Zehnder configurations in order to function. A second advantage is that the maximum possible isolation is only limited by the device length. This allows for incredibly high isolations to be achieved.
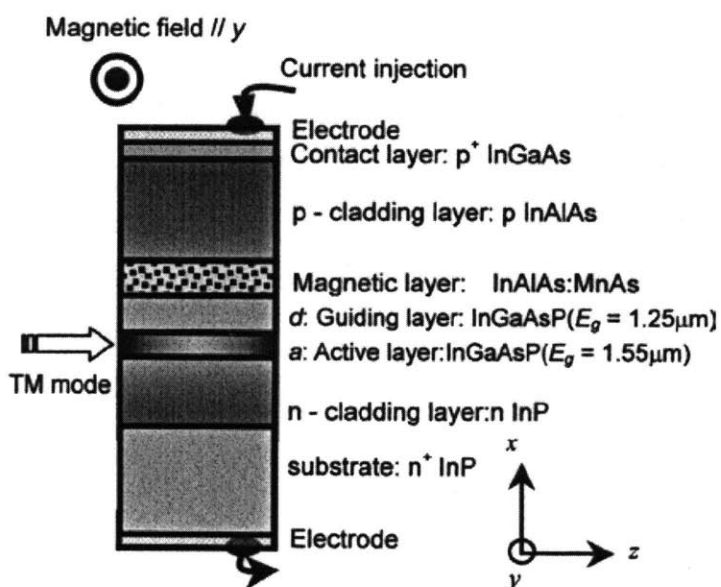
Figure 1-7: NRL isolator made using SOA and a magnetic absorbing layer [6]

While the prospect of a simple makes NRL isolators seem very attractive, there is one important disadvantage. Because the optical mode penetrates into the absorbing magneto-optic layer, the insertion loss is large. The NRL is proportional to the overlap of the mode with the magneto-optic layer, but so is the loss. An SOA must be used just to compensate for this reciprocal loss. For example, a one-dimensional simulation of an SOA covered with a ferromagnetic layer has shown that a material gain of 1560 cm^{-1} is needed to provide unity gain in the forward direction for a NRL isolator [8]. Any practical NRL isolator must therefore be an active device. A passive isolator would be preferable because it would not have any power consumption. Also, when using SOA's, spontaneous emission will be present, which may not all be absorbed by the NRL isolator, further degrading its performance.

1.3.4 Faraday Rotation

As already discussed, Faraday rotation is used to make bulk optical isolators. However, for waveguide structures, Faraday rotation is more difficult to utilize because of the strict phase-matching conditions. However, if this phase-matching condition can be achieved, the Faraday rotation could be used to make isolators which are an order of magnitude smaller than NRPS and NRL isolators.

Waveguide Faraday rotation has been demonstrated in magnetic garnets [9]. Figure 1-8 shows the Faraday rotation for a magnetic garnet, a high birefringence waveguide, and a low birefringence waveguide. As the length of the Faraday rotator is increased, the high birefringence waveguide's Faraday rotation oscillates, while the bulk sample and low birefringence waveguides show a monotonic increase in their Faraday rotation. Thus, by reducing the birefringence of the waveguide, the Faraday rotation approached its maximum value.
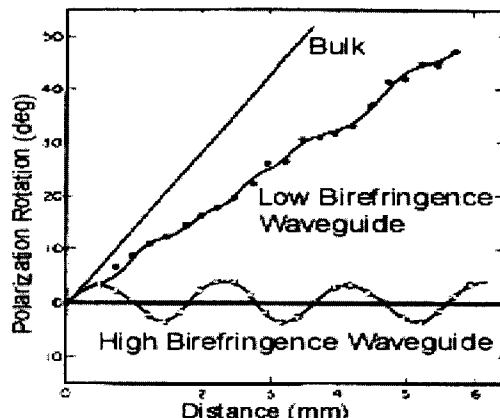
Figure 1-8: Faraday rotation vs. length for three different magnetic garnet samples: a bulk sample, a high birefringence waveguide, and a low birefringence waveguide [9]

Isolators have been achieved with waveguide Faraday rotators and external bulk polarizers [10]. However, a fully integrated isolator has not been demonstrated using Faraday rotation because polarizers and polarizing beam splitters are difficult to achieve in waveguide form.

1.4   Integrated Optical Isolator Design

Conventional isolators use Faraday rotators and bulk polarizers to achieve isolation. Polarizers set at arbitrary angles are difficult to achieve in waveguide form, so a practical integrated isolator design must not contain polarizers. Such a design was created by Sugimoto et. al [11], which also functioned as an optical circulator. The isolator, which is shown in Figure 1-9, is a four port device and consisted of waveguide Faraday rotators, waveguide 3 dB couplers, and thin film polymer half-wave plates in a Mach-Zehnder configuration. The Faraday rotators in the isolator provide a 45° Faraday rotation. The two half-wave plates in the isolator have their slow axis oriented at 22.5° and -22.5° with respect the horizontal, thus providing a reciprocal 45° rotation.
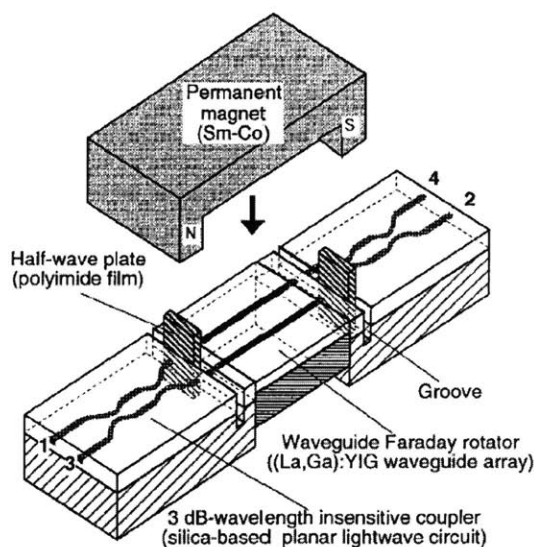
Figure 1-9: Optical isolator consisting of 3 dB couplers, half-wave plates, and Faraday rotators [11]

The advantage of this design is that it achieves isolation with a Faraday rotator without using any polarizers. The entire device was 47 mm in length. Most of this length was dominated by the 3 dB couplers, each of which had a length of 22 mm. The waveguide Faraday rotators, which were made of a lanthamum- and gallium-substituted yttrium iron garnet [(La,Ga):YIG], were 3 mm long. The Faraday rotators were biased by a thin-plate type Sm-Co permanent magnet which was 6 mm long. The applied magnetic field was 18 mT. The half-wave plates were made of 20 µm polyimide films which were inserted into grooves formed on the 3 dB couplers.

Figure 1-10 shows how TE and TM polarizations change as they propagate through the isolator. HWP1 and HWP2 refer to the half-wave plates with slow-axes oriented at 22.5° and -22.5°, respectively. The arrows represent the polarization state, with the black arrows representing TM inputs and the white arrows representing TE inputs. As can be seen, for forward propagation, the polarizations are in phase at the output, but for reverse propagation they are out of phase.
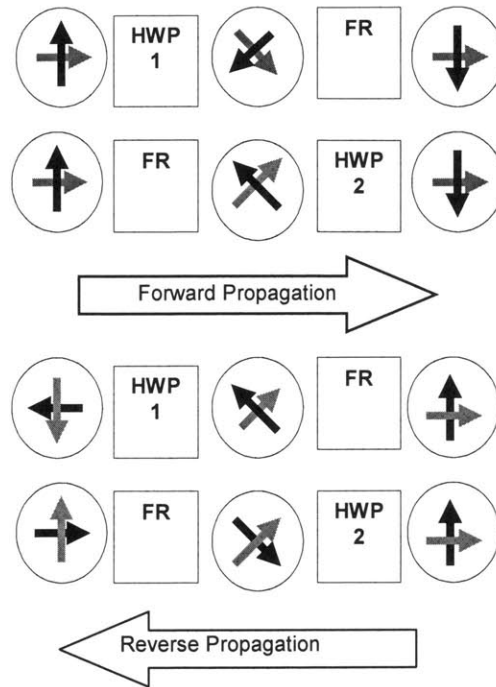
Figure 1-10: Polarization state of TE and TM inputs as they propagate through isolator

To understand how this design works, the Jones matrix formalism is used. A basic tutorial on Jones matrices can be found in Appendix A. For light traveling in the forward direction, the Jones matrices for the two arms can be expressed as:

$$A_1 = HWP1 * FR = \frac{1}{2}\begin{bmatrix} 1 & 1 \\ 1 & -1 \end{bmatrix}\begin{bmatrix} 1 & -1 \\ 1 & 1 \end{bmatrix} = \begin{bmatrix} 1 & 0 \\ 0 & -1 \end{bmatrix} \tag{1.35}$$

$$A_2 = FR * HWP2 = \frac{1}{2}\begin{bmatrix} 1 & -1 \\ 1 & 1 \end{bmatrix}\begin{bmatrix} 1 & -1 \\ -1 & -1 \end{bmatrix} = \begin{bmatrix} 1 & 0 \\ 0 & -1 \end{bmatrix} \tag{1.36}$$

Forward propagating light in the two arms will be in phase and interfere constructively. In the reverse direction, the Jones matrices for the two arms become:

$$A_1 = FR * HWP1 = \frac{1}{2}\begin{bmatrix} 1 & -1 \\ 1 & 1 \end{bmatrix}\begin{bmatrix} 1 & 1 \\ 1 & -1 \end{bmatrix} = \begin{bmatrix} 0 & 1 \\ 1 & 0 \end{bmatrix} \tag{1.37}$$

$$A_2 = HWP2 * FR = \frac{1}{2}\begin{bmatrix} 1 & -1 \\ -1 & -1 \end{bmatrix}\begin{bmatrix} 1 & -1 \\ 1 & 1 \end{bmatrix} = \begin{bmatrix} 0 & -1 \\ -1 & 0 \end{bmatrix} \tag{1.38}$$

Reverse propagating light in the two arms will be out of phase and interfere destructively. It is important to note here that the isolator functions for either TE or TM inputs. It is

polarization independent because any input can be represented as a linear combination of TE and TM polarizations.

The 3 dB couplers will switch the light depending on the phase: light from port 1 will exit at port 2, port 2 to port 3, port 3 to port 4, and port 4 to port 1. By only utilizing two ports, the device will act as an isolator. If all four ports are used, then it will act as a circulator.

Because the circulator used mirco-optic components on a silicon optical bench, it was not monolithically integrated. However, if all of the individual components (3 dB coupler, Faraday rotator, and half-wave plate) are in waveguide form, then this design will be ideal for an integrated optical isolator. Therefore, this design will be used in this thesis for the integrated isolator.

1.5 Thesis Overview

This thesis deals with the design and fabrication of an integrated optical isolator. The first step to making an integrated isolator is to select a design, which has been accomplished in this chapter. Also, in this chapter, it has been argued why it is best to use Faraday rotation as the non-reciprocal effect for the isolator.

Chapter 2 will study Faraday rotation in semiconductors. In this chapter a different approach will be introduced to explain Faraday rotation. This approach will be extended to understand the contributions to Faraday rotation from magnetic dopants and interband transitions in semiconductors. Data will be presented on Faraday rotation in several different materials. Finally, based on this theory and data, a material will be selected for the integrated isolator.

Chapter 3 will go into the details of the design of the integrated isolator. Analysis will be done to determine the limits on isolation and also fabrication tolerances for the device. Finally, simulation results on the isolator performance will be presented.

Measurement and characterization of the waveguide Faraday rotator will be the topic of Chapter 4. The experimental setup for characterization of the Faraday rotator will be described in detail. Data on the optical loss, birefringence, and Faraday rotation of the waveguides will be presented.

Chapter 5 will summarize the results of this thesis and evaluates the progress made towards the realization of an integrated optical isolator thus far. The chapter concludes with a discussion of future work to be done in the design and fabrication of an integrated optical isolator.

Chapter 2

Faraday Rotation in Semiconductors

To make an integrated isolator, a material is needed which can be monolithically integrated with semiconductor lasers. Commercial isolators are made from magnetic garnets such as YIG (yttrium iron garnet). These garnets are ideal for isolators because they have a high Verdet coefficient and low absorption. However, the problem with magnetic garnets is that they cannot be grown on common semiconductor substrates such as InP. Integration of an isolator with a semiconductor laser would be possible if a semiconductor could be used for the isolator material.

In order for a material to be used for an isolator, it must meet one important criterion: it must be able to provide a large Faraday rotation while also having minimal optical loss. Specifically, for the isolator design in this thesis, the material must be able to provide 45° of rotation while also having a loss below 1 dB. The length of the Faraday rotator is then set by two equations:

$$Vl = 45 \tag{2.1}$$

$$10 \log_{10}\left(e^{-\alpha l}\right) = -1 \tag{2.2}$$

where V is the Verdet coefficient in $°\cdot mm^{-1}$ and α is the absorption coefficient in mm^{-1}. By solving these two equations for l, the figure of merit for an isolator material becomes

$$\frac{V}{\alpha} = 195 \tag{2.3}$$

This chapter aims to better understand Faraday rotation in semiconductors in order to see if they can be used for isolators. It will analyze three different contributors to

the Faraday rotation: free carriers, interband transitions, and magnetic dopants. Experimental results on the Faraday rotation in different semiconductors will be presented. The chapter will conclude by selecting a material for the isolator.

2.1 Free Carrier Faraday Rotation

For free carriers in a uniform medium the restoring force of the nucleus approaches zero. The permittivity can then be found by using Equation 1.4 and setting ω_0 to zero. The off-diagonal term becomes

$$\varepsilon_{xy} = \frac{N_e q^3 B}{\varepsilon_o \left(m^*\right)^2 \omega^3} \frac{1}{\left(1 - j\dfrac{2\gamma}{m^*\omega} - \dfrac{\left(qB_z\right)^2 + \gamma^2}{\left(m^*\omega\right)^2}\right)} \tag{2.4}$$

The mass is written as m^* in order to indicate that it represents the effective carrier mass. The damping term can be expressed in terms of the effective mass and a scattering time τ:

$$\gamma = \frac{m^*}{\tau} \tag{2.5}$$

For semiconductors, τ is usually on the order of picoseconds. The applied magnetic field is on the order of a Tesla. The wavelength of importance is 1.55 μm, which corresponds to ω on the order of 10^{15} sec^{-1}. Using these values, the terms in the denominator become

$$\frac{\gamma}{m^*\omega} = \frac{1}{\tau\omega} = 10^{-3} \tag{2.6}$$

$$\frac{qB_z}{m^*\omega} = 10^{-4} \tag{2.7}$$

These terms are both much less than one and can be neglected in the denominator.

By inserting Equation 2.4 into Equation 1.18, the free carrier Faraday rotation becomes

$$V_{fc} = -\frac{\omega}{c}\frac{\varepsilon_{xy}}{2n} = -\frac{N_e q^3 B}{2c\varepsilon_o n\left(m^*\right)^2 \omega^2} \tag{2.8}$$

Rewriting this expression in terms of optical wavelength, one has:

$$V_{fc} = -\frac{N_e q^3 B \lambda^2}{8\pi^2 c^3 \varepsilon_o n (m^*)^2} \qquad (2.9)$$

A key feature of Equation 2.9 is that the Faraday rotation is inversely proportional to the square of the effective mass of the free carriers and proportional to the carrier concentration. This allows the Faraday rotation to be used for measuring these quantities in semiconductors [12],[13],[14]. Another feature of Equation 2.9 is that the Faraday rotation is proportional to q^3. This means that electrons and holes have Faraday rotations of opposite sign. A final feature of Equation 2.9 is that the Faraday rotation is directly proportional to the wavelength squared. For long wavelengths, the free carriers will be the dominant contributors to the Faraday rotation in a semiconductor, whereas with shorter wavelengths closer to the bandgap, interband transitions will be more important.

An important question to ask now is if the free carrier Faraday rotation is strong enough for an optical isolator. To answer this, the loss due to free carriers must be known. This can be done by using the imaginary part of the index of refraction. The expression for the imaginary part of the refractive index can be found by using Equation 1.25:

$$n^2 = (n_r + jn_i)^2 = \frac{N_e q^2}{\varepsilon_o} \frac{m^*(\omega_o^2 - \omega^2) + j\omega\gamma}{\left(m^*(\omega_o^2 - \omega^2) + j\omega\gamma\right)^2 - (\omega q B_z)^2} \qquad (2.10)$$

For semiconductors, $m^*\omega >> \gamma$ and $m^*\omega >> qB_z$, as shown in Equations 2.6 and 2.7. Using these results and Equation 2.5 for γ, the expression for n_i becomes

$$n_i = \frac{N_e q^2}{2\varepsilon_o n_r \omega^2 m^* \tau} \qquad (2.11)$$

τ is the effective scattering time of the free carrier, which can be expressed in terms of the mobility:

$$\tau = \frac{m^* \mu}{|q|} \qquad (2.12)$$

This only gives an upper limit on τ because the mobility does not take into account electron-electron scattering, which also contributes to the damping term γ.

The imaginary portion of the propagation constant corresponds to a power attenuation of the form $e^{-\alpha l}$, where α is the absorption coefficient. By using Equation 2.12, the expression for α becomes

$$\alpha = 2\frac{\omega}{c}n_i = \frac{N_e|q|^3\lambda^2}{4\pi^2 c^3 \varepsilon_o n_r (m^*)^2 \mu} \tag{2.13}$$

The factor of two is included because the power loss is being considered here. With this result and Equation 2.9, the figure of merit for free carriers becomes:

$$\frac{V}{\alpha} = \frac{B\mu}{2} \tag{2.14}$$

Using a value of 1 T for B and typical values for μ (1,000 to 10,000 $cm^2/V/s$), one obtains a figure of merit between 0.05 and 0.5. For an isolator, this figure of merit should be at least 195, so free carriers will not be desirable for providing Faraday rotation.

2.2   Interband Faraday Rotation

To understand how interband transitions and magnetic dopants in semiconductors contribute to Faraday rotation, a different approach to analyzing Faraday rotation is taken. In Section 1.2 it was shown that in a magneto-optical material right- and left-circular polarizations have different propagation constants, and it is the difference in these propagation constants that cause Faraday rotation. This can be written as:

$$\frac{\theta_f}{l} = V = \frac{\beta_+ - \beta_-}{2} = \frac{\omega}{c}\frac{(n_+ - n_-)}{2} \tag{2.15}$$

β has been rewritten here as $\omega n/c$, with n_+ and n_- corresponding to the indices of refraction for right and left circularly polarized light.

The index of refraction is a function of the electronic transition energy E_{12} (the transition from electronic level 1 to level 2). For small perturbations in the transition energy, denoted as ΔE_{12}, the difference in index of refraction can be Taylor expanded about the unperturbed transition energy to give:

$$n_+ - n_- = \frac{\partial n}{\partial E_{12}}\left(\Delta E_{12}^+ - \Delta E_{12}^-\right) \tag{2.16}$$

where the superscripts indicate the perturbations for right- and left-circularly polarized light. Thus, with knowledge of the functional form of the index of refraction and the value of the perturbations to the transition energy, the Faraday rotation can be calculated for any material.

2.2.1 Index of Refraction as a Function of Transition Energy

The first step to calculating the Faraday rotation from interband transitions is to find the partial derivative of the index of refraction with respect to the transition energy. For semiconductors, the transition energy E_{12} of interest is the bandgap energy E_g. A simple model for the refractive index is given by

$$n^2 - 1 = n_o^2 + \frac{F}{E_g^2 - (E)^2} \tag{2.17}$$

F is the oscillator strength of the transition, and n_o is the contribution from all other sources excluding the interband transition to the refractive index. Inserting the partial derivative of this function with respect to E_g into the expression for the Faraday rotation, one obtains:

$$V = \frac{F}{2\eta c} \frac{1}{n} \frac{E^2}{\left(E_g^2 - E^2\right)^2} \left(\Delta E_g^+ - \Delta E_g^-\right) \tag{2.18}$$

It can be seen that the Faraday rotation will increase rapidly as the photon energy approaches the bandgap energy. By engineering the bandgap of a semiconductor, it is possible to increase its Faraday rotation for a desired wavelength.

For specific semiconductors, explicit expressions exist for the index of refraction based on curve fitting to experimental data. For the quarternary material $In_{1-x}Ga_xAs_yP_{1-y}$ lattice matched to InP, the expression for the index of refraction is [15]

$$n^2 - 1 = 1 + \frac{E_d}{E_o} + \frac{E_d E^2}{E_o^3} + \frac{E_d E^4}{2E_o^3\left(E_o^2 - E_g^2\right)} \tag{2.19}$$

where E is the photon energy and

$$E_o = 0.595x^2(1-y) + 1.626xy - 1.891y + 0.524x + 3.391 \quad (2.20)$$

$$E_d = (12.36x - 12.71)y + 7.54x + 28.91 \quad (2.21)$$

For $In_{1-x}Ga_xAs_yP_{1-y}$ lattice matched to InP, the bandgap E_g is given by

$$E_g = 1.35 - 0.72y + 0.12y^2 \quad (2.22)$$

Figure 2-1 shows $\partial n/\partial E_g$ as a function of wavelength for both InP and $In_{1-x}Ga_xAs_yP_{1-y}$ (x=.290 and y=.628). The bandgap of InP is 0.89 μm, and that of InGaAsP is 1.30 μm. At a wavelength of 1.55μm, $|\partial n/\partial E_g|$ for InGaAsP is larger than InP by a factor of 10, so it is expected that the Faraday rotation for InGaAsP should be 10 times as large as for InP just due to the bandgap. Also, it can be seen that $|\partial n/\partial E_g|$ increases as the wavelength approaches the bandgap for both materials. Thus, it can be seen how bandgap engineering can be used to increase Faraday rotation.
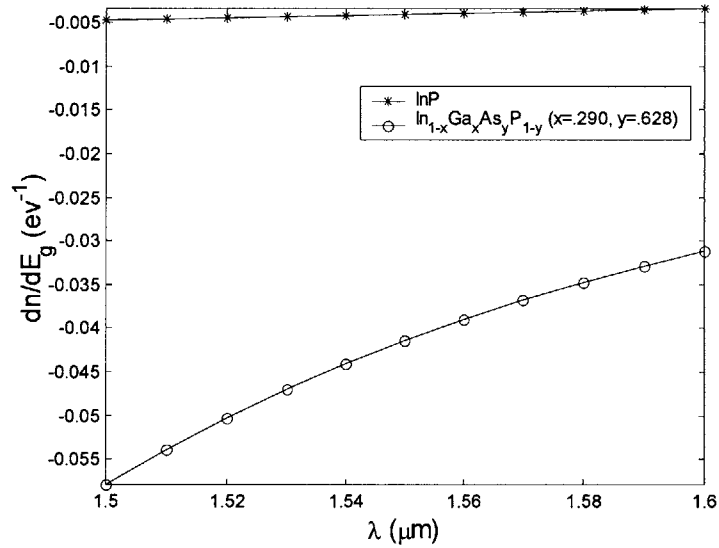
Figure 2-1: $\partial n/\partial E_g$ vs wavelength for InP and $In_{1-x}Ga_xAs_yP_{1-y}$ (x=0.290, y=0.628)

2.2.2 Perturbations to Transition Energy Due to Magnetic Field

The Hamiltonian of an electron in an external magnetic field $\mathbf{B}$ can be written as

$$H_i = -\overline{M} \bullet \overline{B} = \frac{-q}{2m^*}\left(\overline{L} + g\overline{S}\right) \bullet \overline{B} \quad (2.23)$$

where **M** is the magnetic moment of the electron, q is the electron charge, m^* is the effective electron mass, **L** and **S** are the angular momentum and spin operators, and g is the electron g factor. This can be rewritten in the basis of total angular momentum **J**, which is defined as **L+S**:

$$H_i = \frac{-q}{2m^*}\left(\overline{L} + g\overline{S}\right) \cdot \frac{\overline{J}}{|J|}\frac{\overline{J} \cdot \overline{B}}{|J|} = \frac{-q}{2m^*}\frac{\left(\overline{L} + g\overline{S}\right) \cdot \left(\overline{L} + \overline{S}\right)J_z B_z}{J^2} \tag{2.24}$$

Using the identity

$$\overline{L} \cdot \overline{S} = \frac{J^2 - L^2 - S^2}{2} \tag{2.25}$$

The Hamiltonian can be rewritten as

$$H_i = \frac{-q}{2m^*}\frac{(g+1)J^2 + (g-1)\left(S^2 - L^2\right)}{2J^2}J_z B_z \tag{2.26}$$

Now that the Hamiltonian is in the total angular momentum basis, the energy splitting for any state can be written as

$$\Delta E_{j,m_j} = \frac{-q\hbar}{2m^*}g_L m_j B_z \tag{2.27}$$

where m_j is the total angular momentum component along the z axis, j is the total angular momentum, ħ is Planck's constant divided by 2π, and g_L is the Landé g factor, which is defined as

$$g_L = \frac{g+1}{2} + \frac{(g-1)\left(s(s+1) - l(l+1)\right)}{2j(j+1)} \tag{2.28}$$

where j, l, and s correspond to the magnitude of the total angular momentum, orbital angular momentum, and spin. The above expression results from the fact that the eigenvalue of an angular momentum operator A^2 is $\hbar^2 a(a+1)$.

For a semiconductor, the transitions of importance are between the conduction and valence band. The conduction band is mainly s-orbitals, so l=0, and the free carriers are electrons, so q is negative. The valence band has p-orbitals, so l=1, and the free carriers are holes, so q is positive. The energy levels will split as shown in Figure 2-2, with each level designated by its total angular momentum quantum numbers (|j,m_j⟩). The electronic transitions of interest involve an electron losing or gaining one quantum of angular momentum and are indicated by the arrows in Figure 2-2. Because angular

momentum must be conserved in the transition, a photon with a right- or left-circular polarization, represented as σ+ or σ-, is emitted.
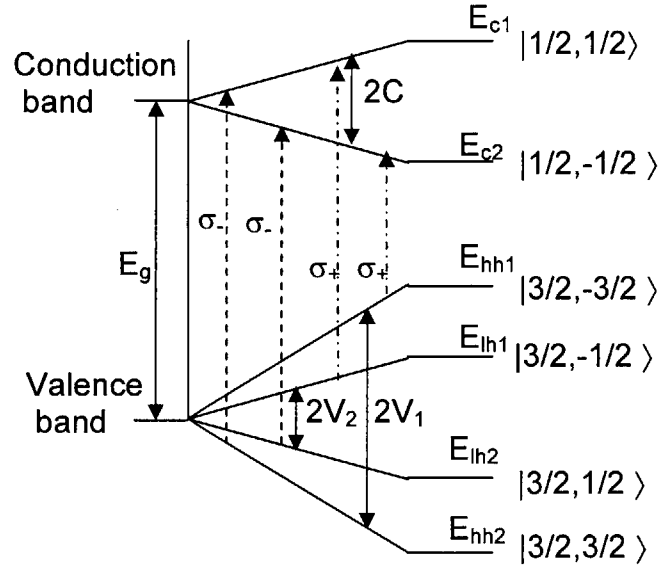
Figure 2-2: Energy splitting of valence and conduction bands due to application of magnetic field

The energies for the transitions in Figure 2-2 are

$$\Delta E+ = E_{c2} - E_{hh1} = E_g - (C + V_1) \tag{2.29}$$

$$\Delta E^+ = E_{c1} - E_{lh1} = E_g + (C - V_2) \tag{2.30}$$

$$\Delta E^- = E_{c2} - E_{lh2} = E_g - (C - V_2) \tag{2.31}$$

$$\Delta E^- = E_{c1} - E_{hh2} = E_g + (C + V_1) \tag{2.32}$$

where

$$C = \mu_B B_z \frac{1}{2} \frac{m_o}{m_c^*} g_c \tag{2.33}$$

$$V_1 = \mu_B B_z \frac{1}{2} \frac{m_o}{m_{hh}^*} (g_v + 2) \tag{2.34}$$

$$V_2 = \mu_B B_z \frac{1}{6} \frac{m_o}{m_{lh}^*} (g_v + 2) \tag{2.35}$$

μ_B is the Bohr magneton which is defined as $|q|\hbar/(2m_o)$ and has a value 6.078×10^{-5} eV/T, and m_o is the free electron mass. The subscript on the g factors indicate valence and

conduction band, while the subscript on the effective masses indicate conduction, heavy hole, and light hole bands. The Faraday rotation is proportional to the energy difference for transitions for left- and right-circular polarized photons. The largest energy difference is for the conduction to light-hole transition:

$$\Delta E^+ - \Delta E^- = \left(E_{c2} - E_{lh1}\right) - \left(E_{c1} - E_{lh2}\right) = \mu_B B_z \left(\frac{m_o}{m_c^*} g_c - \frac{m_o}{m_{hh}^*} \frac{\left(g_v + 2\right)}{3}\right) \qquad (2.36)$$

The g factor for free electrons is 2, but in a semiconductor it differs from this value. It can be calculated using simple k·p theory. For the conduction and valence band, the g factor is given by [16]:

$$g_c = 2 - \frac{2E_p \Delta}{3E_g \left(E_g + \Delta\right)} \qquad (2.37)$$

$$g_v = 1 + \frac{E_p \left(3E_g + 2\Delta\right)}{3E_g \left(E_g + \Delta\right)} \qquad (2.38)$$

Δ is the spin-orbit splitting energy and E_p is the energy equivalent matrix momentum element, expressed as $2|P|^2/m_o$, and P is the momentum matrix element. These parameters are well known for most semiconductors.

Using these results, the expression for the Verdet coefficient becomes:

$$V = \frac{\omega}{2c} \frac{\partial n}{\partial E_g} \mu_B B_z \left(\frac{m_o}{m_c^*} g_c - \frac{m_o}{m_{lh}^*} \frac{\left(g_v + 2\right)}{3}\right) \qquad (2.39)$$

Thus, an explicit expression for the interband Faraday rotation in semiconductors is obtained in terms of well known parameters.

2.2.3 Perturbations to Transition Energy Due to Magnetic Dopants

If magnetic dopants are introduced into a semiconductor, the energy splitting can be enhanced further. This is due to an sp-d exchange interaction between the magnetic dopant electrons and the band electrons. This interaction can be described by a Heisenberg-type Hamiltonian [17]:

$$H_{int} = \sum_{R_i} J\left(\vec{r} - \overline{R_i}\right) \overline{S_i} \bullet \vec{\sigma} \qquad (2.40)$$

where J(r-R$_i$) is the exchange integral, R$_i$ is the site of each magnetic dopant atom, S$_i$ is the spin operator for the magnetic dopant electrons, and σ$_i$ is the spin operator for the free carriers in the semiconductor. The new energy levels due to this Hamiltonian can be found using k·p theory. The resulting levels split just as the levels found for intrinsic semiconductors, but the magnitude of the splitting is different. Figure 2-3 shows the energy levels and electronic transitions for right- and left- handed circular polarizations.
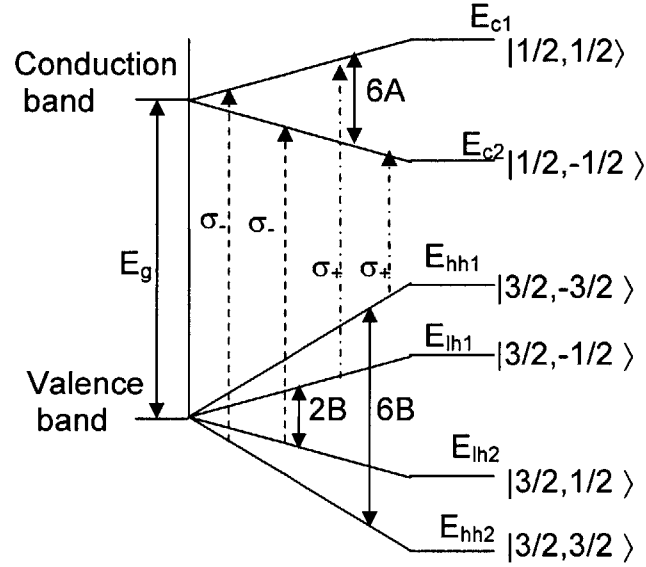
Figure 2-3: Energy splitting of valence and conduction bands due to sp-d exchange interaction with magnetic dopants

The transition energies are

$$\Delta E^- = E_{c1} - E_{lh1} = E_g + (3A + B)$$ (2.41)

$$\Delta E^+ = E_{c2} - E_{hh1} = E_g + 3(B - A)$$ (2.42)

$$\Delta E^- = E_{c1} - E_{hh2} = E_g - 3(B - A)$$ (2.43)

$$\Delta E^- = E_{c2} - E_{lh1} = E_g - (3A + B)$$ (2.44)

where the splitting terms are given by [18]

$$A = \frac{1}{6}\alpha \frac{M}{g_M \mu_B}$$ (2.45)

$$B = \frac{1}{6}\beta \frac{M}{g_M \mu_B}$$ (2.46)

α and β are the exchange integrals for the conduction and valence band electrons, g_M is the Landé g factor of the magnetic dopant spins, and M is the magnetization of the dopant per unit volume.

The largest difference in right- and left-circular polarized transition energies is

$$\Delta E^+ - \Delta E^- = \left(E_{c2} - E_{hh1}\right) - \left(E_{c1} - E_{hh2}\right) = 6(B - A) = \frac{\beta - \alpha}{g_M \mu_B} M \quad (2.47)$$

The magnetization of the dopants for low concentrations can be expressed as [19]

$$M = xN_o \left(g_M \mu_B\right)^2 \frac{S(S+1)}{3k_B T} B \quad (2.48)$$

where x is the dopant concentration, N_o is the number of unit cells per volume, k_B is Boltzman's constant, T is the temperature, B is the applied magnetic field, and S is the electronic spin of the magnetic dopant atom.

With this result the Verdet coefficient due to magnetic dopants becomes

$$V = \frac{\omega}{2c} \frac{\partial n}{\partial E_g} (\beta - \alpha) xN_o \left(g_M \mu_B\right) \frac{S(S+1)}{3k_B T} B \quad (2.49)$$

The important thing to note from this expression is that the Verdet coefficient is proportional to the magnetic dopant concentration. This is similar to free carrier Faraday rotation, but the difference here is that there is minimal loss caused by the magnetic dopants. It has been shown that in semiconductors such as InP, the introduction of magnetic dopants will have negligible contribution to the optical loss for wavelengths below the bandgap [20]. Therefore, magnetic dopants are an effective way to enhance the Verdet coefficient without increasing the loss.

The unknown terms in Equation 2-49 are the exchange integrals α and β. These terms are difficult to calculate and must be determined experimentally. The difference of these exchange integrals will determine the sign of the Faraday rotation. Previous results have shown that the Faraday rotation in semiconductors caused by magnetic dopants such as Fe is negative [21]. Therefore, by increasing the dopant concentration in a semiconductor, the Faraday rotation can become zero or even negative.

2.3 Faraday Rotation Measurement

2.3.1 Experimental Setup

The experimental setup for measuring the Faraday rotation in bulk samples is shown if Figure 2-4. The samples are placed in an electromagnet capable of providing magnetic fields as strong as 2 Tesla. A 50 dB extinction ratio polarizer at the input provides linearly polarized light oriented at 45° from the horizontal axis. After the light is rotated by the sample, a polarizing beam-splitter with 50 dB of extinction separates the horizontal and vertical polarizations. Two photodetectors measure the powers of the polarizations.
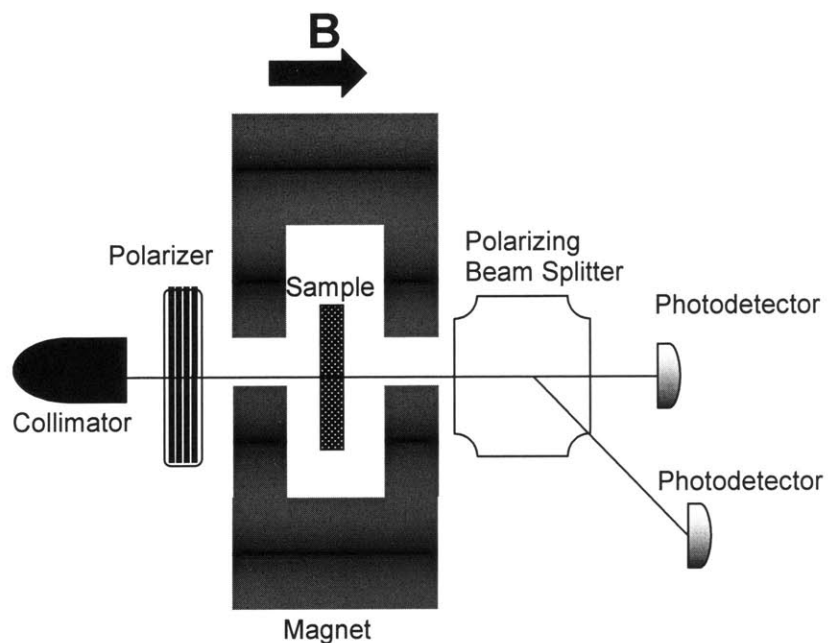
Figure 2-4: Experimental setup for measuring Faraday rotation in bulk samples

The Jones' matrix formalism is used to analyze the setup. The sample which provides a Faraday rotation θ_F can be modeled as a Jones' matrix of the form

$$\begin{bmatrix} \cos(\theta_F) & -\sin(\theta_F) \\ \sin(\theta_F) & \cos(\theta_F) \end{bmatrix} \tag{2.50}$$

Ideally the input polarization should be at 45°, but the input may not be exactly at this angle. If the input light is at an angle 45°+δ, then the output from the sample can then be modeled as

$$\overline{E_{out}} = E_o \begin{bmatrix} \cos(\theta_F) & -\sin(\theta_F) \\ \sin(\theta_F) & \cos(\theta_F) \end{bmatrix} \begin{bmatrix} \cos(45+\delta) \\ \sin(45+\delta) \end{bmatrix} = \frac{E_o}{\sqrt{2}} \begin{bmatrix} \cos(45+\delta)\cos(\theta_F) - \sin(45+\delta)\sin(\theta_F) \\ \sin(45+\delta)\cos(\theta_F) + \cos(45+\delta)\sin(\theta_F) \end{bmatrix}$$

(2.51)

The normalized difference in the powers for the two polarizations is then:

$$dP = \frac{|E_x|^2 - |E_y|^2}{|E_x|^2 + |E_y|^2} = -\cos(2\delta)\sin(2\theta_F) - \sin(2\delta)\cos(2\theta_F)$$ (2.52)

The error in input angle δ will cause an error in the calculated angle. By switching the sign of the magnetic field, the sign of θ_F will also switch. By subtracting dP for the positive and negative magnetic field the error due to the imbalance can be reduced:

$$dP^+ - dP^- = -2\cos(2\delta)\sin(2\theta_F)$$ (2.53)

For δ as large as 10°, cos(2δ) is 0.94. Thus a 10° error in the input will only result in a 6 % error in the measured value of θ_F. In practice, δ is kept below 1° for bulk measurements, resulting in 0.1 % error in the Faraday rotation measurement.

2.3.2 Cavity Enhanced Rotation:

Because some samples had very clean, reflective surfaces, an optical cavity was created. When a Faraday rotating material is placed in an optical cavity, the rotation is enhanced on resonance. In order to extract the single pass rotation, a closer analysis of cavity enhanced rotation is provided here.
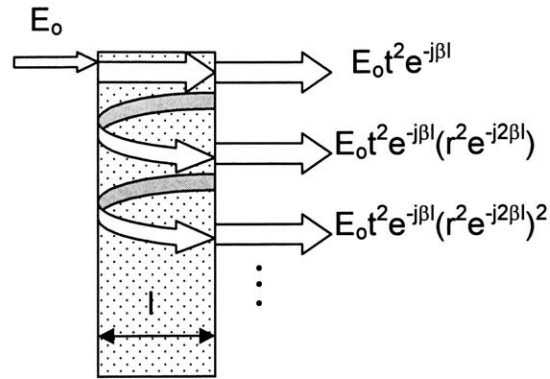
Figure 2-5: Transmission through an optical cavity of length l, propagation constant β, and field transmission and reflection coefficients t and r

To understand this phenomenon, it is helpful to first understand the transmission characteristics of an optical cavity. Figure 2-5 shows a picture of a simple optical cavity of length l. β is the propagation constant of the cavity material, and t and r are the field transmission and reflection coefficients of the surfaces at the ends of the cavity. The transmission is given by

$$E_t = E_o t^2 e^{-j\beta l}\left(1 + r^2 e^{-j2\beta l} + \left(r^2 e^{-j2\beta l}\right)^2 + ...\right) = \frac{E_o t^2 e^{-j\beta l}}{1 - r^2 e^{-j2\beta l}} \qquad (2.54)$$

For a Faraday rotating material, the allowed polarization states are circular polarizations, each with a different β. The Faraday rotation through the cavity will be given by the phase difference between the two circular polarizations:

$$\theta_F = \frac{\angle E_t^+ - \angle E_t^-}{2} \qquad (2.55)$$

The phase of the transmitted light is

$$\angle E_t = -\tan^{-1}\left(\frac{\text{Im}\{E_t\}}{\text{Re}\{E_t\}}\right) = \tan^{-1}\left(\frac{1 + r^2}{1 - r^2}\tan(\beta l)\right) \qquad (2.56)$$

For a Faraday rotating material, the propagation constant is given by

$$\beta_\pm = \frac{\omega}{c}\left(n \pm \frac{\varepsilon_{xy}}{2n}\right) = \beta_o \pm V \qquad (2.57)$$

where β_o is the propagation constant under no applied magnetic field and V is the Verdet coefficient. On resonance, the round-trip phase through the cavity is 2π, and $\tan(\beta_o l)=0$.

Therefore, $\tan(\beta_o l \pm Vl) \approx \pm Vl$. Under this approximation, the Faraday rotation on resonance becomes

$$\theta_F = \frac{1 + r^2}{1 - r^2} Vl \qquad (2.58)$$

Because Vl is the Faraday rotation with no cavity present, it can be seen that the effect of the cavity is to enhance the rotation by a factor of $(1+r^2)/(1-r^2)$. This factor can be calculated from the power transmission spectrum of the cavity. The transmitted power is

$$P = |E|^2 = \frac{|E_o|^2 t^4}{1 + r^4 - 2r^2 \cos(2\beta l)} \qquad (2.59)$$

The ratio of the maximum transmission to minimum transmission is then

$$\frac{P_{max}}{P_{min}} = \frac{\left(1 + r^2\right)^2}{\left(1 - r^2\right)^2} \qquad (2.60)$$

Thus, by measuring the Faraday rotation on resonance and the power transmission spectrum, the single pass Faraday rotation θ_{sp} can be expressed as

$$\theta_{sp} = \theta_{max} \sqrt{\frac{P_{min}}{P_{max}}} \qquad (2.61)$$

where θ_{max} is the Faraday rotation on resonance. This method allows for the extraction of the Verdet coefficient of a material from its cavity enhanced rotation. The analysis of cavity enhanced rotation presented in this section differs from previous work [22], however, the same result (Equation 2.61) is obtained.

2.3.3 Experimental Results

The samples measured included iron doped InP (Fe:InP), sulfur doped InP (S:InP), and InGaAsP, both undoped and iron doped. The sulfur is a donor and provides free electrons to the InP. There are no free carriers in iron doped InP because the iron creates a state in the bandgap which traps the free carriers. This is why Fe:InP is known as semi-insulating InP.

The Verdet coefficient of S:InP is shown in Figure 2-6. As can be seen, at longer wavelengths, the Faraday rotation increases. In this region the free carrier rotation is dominant.
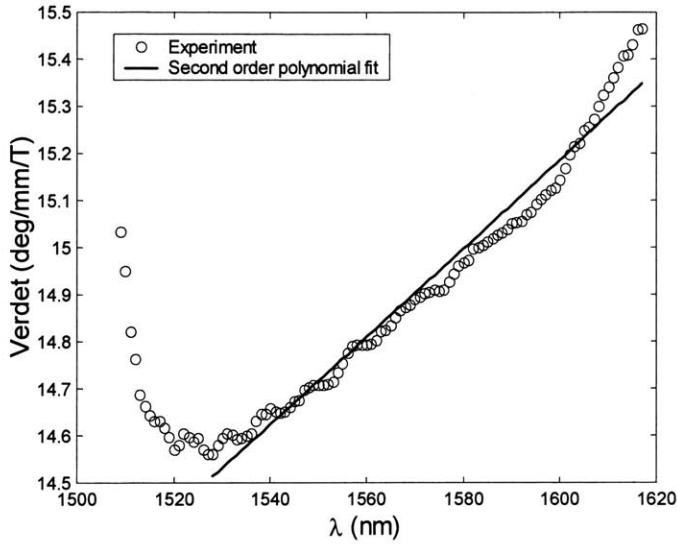
Figure 2-6: Verdet coefficient of S:InP vs wavelength. The free carrier concentration is 3.6×10^{18} cm^{-3}

By fitting a second order polynomial to the curve at longer wavelengths, as shown in Figure 2-6, the carrier concentration was calculated. For this sample, the actual carrier concentration is 3.6×10^{18} cm^{-3}, and the calculated carrier concentration is 3.7×10^{18} cm^{-3}, thus showing close agreement with Equation 2.9.

The total rotation is found by adding the free carrier rotation and interband rotation. Figure 2-7 shows the theoretical Verdet coefficient for S:InP, along with the measured Verdet coefficient. Also plotted in Figure 2-7 is the theoretical interband Verdet coefficient calculated using Equation 2.39 and the theoretical free carrier rotation calculated using Equation 2.9. The value of the experimental Verdet coefficient is larger than the theoretical value by a factor of 2. This is because the theoretical interband rotation is too small by a factor of 8.
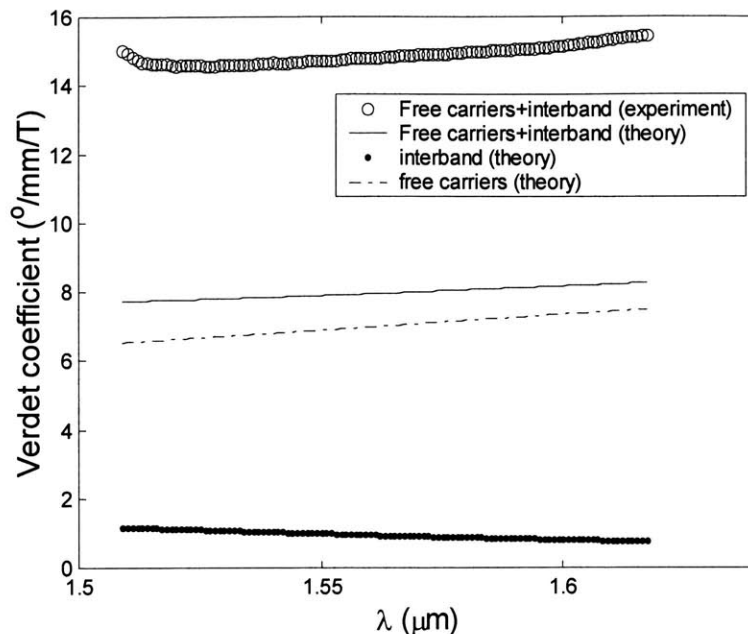
Figure 2-7: Theoretical and experimental Verdet coefficient of S:InP

Figure 2-8 shows the measured Verdet coefficient and optical loss versus wavelength for the Fe:InP. The Fe concentration is 2.9×10^{16} cm^{-3} and the Verdet coefficient of Fe:InP is half as large as for undoped InP. This indicates that the contribution of Fe atoms to the Faraday rotation is actually opposite that of the intrinsic contribution.

The loss measurements were made using ellipsometry. The error of the loss measurement below the bandgap is 0.04 mm^{-1}, which is larger than the largest measured loss. The loss minimum in Figure 2-8 may not be a true minimum, but instead may be due to measurement error.

The figure of merit V/α for this material at a magnetic field of 1 Tesla is shown in Figure 2-9. With the uncertainty in the loss measurement, the maximum figure of merit ranges between 51 to 157, which is not large enough for an optical isolator.
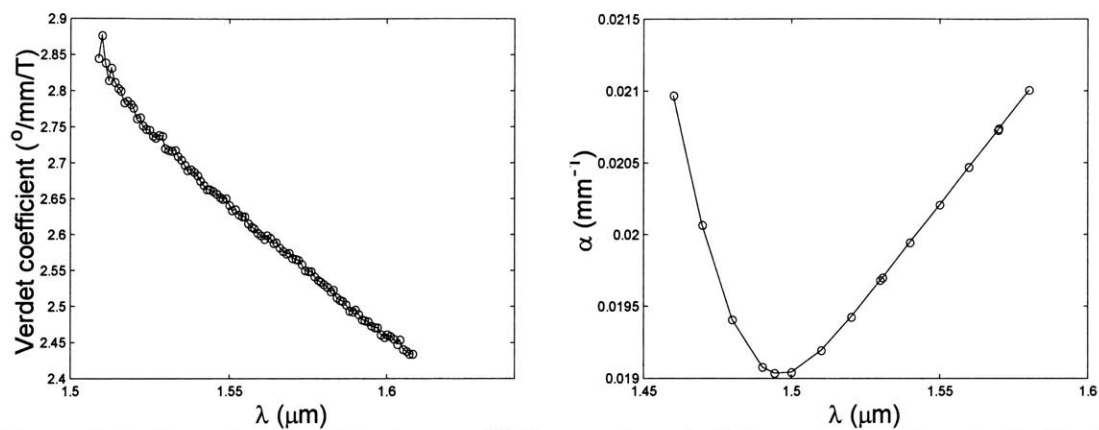
Figure 2-8: Experimental Verdet coefficient and optical loss vs wavelength for Fe:InP. The Fe concentration is 2.9×10^{16} cm^{-3}
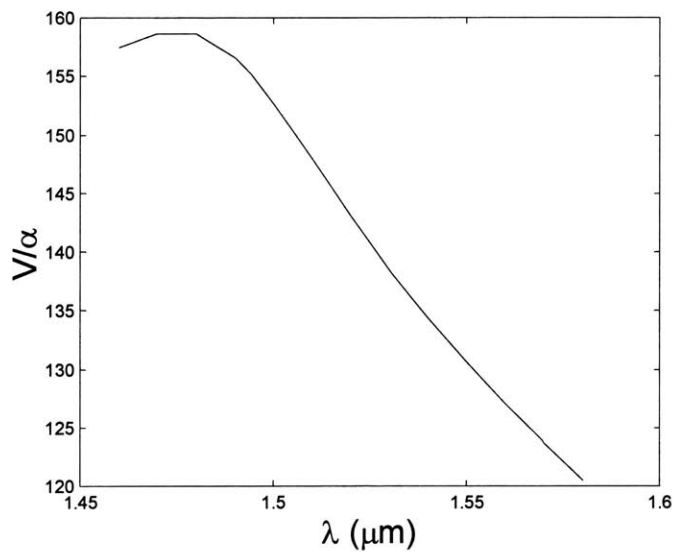
Figure 2-9: Figure of merit V/α for Fe:InP at a magnetic field of 1 T

Fe: InP	1 µm
Fe: InGaAsP	0.5 µm
Fe: InP	1 µm
Fe: InP	350 µm

Figure 2-10: Fe:In$_{1-x}$Ga$_x$As$_y$P$_{1-y}$ (x=.290 and y=.628) structure used for Faraday rotation measurements

Fe:In$_{1-x}$Ga$_x$As$_y$P$_{1-y}$ (x=.290 and y=.628) lattice matched to InP was epitaxially grown on an Fe:InP substrate as shown in Figure 2-10. This sample had very clean surfaces, so it acted as an optical cavity. No cavity effect was observed in the Fe:InP and S:InP samples because their surfaces were scratched and did not act like smooth mirrors. The measured Faraday rotation and power spectrum versus wavelength for the Fe:InGaAsP is shown in Figure 2-11. On resonance, the rotation is a maximum, as predicted by the theory. Samples of Fe:InGaAsP with various Fe concentrations were measured and the single pass rotation was extracted using Equations 2.61.
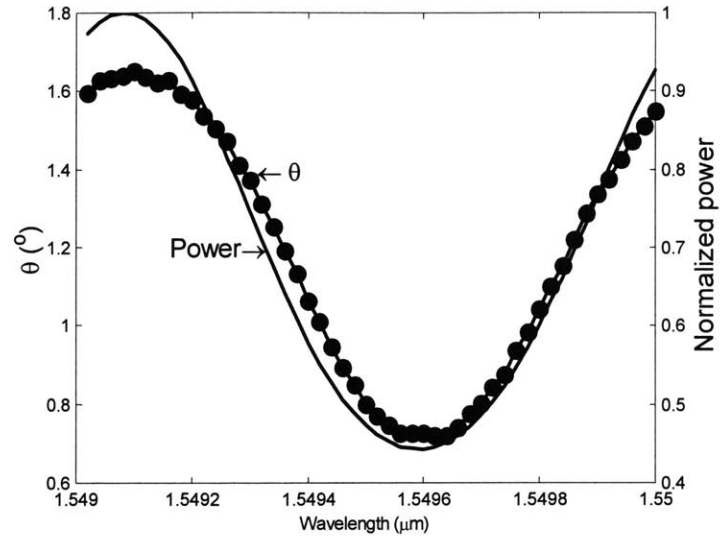
Figure 2-11: Cavity enhanced Faraday rotation and power spectrum versus wavelength for Fe:InGaAsP sample at a magnetic field of 1.3 T

Because the substrate was over 700 times thicker than the InGaAsP, the measured rotation was dominated by the substrate. To obtain the rotation of the InGaAsP from the measured rotation of the entire structure, the substrate rotation was subtracted off from each samples total rotation. The results on Fe:InP were used to calculate the substrate rotation.

The Verdet coefficient of InGaAsP can be calculated using the following expression:

$$V_{InGaAsP} = \frac{\theta_o - \theta_s}{Bl_{InGaAsP}} \tag{2.62}$$

where θ_o is the measured rotation in the sample, θ_s is the calculated rotation of the substrate, $l_{InGaAsP}$ is the thickness of the InGaAsP, and B is the applied magnetic field. The substrate rotation is calculated using the measured rotation for the Fe:InP sample:

$$\theta_s = V_s Bl_s = \frac{\theta_{Fe:InP} l_s}{l_{Fe:InP}} \tag{2.63}$$

where $l_{Fe:InP}$ and l_s are the lengths of the Fe:InP sample and the substrate of the InGaAsP samples, respectively. $\theta_{Fe:InP}$ is the measured rotation for the Fe:InP sample and B cancels out because it is the same for each measurement. Inserting this into Equation 2.62 gives

$$V_{InGaAsP} = \frac{\theta_o - \theta_{Fe:InP} \dfrac{l_s}{l_{Fe:InP}}}{Bl_{InGaAsP}} \tag{2.64}$$

The error in $V_{InGaAsP}$ is given by

$$\left(\Delta V_{InGaAsP}\right)^2 = \left(\frac{\partial V_{InGaAsP}}{\partial \theta_o}\right)^2 \left(\Delta \theta_o\right)^2 + \left(\frac{\partial V_{InGaAsP}}{\partial \theta_{Fe:InP}}\right)^2 \left(\Delta \theta_{Fe:InP}\right)^2 \tag{2.65}$$

Because the uncertainty in each rotation measurement is 0.01°, the error in $V_{InGaAsP}$ becomes

$$\left(\Delta V_{InGaAsP}\right) = \frac{\Delta\theta}{Bl_{InGaAsP}} \sqrt{1 + \frac{l_s}{l_{Fe:InP}}} \tag{2.62}$$

By inserting numerical values for all of the constants, the error becomes

$$\Delta V_{InGaAsP} = \frac{0.01°}{\left(1.315T\right)\left(5x10^{-4}mm\right)} \sqrt{1 + \left(\frac{0.350mm}{0.487mm}\right)} = 18.7\frac{o}{mm \cdot T} \tag{2.66}$$

Figure 2-12 shows the Verdet coefficient versus Fe concentration in the InGaAsP at a wavelength of 1.55μm. As can be seen in the plot, as the Fe concentration is increased, the Verdet coefficient becomes more and more negative, which agrees with the results for Fe:InP. Also, the rotation is linearly proportional to the iron concentration, as expected for low iron concentrations. The linear fit to the data in Figure 2-12 predicts a value of 96.7 ± 18.7 °/mm/T for the Verdet coefficient for undoped InGaAsP at a wavelength of 1.55μm, while Equation 2.39 predicts a value of 48.2 °/mm/T.
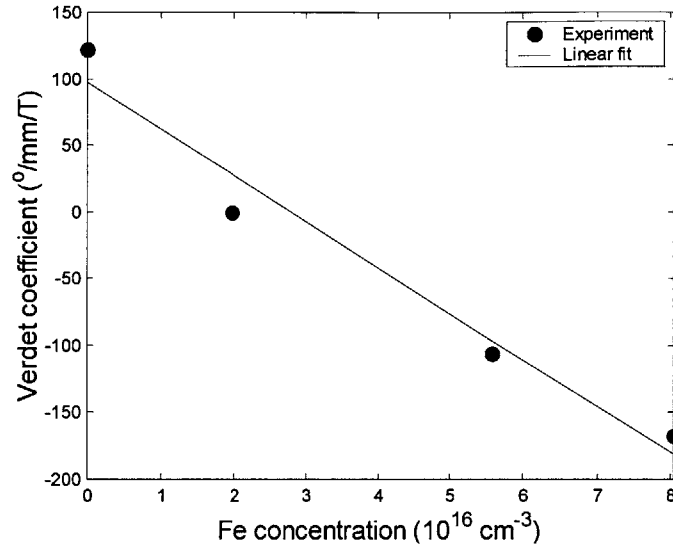
Figure 2-12: Verdet coefficient versus iron concentration of Fe:InGaAsP at a wavelength of 1.55μm

Material	V [°/mm/T] (experiment)	V [°/mm/T] (theory)	α [mm^{-1}]	Experimental V/ α at 1 T (Target=195)
YIG	130		0.11	1182
InP	7.8	1.0	0.02	390
Fe:InP : 2.9×10^{16} cm^{-3}	2.6		0.02	130
InGaAsP	96.7	48.2		
Fe:InGaAsP : 8.0×10^{16} cm^{-3}	-181.4			

Table 2-1: Verdet coefficient, absorption coefficient, and figure of merit for different materials at 1.55μm

Table 2-1 shows the Verdet coefficient, optical loss, and figure of merit for various materials at 1.55μm. For the figure or merit, it is assumed that the external magnetic field is 1 T. As can be seen from the table, undoped InGaAsP has a Verdet coefficient comparable to YIG. This indicates that this material is a viable candidate for an integrated optical isolator. The main reason for the enhanced strength of the Faraday

rotation is the decreased bandgap of the InGaAsP. By adjusting its composition to reduce the bandgap, the Verdet coefficient of InGaAsP could be increased even more. The optical loss for InGaAsP is not listed in the table because the sample was too thin for loss measurements. However, in Chapter 4 optical loss measurements for InGaAsP waveguides will be shown.

2.4 Summary

The aim of this chapter was to present a theoretical model for semiconductor Faraday rotation in order to determine what sort of material would be ideal for an optical isolator. The first key result is that by tuning the bandgap closer to the operational wavelength, the Faraday rotation can be increased. The second key result is that the addition of magnetic dopants will contribute to the Faraday rotation via an sp-d exchange interaction. Thus there are two parameters, bandgap and magnetic dopant concentration, which can be used to control the Faraday rotation.

It was found that InGaAsP is a suitable material for an optical isolator. It is lattice matched to InP, which is the substrate for semiconductor lasers used for telecommunications. These are the lasers for which the isolator is being designed, so the use of InGaAsP allows for monolithic integration. The bandgap of InGaAsP can be tuned by controlling its composition, thus allowing for tuning of the Faraday rotation. Magnetic dopants provide a Faraday rotation of the opposite sign of undoped InGaAsP. They can be used to increase the Faraday rotation with heavier doping concentrations. The next step is to design an integrated isolator using this material. This is discussed in Chapter 3.

Chapter 3
Integrated Isolator Design

The design used for the isolator was discussed in Chapter 1. The design is shown again here in Figure 3-1. It is a four port device which acts as a circulator. When only two ports are used, the device functions as an isolator. It consists of two Faraday rotators which provide 45° of non-reciprocal rotation, two half-wave plates which provide 45° of reciprocal rotation, and two 3 dB couplers. The half-wave plates provide their rotation by having their slow-axis, defined by the vector **s** in Figure 3-1, oriented at 22.5° and -22.5° to the horizontal. This chapter will go through the design of each of these components in waveguide form. It will then discuss the effect of fabrication errors on isolator performance. Finally, simulation results for the isolator bandwidth will be presented. An eigenmode propagation code was written to simulate the isolator bandwidth using 2-D optical mode profiles of the waveguide structures calculated using a fully-vectorial mode solver written by Mike Watts.
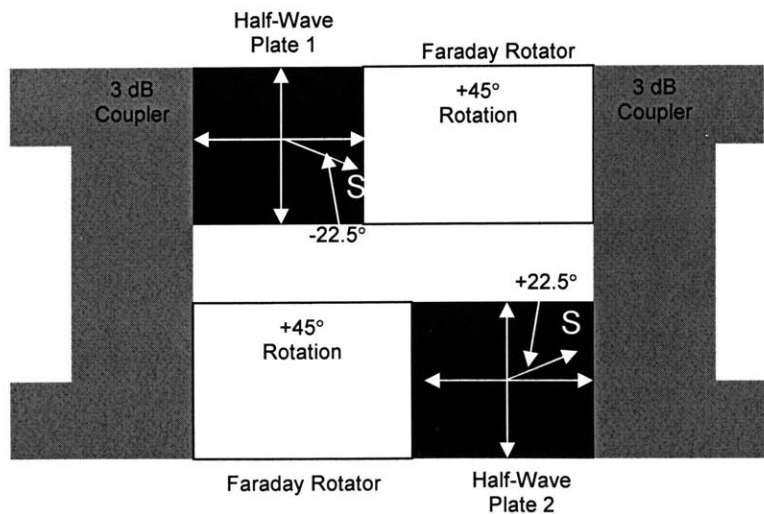
Figure 3-1: Integrated isolator block diagram

3.1 Faraday Rotator

3.1.1 Theory

To understand the effects of birefringence on Faraday rotation, it is easiest to view the problem not as a polarization rotation, but as a coupling of transverse electric (TE) and transverse magnetic (TM) polarizations. The coupled mode equations modeling Faraday rotation are [23]

$$\frac{\partial A_{TE}}{\partial z} = -j\beta_{TE} A_{TE} + V A_{TM} \tag{3.1}$$

$$\frac{\partial A_{TM}}{\partial z} = -V A_{TE} - j\beta_{TM} A_{TM} \tag{3.2}$$

V is the Verdet coefficient, A represents the field amplitude, and β is the propagation constant for the TE and TM modes. By assuming that the fields have an $e^{-j\beta z}$ dependence, the eigenvectors v and eigenvalues λ of this system of equations are found to be

$$\overline{v_1} = \begin{bmatrix} 1 \\ j\dfrac{\Delta + \psi}{V} \end{bmatrix}, \lambda_1 = -j(\beta_o + \psi) \tag{3.3}$$

$$\overline{v_2} = \begin{bmatrix} 1 \\ j\dfrac{\Delta - \psi}{V} \end{bmatrix}, \lambda_2 = -j(\beta_o - \psi) \tag{3.4}$$

where

$$\Delta = \frac{(\beta_{TE} - \beta_{TM})}{2} \tag{3.5}$$

$$\beta_o = \frac{(\beta_{TE} + \beta_{TM})}{2} \tag{3.6}$$

$$\psi = \sqrt{\Delta^2 + V^2} \tag{3.7}$$

The eigenvectors represent the polarization states of the system, and the eigenvalues represent their propagation constants. Using the results of Appendix A, the Jones' matrix for a birefringent Faraday rotator of length L is given by

$$\overline{\overline{S}} = \Lambda D \Lambda^{-1} =$$

$$\begin{bmatrix} \cos(\psi L) + j\dfrac{\Delta}{\psi}\sin(\psi L) & -\dfrac{V}{\psi}\sin(\psi L) \\ \dfrac{V}{\psi}\sin(\psi L) & \cos(\psi L) - j\dfrac{\Delta}{\psi}\sin(\psi L) \end{bmatrix} \qquad (3.8)$$

where the matrix Λ has the eigenvectors v_1 and v_2 in its columns, and D is a diagonal matrix with the eigenvalues $e^{\lambda_1 L}$ and $e^{\lambda_2 L}$ along its diagonal. The common phase factors have been dropped in the above expression. In the limit of no Faraday rotation ($V=0$), this matrix reduces to

$$\overline{\overline{S}} = \begin{bmatrix} e^{-j\frac{(\beta_{TE}-\beta_{TM})}{2}L} & 0 \\ 0 & e^{j\frac{(\beta_{TE}-\beta_{TM})}{2}L} \end{bmatrix} \qquad (3.9)$$

This is just the Jones' matrix of a reciprocal birefringent element. In the opposite limit where there is no birefringence ($\Delta=0$), the Jones's matrix becomes

$$\overline{\overline{S}} = \begin{bmatrix} \cos(VL) & -\sin(VL) \\ \sin(VL) & \cos(VL) \end{bmatrix} \qquad (3.10)$$

This is the Jones matrix for a Faraday rotation through an angle VL. If birefringence is present, the rotation will be less than VL. If $\Delta \gg V$, then the effect of the birefringence will dominate and the Faraday rotator will act like a reciprocal birefringent element. In the opposite limit, the Faraday rotator will function properly. Thus, it can be mathematically seen how the birefringence suppresses the Faraday rotation.

For a more intuitive explanation for waveguide Faraday rotation, it helps to think in terms of power exchange. The Verdet coefficient can be viewed as the rate of power exchange between the TE and TM modes. In a birefringent free waveguide, both modes have the same propagation constant, which means they have the same phase velocity. If the two modes are traveling at the same velocity, then it is easy for them to exchange power. In fact, in this limit, all the power from one mode can be transferred to the other. This would correspond to a 90° Faraday rotation. If birefringence is present, the modes

will not travel at the same velocity. In this case, full power transfer will never be achieved. Thus, no matter how long the Faraday rotator is, a 90° will never be possible. This is the source of the Faraday rotation suppression.

3.1.2 Faraday Rotator Limits on Isolation

To see how much birefringence can be tolerated, a Jones' matrix analysis of the isolator is used. For the Faraday rotator (FR), VL=π/4. If no birefringence is present, this will give a 45° rotation, but if there is birefringence, the Jones matrix will become

$$FR(45°) = \begin{bmatrix} a & -b \\ b & a^* \end{bmatrix} \tag{3.11}$$

where

$$a = \cos\left(\frac{\pi}{4}\sqrt{1+\left(\frac{\Delta}{V}\right)^2}\right) + \left(\frac{j\frac{\Delta}{V}}{\sqrt{1+\left(\frac{\Delta}{V}\right)^2}}\right)\sin\left(\frac{\pi}{4}\sqrt{1+\left(\frac{\Delta}{V}\right)^2}\right) \tag{3.12}$$

$$b = \left(\frac{1}{\sqrt{1+\left(\frac{\Delta}{V}\right)^2}}\right)\sin\left(\frac{\pi}{4}\sqrt{1+\left(\frac{\Delta}{V}\right)^2}\right) \tag{3.13}$$

In the forward direction, the Jones' matrices of the two arms of the circulator are

$$A_1 = HWP(22.5°) * FR = \frac{1}{\sqrt{2}}\begin{bmatrix} a+b & a^*-b \\ a-b & -(a^*+b) \end{bmatrix} \tag{3.14}$$

$$A_2 = FR * HWP(-22.5°) = \frac{1}{\sqrt{2}}\begin{bmatrix} a+b & -(a-b) \\ -(a^*-b) & -(a^*+b) \end{bmatrix} \tag{3.15}$$

where HWP stands for half-wave plate and the angle represents the orientation of the slow axis.

In the reverse direction, the Jones' matrices of the two arms are

$$A_1 = FR * HWP(22.5°) = \frac{1}{\sqrt{2}}\begin{bmatrix} a-b & a+b \\ a^*+b & -a^*+b \end{bmatrix} \tag{3.16}$$

$$A_2 = HWR(-22.5°) * FR = \frac{1}{\sqrt{2}}\begin{bmatrix} a-b & -(a^*+b) \\ -a+b & a^*+b \end{bmatrix}$$

(3.17)

When the reverse Jones' matrices are added together, the result is

$$A_1 + A_2 = \sqrt{2}\begin{bmatrix} a-b & j\,\mathrm{Im}\{a\} \\ -j\,\mathrm{Im}\{a\}+b & b \end{bmatrix}$$

(3.18)

where Im{a} refers to the imaginary part of a. With perfect 3 dB couplers, the maximum possible isolation will be given by any light in one arm which is not exactly out of phase with the light in the opposite arm. To calculate this, assume that `the input light with power normalized to one has equal TE and TM components. Then the isolation can be defined as the power of the Jones' vector obtained after multiplying the input with Equation 3.18:

$$Isolation = \left| (A_1 + A_2)\frac{1}{\sqrt{2}}\begin{bmatrix} 1 \\ 1 \end{bmatrix} \right|^2 = \left| \begin{bmatrix} a-b+j\,\mathrm{Im}\{a\} \\ 2b-j\,\mathrm{Im}\{a\} \end{bmatrix} \right|^2$$

(3.19)

The isolation as a function of Δ/V is plotted in Figure 3-2. For the isolator to achieve at least 15 dB of isolation, Δ/V must be less than 0.13.
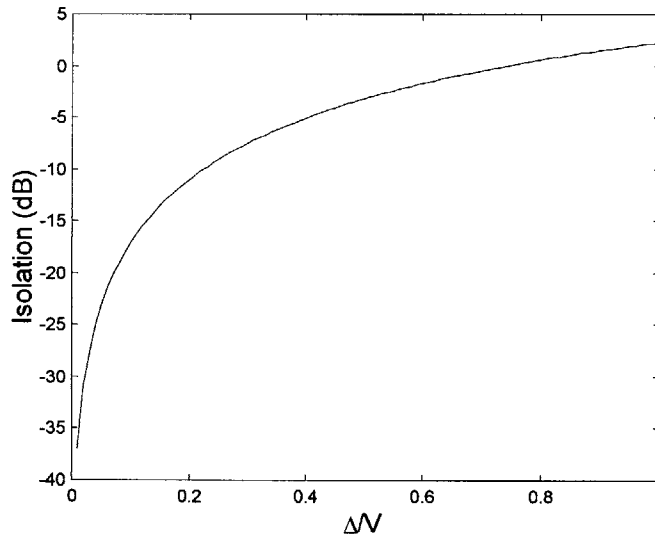
Figure 3-2: Isolation vs. Δ/V

The length of the Faraday rotator is determined by its Verdet coefficient. Based on the results of Chapter 2, the Verdet coefficient is assumed to be 100°/mm for simulations in this chapter, which corresponds to a length of 450 μm for the Faraday

rotator. Using this value for V, Δ must be less than 13 °/mm in order for the isolation to remain below 15 dB. At a wavelength of 1.55 μm, this corresponds to a waveguide birefringence of 1.1 x 10^{-4}, where the waveguide birefringence is defined as the difference in TE and TM mode effective indices (n_{TE}-n_{TM}).

3.1.3 Faraday Rotator Design

Rotationally invariant mode profiles would eliminate the birefringence because then the TE and TM modes would be indistinguishable under a 90° coordinate rotation. By etch-tuning a high-mesa waveguide, the mode profiles can be made rotationally invariant [24]. The high-mesa waveguide consists of a 0.5 μm Fe:$In_{1-x}Ga_xAs_yP_{1-y}$ (x=0.28, y=0.63) core with a 1.0 μm Fe:InP cladding on top and bottom.
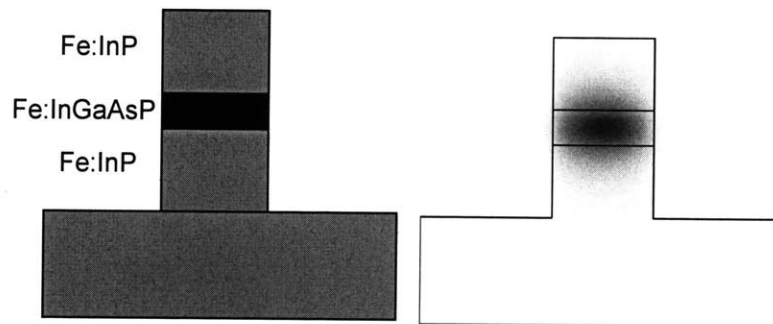
Figure 3-3: High-mesa etched waveguide cross-section and optical mode profile. The waveguide width is 1.4μm, the core thickness is 0.5 μm, and the wavelength is 1.55μm

Figure 3-3 shows the high-mesa waveguide structure and the optical mode profile for a waveguide with a width of 1.4 μm at a wavelength of 1.55 μm. The high-mesa structure has low mode confinement in the vertical direction because of a low index contrast, and high confinement in the horizontal direction because of the high index contrast.

6
4
2
0
-2
-4
-6
-8

$n_{TE} - n_{TM}$ (10^{-4})

1.35 1.36 1.37 1.38 1.39 1.4 1.41 1.42 1.43 1.44 1.45

Width (μm)
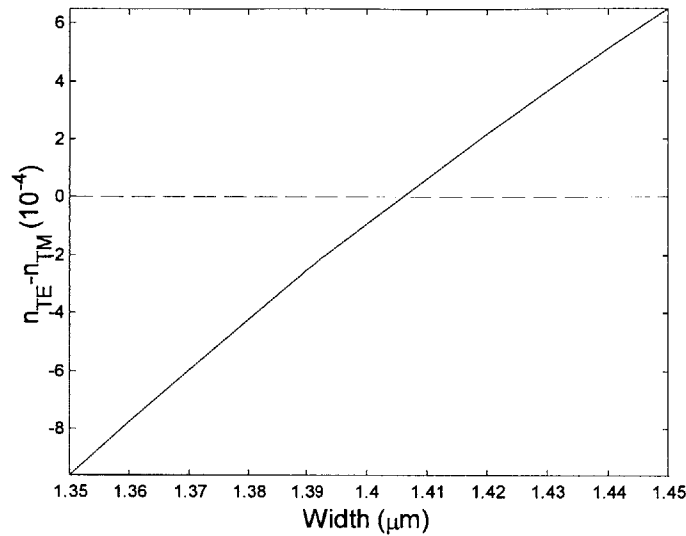
Figure 3-4: Birefringence of Faraday rotator vs. waveguide width at a wavelength of 1.55μm

Tuning the width will tune the mode shape until a rotationally invariant profile is achieved. Figure 3-4 shows the theoretical birefringence as a function of waveguide width at a wavelength of 1.55 μm. To maintain at least 15 dB of isolation, the waveguide width must be accurate to within 0.01 μm.

3.2 Multimode Interferometer

3.2.1 Theory

To achieve the power splitting a multimode interferometer (MMI) is used. This device is a multimode waveguide which utilizes the interference between different modes to achieve the power splitting. The interference between the modes can be used to produce multiple images of the input field along periodic lengths of the waveguide [25]. A general diagram of an MMI is shown in Figure 3-5. In consists of two input and output ports. To function as a 3 dB coupler, light incident on one input port must have its power evenly divided into the two output ports.
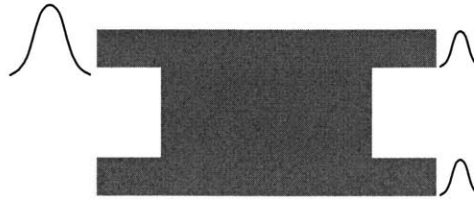
Figure 3-5: General diagram of MMI. Light at the input port on the left has its power evenly divided between the two output ports

For tightly confined modes, the propagation constant for each mode is approximately parabolic with respect to the mode order. The lateral wavenumber k_{mt} and propagation constant β_m are related by the expression

$$k_{mt}^2 + \beta_m^2 = \left(\frac{\omega}{c}n\right)^2 \tag{3.20}$$

where n is the refractive index of the waveguide core and m is the mode order. For tightly confined modes, the lateral wavenumber can be approximated as

$$k_{tm} = \frac{(m+1)\pi}{W} \tag{3.21}$$

where W is the waveguide width. By using Equation 3.21, along with the fact that $k_{mt}^2 << (\omega n/c)^2$, the propagation constant is approximately given by

$$\beta_m \approx \frac{\omega}{c}n - \frac{(m+1)^2\pi^2 c}{\omega W^2} \tag{3.22}$$

This can be rewritten as

$$\beta_m \approx \beta_0 - am(m+2) \tag{3.23}$$

where β_m is the propagation constant of the higher order modes, β_0 is the propagation constant of the zero order mode, and a is given by

$$a = \frac{\pi^2 c}{\omega W^2} \tag{3.24}$$

This parabolic relation of the propagation constant to mode order is the key for an MMI to function properly.

An input mode on one side of the MMI can be expanded in terms of the guided modes of the MMI

$$\psi(x,y,0) = \sum_m c_m \phi_m(x,y)$$ (3.25)

where $\psi(x,y,0)$ is the input field, c_m are the mode excitation coefficients, and $\phi_m(x,y)$ are the modes of the MMI. Because the MMI modes are orthogonal, the mode excitation coefficients are given by

$$c_m = \frac{\int \psi^*(x,y,0)\phi_m(x,y)dA}{\int \phi_m^*(x,y,0)\phi_m(x,y)dA}$$ (3.26)

The field at a distance L will be given by

$$\psi(x,y,L) = \sum_m c_m \phi_m(x,y)e^{-j\beta_m L}$$ (3.27)

which after common phase factors are dropped becomes

$$\psi(x,y,L) = \sum_m c_m \phi_m(x,y)e^{jam(m+2)L}$$ (3.28)

To split the power of the input mode, two images of the input mode must be created. To see how this image creation occurs, the following properties are used:

$$m(m+2) = \begin{cases} even & m = even \\ odd & m = odd \end{cases}$$ (3.29)

and

$$\phi_m(-x,y) = \begin{cases} \phi_m(x,y) & m = even \\ -\phi_m(x,y) & m = odd \end{cases}$$ (3.30)

which comes from the symmetry properties of the MMI modes.

If L is chosen so that

$$L = \frac{\pi}{2a}$$ (3.31)

the propagated field becomes

$$\psi\left(x,y,\frac{\pi}{2a}\right) = \sum_m c_m \phi_m(x,y)e^{jm(m+2)\frac{\pi}{2}}$$ (3.32)

Utilizing the symmetry properties of the modes, this expression can be rewritten as

$$\psi(x,y,\frac{\pi}{2a}) = \sum_{m=even} c_m \phi_m(x,y) - j \sum_{m=odd} c_m \phi_m(x,y)$$

$$= \frac{1-j}{2}\psi(x,y,0) + \frac{1+j}{2}\psi(-x,y,0)$$

(3.33)

This equation represents a pair of images with half of the incident power located at a distance of $\pi/2a$ from the input. This two-fold imaging can be used to make 3 dB couplers.

If the field from Equation 3.33 propagates another $\pi/2a$, the output field will be

$$\psi(x,y,\frac{\pi}{a}) = \sum_{m=even} c_m \phi_m(x,y) - \sum_{m=odd} c_m \phi_m(x,y) = \psi(-x,y,0)$$

(3.34)

which represents the input field at the opposite output port. However, if there is an additional π phase shift introduced between the two field images, then Equation 3.33 can be rewritten as

$$\psi(x,y,\frac{\pi}{2a}) = \sum_{m=odd} c_m \phi_m(x,y) - j \sum_{m=even} c_m \phi_m(x,y)$$

(3.35)

After propagating another $\pi/2a$ distance, the output field will not switch ports:

$$\psi(x,y,\frac{\pi}{a}) = -j \sum_{m=even} c_m \phi_m(x,y) - j \sum_{m=odd} c_m \phi_m(x,y) = \psi(x,y,0)$$

(3.36)

Thus, the addition of a π phase shift to one of the images can be used to control the exit port of the input light.

3.2.2 MMI Limits on Isolation

For a Mach-Zehnder isolator, imbalances in the MMI will ultimately limit the maximum isolation. The imbalance is defined as

$$\eta = \frac{P_1}{P_2} = \frac{\frac{P_0}{2} - (P_1 - P_2)}{\frac{P_0}{2} + (P_1 - P_2)}$$

(3.37)

P_1 and P_2 are the powers in the two output ports of the MMI and P_0 is the total input power. In order to calculate the maximum possible isolation, it is assumed that the second MMI in the isolator has no imbalance. Then the balanced power would all be sent to the port where no isolation is required and the unbalanced power would be divided evenly between both ports. Thus, in the port where isolation is desired, there would be half of the imbalanced power. The maximum isolation, which is the normalized power in the port where isolation is desired, can be expressed as

$$Isolation = \frac{P_1 - P_2}{2P_0} = \frac{1}{4}\frac{1-\eta}{1+\eta} \tag{3.38}$$

Figure 3-6 shows the isolation versus imbalance. In order to have 20 dB isolation, the imbalance must be below 0.33 dB.
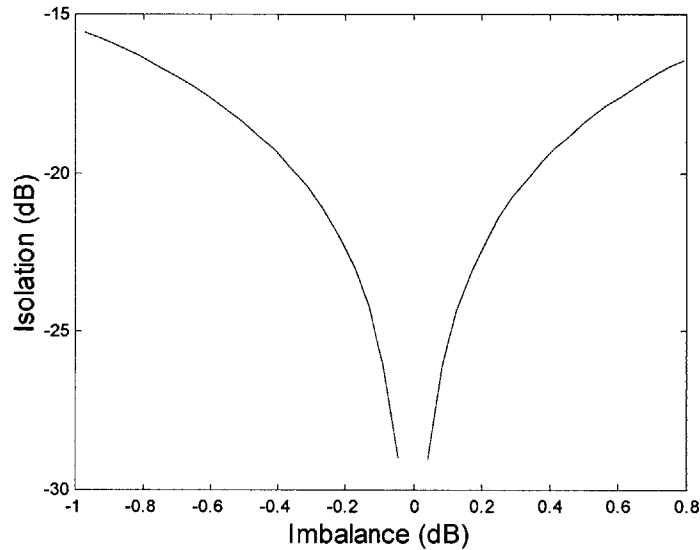
Figure 3-6: Isolation vs. MMI imbalance

3.2.3 MMI Design

The MMI was designed to accommodate the 1.4μm wide waveguide Faraday rotators, while simultaneously minimizing its length. The MMI possesses the same epitaxial layers as the Faraday rotator and the width was chosen to be 3.4 μm. There were four guided modes for both TE and TM polarizations. Figure 3-7 shows the guided TE mode profiles. The TM modes are very similar to the TE modes, and so are not

shown here. Because the MMI was birefringent, the TE and TM modes had different lengths for optimal power splitting.
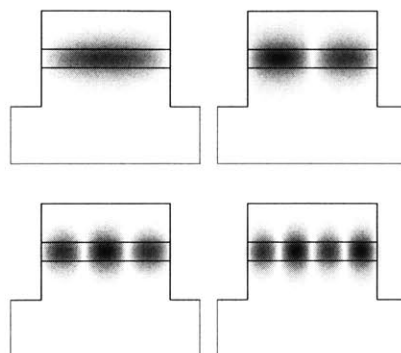
Figure 3-7: MMI TE mode profiles

The power imbalance versus MMI length at 1.55 μm was calculated using an eigenmode propagation code (see Appendix B), and the results are shown in Figure 3-8. The length for minimum imbalance for both polarizations is 52 μm. At this length, the minimum imbalances of both TE and TM polarizations are 0.06 dB, which limits the maximum isolation to 27.6 dB.
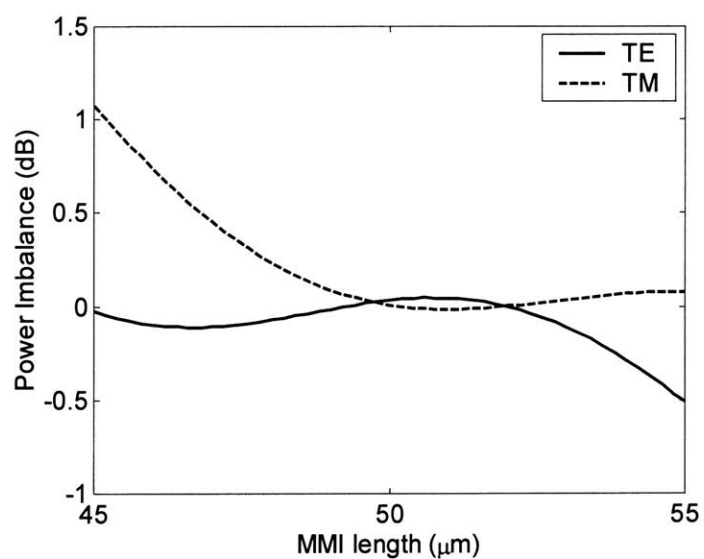
Figure 3-8: MMI imbalance vs. length for TE and TM polarizations at a wavelength of 1.55μm

3.3 Half-Wave Plate

3.3.1 Half-wave Plate Limits on Isolation

To analyze the effect of any error in the half-wave plate axes, the Jones' matrix formalism is used. For this analysis, it is assumed that the slow-axes of the half-wave plates in each arm of the isolator are at θ and $-\theta$. As shown in Appendix A, the Jones' matrix for an arbitrary half-wave plate with slow-axis angle θ is

$$HWP = \begin{bmatrix} \cos(2\theta) & \sin(2\theta) \\ \sin(2\theta) & -\cos(2\theta) \end{bmatrix} \tag{3.39}$$

In the forward direction, the overall Jones matrix for each arm is

$$A_1 = HWP(\theta) * FR = \frac{1}{\sqrt{2}} \begin{bmatrix} \cos(2\theta) + \sin(2\theta) & -\cos(2\theta) + \sin(2\theta) \\ -\cos(2\theta) + \sin(2\theta) & -\cos(2\theta) - \sin(2\theta) \end{bmatrix} \tag{3.40}$$

$$A_2 = FR * HWP(-\theta) = \frac{1}{\sqrt{2}} \begin{bmatrix} \cos(2\theta) + \sin(2\theta) & \cos(2\theta) - \sin(2\theta) \\ \cos(2\theta) - \sin(2\theta) & -\cos(2\theta) - \sin(2\theta) \end{bmatrix} \tag{3.41}$$

In the reverse direction, the Jones' matrices of the two arms are

$$A_1 = FR * HWP(\theta) = \frac{1}{\sqrt{2}} \begin{bmatrix} \cos(2\theta) - \sin(2\theta) & \cos(2\theta) + \sin(2\theta) \\ \cos(2\theta) + \sin(2\theta) & -\cos(2\theta) + \sin(2\theta) \end{bmatrix} \tag{3.42}$$

$$A_2 = HWP(-\theta) * FR = \frac{1}{\sqrt{2}} \begin{bmatrix} \cos(2\theta) - \sin(2\theta) & -\cos(2\theta) - \sin(2\theta) \\ -\cos(2\theta) - \sin(2\theta) & -\cos(2\theta) + \sin(2\theta) \end{bmatrix} \tag{3.43}$$

When the reverse Jones' matrices are added together, the result is

$$A_1 + A_2 = \sqrt{2} \begin{bmatrix} \cos(2\theta) - \sin(2\theta) & 0 \\ 0 & -\cos(2\theta) + \sin(2\theta) \end{bmatrix} \tag{3.44}$$

Following the same method as Equation 3.19, the maximum isolation with perfect 3 dB couplers will be

$$Isolation = 2|\cos(2\theta) - \sin(2\theta)|^2 = 2(1 - \sin(4\theta)) \qquad (3.45)$$

Figure 3-9 shows the isolation versus θ. The slow axis angle is 22.5° for the ideal case, but to have an isolation of at least 20 dB, deviations of $\pm1.4°$ can be tolerated.
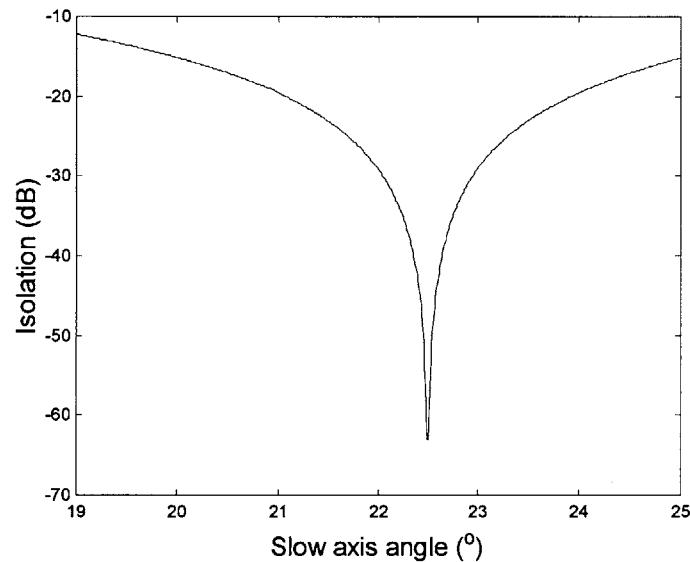
Figure 3-9: Isolation vs. HWP slow-axis angle

3.3.2 Half-Wave Plate Design

The isolator requires two different half wave plates with slow axes at 22.5°and -22.5° with respect to the TE axis in order to provide a reciprocal 45° rotation. To achieve intergrated half-wave plates, a birefringent waveguide is needed which has its principal axes not aligned to the TE and TM axes.

If a notch is etched on top of the Faraday rotator structure's upper cladding, as shown in Figure 3-10, the symmetry which decouples TE and TM modes will be broken. The effect of this notch is to couple these modes, creating new eigenmode polarizations. These polarizations will define the slow- and fast-axes of the waveguide half-wave plate. The slow-axis corresponds to the polarization of the eigenmode with the larger effective index. By controlling the width of the notch, the slow-axis angle can be controlled. In

order to change the sign of the slow-axis angle for the second half-wave plate in the isolator, the notch simply needs to be etched on the opposite side of the waveguide.
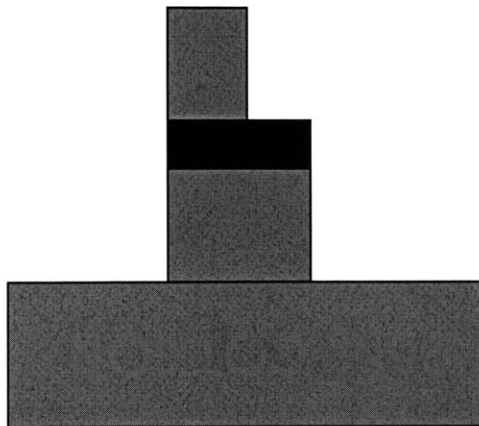
Figure 3-10: Waveguide HWP cross-section. The notch on top of the core couples TE and TM polarizations, creating new eigenmode polarizations which are no longer TE or TM

To function as a half-wave plate, the waveguide must also provide a π phase shift between the two eigenmodes. The length of the half-wave plate is defined as

$$L_{HWP} = \frac{\pi}{\beta_s - \beta_f} = \frac{\lambda}{2(n_s - n_f)} \tag{3.46}$$

where β is the propagation constant of the fast- and slow-axis modes, n is the effective indices of the modes, and λ is the wavelength. The graph in Figure 3-11 shows the slow axis angle as a function of notch width, and also the corresponding waveguide length to achieve the π phase shift. At 1.55 μm, a notch width of 0.85 μm and waveguide length of 158 μm will give the required half-wave plate functionality. Because there is only 1.4° tolerance in the slow axis angle, the corresponding tolerance on notch width is 0.05 μm.
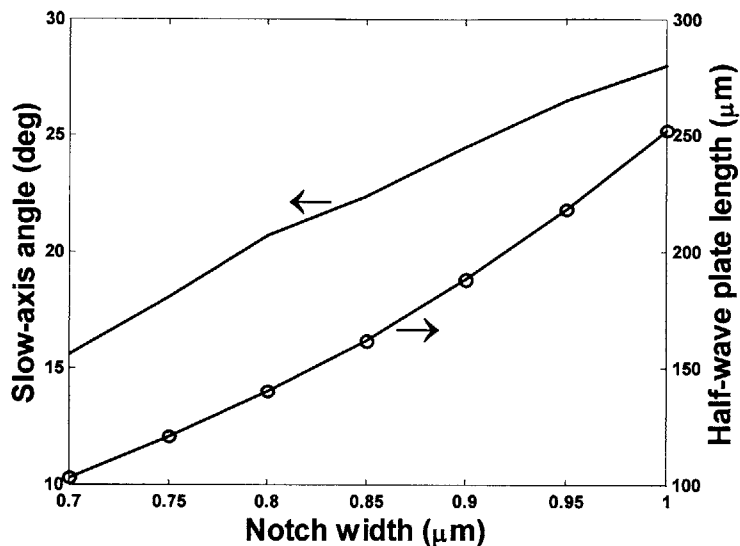
Figure 3-11: Slow axis angle and length of HWP vs. notch width at a wavelength of 1.55 μm

3.4 Isolator Simulation

Figure 3-12 shows a top and cross-sectional view of the isolator, with the arrows indicating where light enters and leaves. The length of the isolator, which is given by the sum of the lengths of each individual component, is 712 μm. The longest component is the Faraday rotator, but this length can be changed if the Verdet coefficient is further increased.
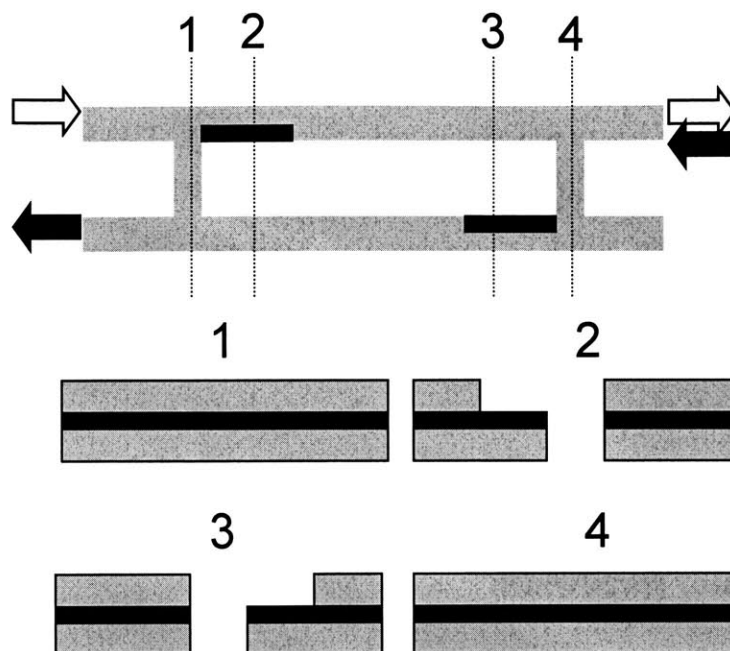
Figure 3-12: Top and cross-sectional view of isolator

With all components now designed in integrated form, the next step is to evaluate the performance of he isolator. Conventional photonic design software could not be used to simulate the isolator because of the non-reciprocal Faraday rotator. In order to simulate the circulator, an eigenmode propagation code was written which could support non-reciprocal structures. Further details on this code can be found in Appendix B.

3.4.1 Reflections at Junctions

Before simulating the entire isolator, there was one concern, which was the effect of reflections at the junctions of the different components. The reflections at the junctions can be estimated using the Fresnel reflection. The Fresnel power reflection coefficient at the junction of waveguide 1 and waveguide 2 is defined as:

$$R = \left| \frac{n_2 - n_1}{n_2 + n_1} \right|^2 \tag{3.47}$$

where n is the effective index of each waveguide. With this formula, the reflections at the junctions of the different structures were calculated.

It was expected that the reflections would be minimal because the mode indices are very similar in value, so reflections due to index discontinuities will be negligible. It was found that the all the power reflections were below 60 dB. This is negligible because the isolation is theoretically limited to 27.6 dB just by the MMI imbalance.

Simulations done using a commercial photonic design software package [Fimmwave and Fimmprop from Photon Design®] also showed that the power reflections at the junctions were negligible. At the Faraday rotator/half-wave plate junction and at the Faraday rotator/MMI junction the power reflections were below 60 dB. This agrees with the Fresnel reflection calculated by using the effective mode indices.

3.4.2 Isolator Bandwidth

The isolator bandwidth was simulated using the eigenmode propagation code in Appendix A, and the results are shown in Fig. 3-14. For this simulation, the insertion loss is defined as the power in the top left port when the input is from the top right port, and the isolation is defined as the power in the top right port when the input is from the top left port, as illustrated in Figure 3-12. This will be known as the isolator configuration.

When the isolator is used in this manner, its isolation will be maximized. This is because in the forward direction, the outputs of the two arms are in phase and are less sensitive to any deviations from the ideal specifications for the half-wave plate and Faraday rotator. However, in the reverse direction, because a precise π phase shift between the two arms is needed, the isolator will be much more sensitive to these deviations. These deviations will then manifest not as a reduction in isolation, which is the important specification for the isolator, but rather as insertion loss. If the isolator is to be used as a circulator, then all four ports are active and the isolation will not be as robust, but if it is used only as an isolator, then only two ports are active and it will achieve much better performance.

To quantify how much more robust the device is in the isolator configuration, the Jones' matrix formalism is used. The Faraday rotator limit on isolation is found by

taking the difference Jones' matrices for the forward direction found in Equations 3.14 and 3.15:

$$Isolation = \left|(A_1 - A_2)\frac{1}{\sqrt{2}}\begin{bmatrix}1\\1\end{bmatrix}\right|^2 = \left|\begin{bmatrix}\text{Re}\{a\}-b\\\text{Re}\{a\}-b\end{bmatrix}\right|^2 = 2(\text{Re}\{a\}-b)^2 \tag{3.48}$$

The half-wave plates' limit on isolation can be found in the same manner using Equations 3.40 and 3.41:

$$Isolation = \left|(A_1 - A_2)\frac{1}{\sqrt{2}}\begin{bmatrix}1\\1\end{bmatrix}\right|^2 = \left|(\sin(2\theta)-\cos(2\theta))\begin{bmatrix}1\\1\end{bmatrix}\right|^2 = 2(1-\sin(4\theta))^2 \tag{3.49}$$

This expression is identical to the isolation limit set by the half-wave plate in the opposite configuration.

Unlike with the half-wave plate, the isolation limit set by the Faraday rotator in the isolator configuration is different from the opposite configuration. The isolation limit of the Faraday rotator is shown in Figure 3-13. Now to have 15 dB of isolation, Δ/V must now be less than 0.8. This requires the waveguide width must be accurate to within 0.04 μm, which is four times the tolerance as the opposite configuration.
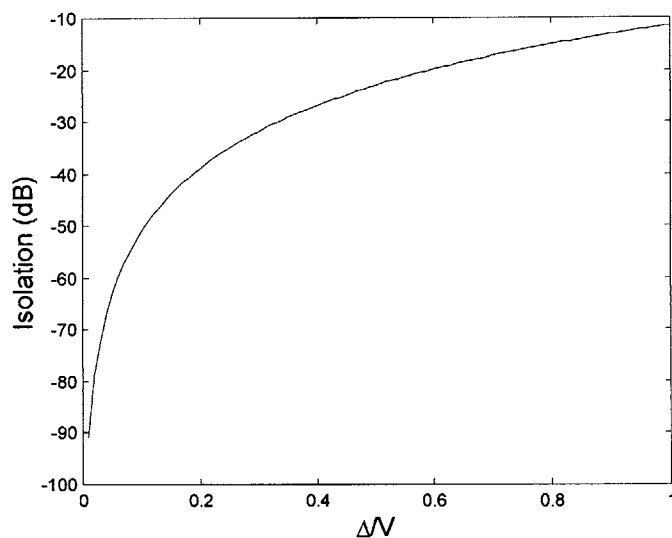
Figure 3-13: Isolation vs Δ/V for isolator configuration

The maximum isolation is 24 dB at 1.55 μm, which is the wavelength for which the isolator was optimized. It maintains 12 dB of isolation over a 100 nm bandwidth, for

both TE and TM polarizations, thus showing that it is truly polarization independent. The insertion loss is 1.4 dB at 1.55 μm, and stays below 5 dB over a 100 nm bandwidth. The factors that limit the bandwidth are the imbalance of the MMI, the birefringence of the Faraday rotator, and deviations of the half-wave plate slow axis angle. To understand which element is the limiting factor, each individual component's bandwidth was analyzed.
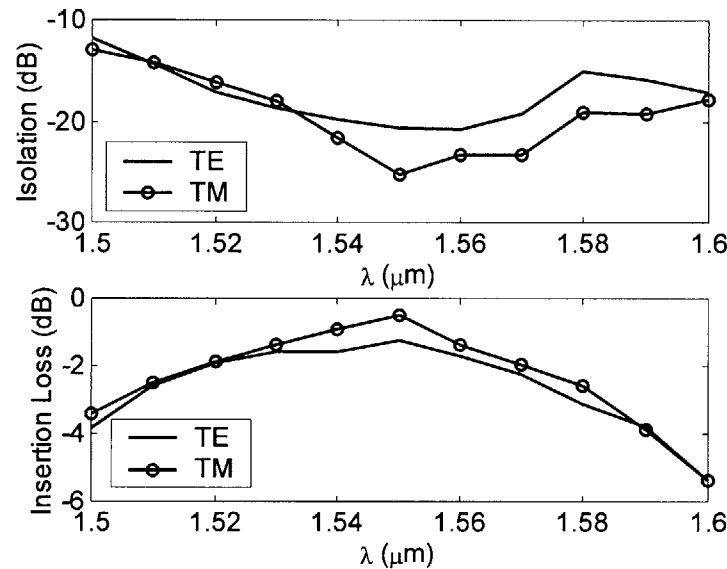
Figure 3-14: Theoretical isolation and insertion loss of isolator

For the MMI, the isolation due to the imbalance versus wavelength is shown in Figure 3-15. The isolation increase at 1.60 μm can be explained by the fact that at this wavelength the imbalance is lower, but the loss is higher. Therefore, the isolation will increase because the MMI splits the power evenly in the two arms, but there is also power which never enters either arm, which will increase the loss. The isolation does not vary by more than 3 dB over the entire bandwidth and remains below 24 dB. This is because the MMI is not extremely wavelength dependent and maintains a low imbalance over the entire simulation bandwidth. Therefore, it is not the element which limits the bandwidth, but it does limit the maximum isolation.
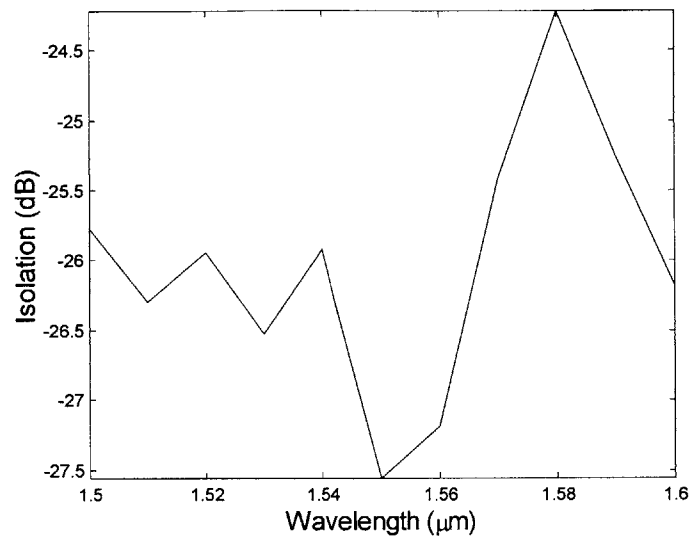
Figure 3-15: Isolation due to MMI imbalance vs. wavelength

The maximum isolation due to the slow-axis angle of the half-wave plate versus wavelength is shown in Figure 3-16. The minimum isolation occurs at 1.56 μm instead of 1.55μm. This is because the slow-axis angle is actually closer to 22.5° at this wavelength. When designing the half-wave plate, the step size used for the notch width was too large to exactly achieve the ideal angle. However, by tuning the wavelength, the index of refraction changes were small enough to come very close to 22.5°. It can also be seen that the isolation shows a strong wavelength dependence, which is due to the slow-axis angle being very sensitive to wavelength.
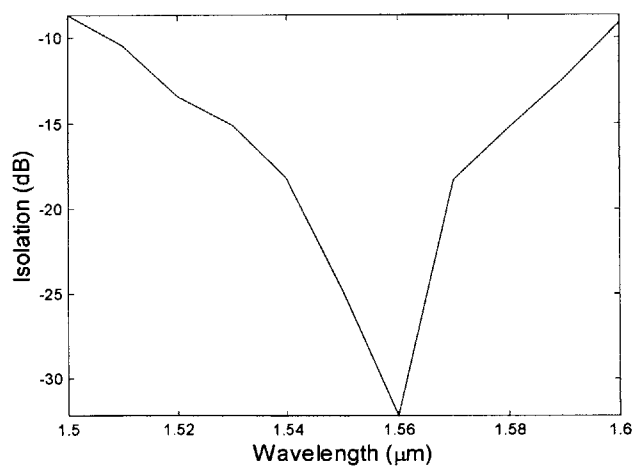
Figure 3-16: Isolation due to slow-axis angle deviations vs. wavelength

The maximum isolation due to the Faraday rotator birefringence is plotted in Figure 3-17. The maximum isolation is at 1.55 μm, but as can be seen, the isolation shows a strong wavelength dependence. This is because the birefringence is very sensitive to wavelength. However, by increasing the Verdet coefficient, a larger birefringence can be tolerated.
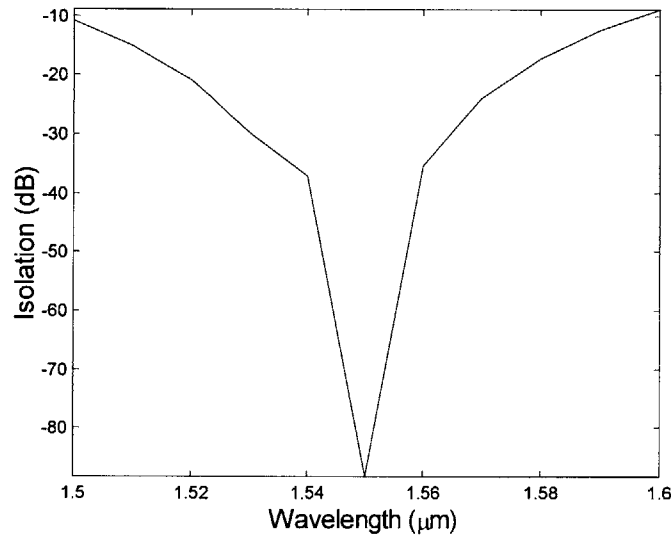
Figure 3-17: Isolation due to Faraday rotator birefringence vs. wavelength

3.5 Summary

The isolator design presented in this chapter showed a maximum isolation of 24 dB. This limit was set mainly by the imbalance of the MMI's. The isolator is fully integrated and is less than 1 mm in length. The design is very general and not limited to InP/InGaAsP systems. The concepts used to design each component are very simple and applicable to any material platform. Thus, what has been shown in this chapter is a very general design for a polarization independent, integrated optical isolator which can also function as an optical circulator.

The dimension where fabrication tolerances are strictest is the width. For the HWP's, the tolerances are determined by the operational wavelength and the refractive

indices of the materials. However, the Faraday rotator's width tolerance can be reduced if the Verdet coefficient can be increased. As discussed in Chapter 2, the Verdet coefficient of Fe:InGaAsP can be increased by increasing the magnetic doping or reducing the bandgap. Other advantages of increasing the Verdet coefficient include reducing the isolator length and increasing the performance bandwidth. The important thing to note is that if the isolator is used in the configuration shown in Figure 3-12, then the tolerances are relaxed on the Faraday rotator. However, if it is used as a circulator, the strict tolerances will be necessary for proper function.

With the design now complete, the next step is the fabrication of the isolator. Chapter 4 deals with the fabrication and characterization of the waveguide Faraday rotator.

Chapter 4

Waveguide Measurements

There were three measurements which were made on the waveguide Faraday rotator: optical loss, birefringence, and Faraday rotation. This chapter will begin with a description of the fabrication of the waveguides. Then the theory for each measurement will be discussed. The experimental setup and technique for each measurement will then be described. Finally, results will be presented for these measurements.

4.1 Fabrication

The waveguide was fabricated with low pressure methane based reactive ion etching with a 300 nm thick Ti mask. $CH_4/H_2/O_2$ with ratios 25:30:0.5, 100W RF power, and a chamber pressure 8.5 mTorr were used for the etching. A 2.5μm deep etch required 50 minutes etching in our system. Figure 4-1 shows a picture of the fabricated high-mesa waveguide with a width of 1.4μm and an etching depth of 2.5μm. The InGaAsP core is 0.5 μm thick and the top and bottom InP claddings are 1.0 μm thick. The etching surface is fairly smooth. The waveguides were cleaved in order to make the end-facets. All waveguide fabrication was done by Xiaoyun Guo.
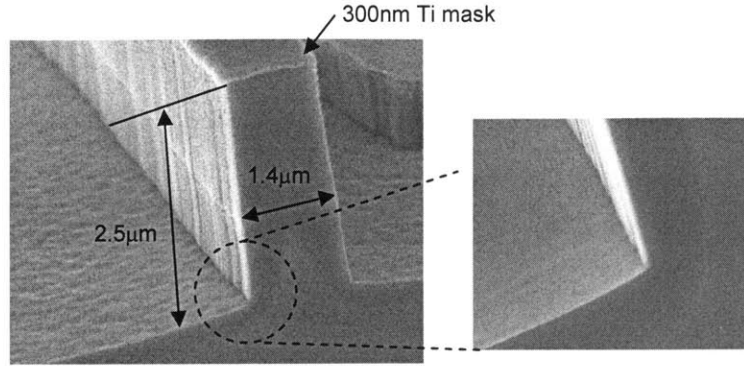
Figure 4-1: Etched waveguide with 300nm Ti mask. The enlarged picture of the etched surface shows that it is smooth. The line shown in the mesa surface is due to the oxygen ashing in the middle of the processing.

4.2 Theory

4.2.1 Loss Measurement

The reflective end facets of a waveguide will create an optical cavity. The expression for the transmission through an optical cavity which was derived in Chapter 2 is

$$E_t = E_o t^2 e^{-j\beta l}\left(1 + r^2 e^{-j2\beta l} + \left(r^2 e^{-j2\beta l}\right)^2 + ...\right) = \frac{E_o t^2 e^{-j\beta l}}{1 - r^2 e^{-j2\beta l}} \tag{4.1}$$

where l is the cavity length, t and r are the field transmission and reflection coefficients, and β is the propagation constant. For a waveguide with loss, the propagation constant is a complex number with the imaginary part corresponding to the loss. Equation 4.1 can be rewritten as

$$E_t = E_o t^2 e^{-j\beta l} e^{-\frac{\alpha}{2}l}\left(1 + r^2 e^{-j2\beta l} + \left(r^2 e^{-j2\beta l}\right)^2 + ...\right) = \frac{E_o t^2 e^{-j\beta l} e^{-\frac{\alpha}{2}l}}{1 - r^2 e^{-j2\beta_r l} e^{-\alpha l}} \tag{4.2}$$

where the propagation constant has been written as

$$\beta = \beta_r - j\frac{\alpha}{2} \tag{4.3}$$

The absorption coefficient is α because it corresponds to the power absorption which is proportional to $|E_t|^2$.

The ratio of the square-root of the transmitted power on-resonance to the transmitted power off-resonance is then

$$F = \sqrt{\frac{P_{max}}{P_{min}}} = \frac{1 + Re^{-\alpha l}}{1 - Re^{-\alpha l}} \tag{4.4}$$

where r^2 has been rewritten as the power reflection coefficient, R. Solving this expression for α gives

$$\alpha = \frac{\ln(R) - \ln\left(\frac{F-1}{F+1}\right)}{l} \tag{4.5}$$

To calculate R, the Fresnel equations can be used:

$$R = \left|\frac{n_2 - n_1}{n_2 + n_1}\right|^2 \tag{4.6}$$

Here n_1 is the index of refraction of the external medium, which is air for the waveguide measurements, and n_2 is the effective index of the waveguide mode. The effective index of the mode can be calculated using the separation of the resonant peaks for the mode. If two adjacent peaks for the mode occur at wavelengths λ_1 and λ_2, then the resonance condition for each peak becomes

$$2nl = m\lambda_1 \tag{4.7}$$

$$2nl = (m+1)\lambda_2 \tag{4.8}$$

where m is the order of the resonance. The second equation comes from the fact that the order of adjacent peaks differs by one. Solving these equations for n gives

$$n = \frac{1}{2l}\frac{\lambda_1 \lambda_2}{\lambda_2 - \lambda_1} \tag{4.9}$$

With this result, along with Equations 4.5 and 4.6, the waveguide loss can be calculated.

4.2.2 Birefringence Measurement

To calculate the birefringence in the Faraday rotator, the effects of the cavity are used. Resonances will occur whenever the roundtrip phase through the cavity is 2π. If the propagation constant is written as

$$\beta = \frac{2\pi}{\lambda} n \qquad (4.10)$$

then the transmitted field can becomes

$$E_t = \frac{E_0 t^2}{1 - r^2 e^{-j\frac{4\pi}{\lambda} nl}} \qquad (4.11)$$

If there is birefringence in a waveguide, then the index of refraction will be different for the TE and TM modes. This will cause the resonance peaks to occur at different wavelengths for the two polarizations. The TM effective index can be written as

$$n_{TM} = n_{TE} + \Delta n \qquad (4.12)$$

where Δn is the birefringence. The condition for the resonance of each mode is

$$2n_{TE} l = m\lambda_{TE} \qquad (4.13)$$

$$2(n_{TE} + \Delta n)l = m\lambda_{TM} \qquad (4.14)$$

where λ_{TE} and λ_{TM} are the wavelengths for the two modes where the resonance occurs. In order to solve for the birefringence, the resonance order must be known. If it is assumed that it is the same for two adjacent resonant peaks, then the birefringence is given by

$$\Delta n = n_{TE}\left(\frac{\lambda_{TM}}{\lambda_{TE}} - 1\right) \qquad (4.15)$$

By using this equation along with Equation 4.9 for n_{TE}, the birefringence of the waveguide can be calculated.

The main problem with this measurement technique is that if the birefringence is too large, the adjacent TE and TM peaks will not be of the same order. To see how large the birefringence must be for this to occur, it is assumed that the peaks occur at the same wavelength, but differ in order by one, which can be written as

$$2n_{TE} l = m\lambda \qquad (4.16)$$

$$2(n_{TE} + \Delta n)l = (m+1)\lambda \qquad (4.17)$$

Solving this for Δn gives

$$\Delta n = \frac{\lambda}{l} \qquad (4.18)$$

To see the numerical value for the birefringence limit, typical values of the parameters for the Faraday rotator waveguides used in the measurement are used (l=500μm, λ=1.55μm). With these values, the maximum limit on Δn becomes 3.1 x 10^{-3}. For measurements done between 1.50 μm and 1.60 μm, Δn does not go beyond 10^{-3} for the 1.4 μm wide Faraday rotator. Also, Δn is below 3 x 10^{-3} at 1.55 μm if the Faraday rotator width remains between 1.3 μm and 1.6 μm. As long as the width of the waveguide is within this range, the birefringence can be accurately measured with the technique described in this section.

4.2.3 Faraday Rotation Measurement

The Faraday rotation in waveguides is measured in the same way as in bulk samples. The input light is linearly polarized at 45°, and the output light is separated into TE and TM components. The difference with waveguides is that there is birefringence present. Using Equation 3.8, the output light will be

$$\overline{E_t} = \begin{bmatrix} \cos(\psi L) + j\frac{\Delta}{\psi}\sin(\psi L) & -\frac{V}{\psi}\sin(\psi L) \\ \frac{V}{\psi}\sin(\psi L) & \cos(\psi L) - j\frac{\Delta}{\psi}\sin(\psi L) \end{bmatrix} \frac{1}{\sqrt{2}}\begin{bmatrix} 1 \\ 1 \end{bmatrix} = $$

$$\frac{1}{\sqrt{2}}\begin{bmatrix} \cos(\psi L) - \left(\frac{V - j\Delta}{\psi}\right)\sin(\psi L) \\ \cos(\psi L) + \left(\frac{V - j\Delta}{\psi}\right)\sin(\psi L) \end{bmatrix}$$

(4.19)

where V is the Verdet coefficient and the other variables are defined as

$$\Delta = \frac{\beta_{TE} - \beta_{TM}}{2}$$

(4.20)

$$\psi = \sqrt{\Delta^2 + V^2}$$

(4.21)

The difference in TE and TM power is then

$$dP = -\frac{V}{\psi}\sin(2\psi l)$$

(4.22)

In order to minimize the effect of any errors in the input polarization, the measurement is done for both positive and negative magnetic field. The resulting difference in these two powers is then

$$dP^+ - dP^- = -4\frac{V}{\psi}\sin(2\psi l) = -\frac{2}{\sqrt{1+\left(\frac{\Delta}{V}\right)^2}}\sin\left(2Vl\sqrt{1+\left(\frac{\Delta}{V}\right)^2}\right) \qquad (4.23)$$

From Equation 4.22 it can be seen that if $\Delta \gg V$, then the measured signal will approach zero.

To see what the Faraday rotation spectrum will look like for a waveguide, simulation plots are shown if Figure 4-2. The plots show the expected Faraday rotation versus wavelength for different width waveguides. The Verdet coefficient is assumed to be 10 °/mm for the waveguides and the length is assumed to be 500 μm. The Verdet coefficient is lower than the value used for the simulations in Chapter 3 because the maximum magnetic field for the waveguide measurements is 0.1 T. The effective indices used for the simulation were calculated with the 2-D mode solver used for the simulations in Chapter 3. As can be seen from the plots, the rotation is a maximum when the birefringence is zero, and it drops off as the wavelength deviates from the zero-birefringence wavelength. In order to be able to see rotation within the wavelength range available for the measurements, the width of the waveguide must be between 1.35 μm and 1.50 μm. The maximum measured rotation can be used as the cavity-enhanced rotation and Equation 2.61 can be used to extract the single-pass rotation.
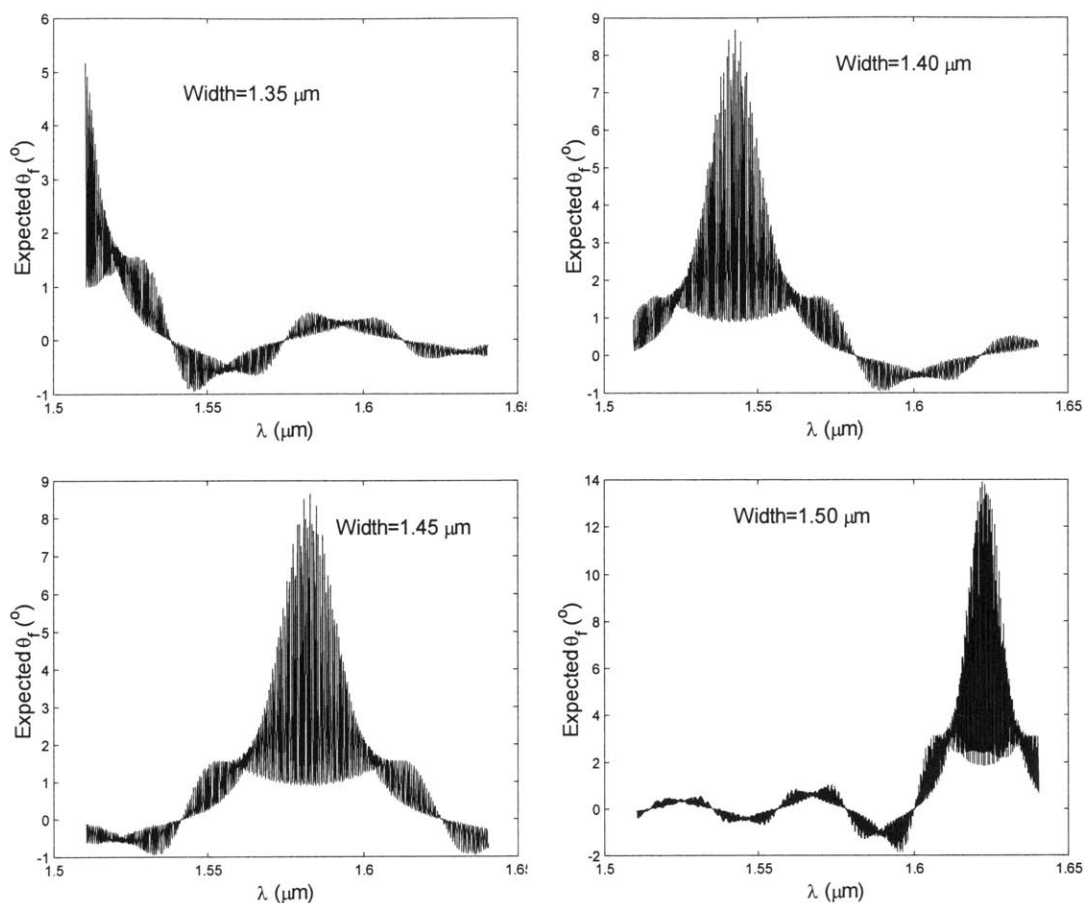
Figure 4-2: Simulation of expected Faraday rotation vs wavelength for different waveguide widths. The Verdet coefficient is 10°/mm and the cavity length is 500 μm for the simulation

4.3 Experimental Setup

To measure the waveguide properties, there are three problems which must be solved. First is coupling light into the waveguide, second is controlling the input polarization, and third is detecting the output power. Each problem will be discussed in detail in the following sections.

4.3.1 Coupling to Waveguide

To couple light into the waveguide, a polarization maintaining (PM) lensed fiber is used. The difficulty in coupling to the waveguide is that because it is so small, precise alignment and incredible stability of the fiber and waveguide is needed. The size of the optical mode is approximately 1 μm^2, so the position of the fiber must be able to be controlled with sub-micron accuracy. This was accomplished mounting the fiber on a piezo-electric translation stage which had an accuracy of 10 nm.

To determine if the fiber had coupled to the waveguide mode, a 100x microscope objective and an infrared camera were used to image the end facet of the waveguide. The first step was to raise the fiber above the waveguide and align it with the end facet. Then the lens was adjusted until the spot from the fiber came into focus on the camera. The fiber was then pulled back and the waveguide was raised up until it aligned with the fiber. The light usually coupled to the substrate modes of the waveguide, which indicated that the waveguide is too high. It was lowered until the substrate modes disappeared, but not lowered so much that the light passed over the top of the waveguide. It is in this dark region between air and substrate the guided mode existed. Next the fiber was moved closer to the waveguide and moved vertically and horizontally with the piezo-electric stage until the mode appeared on the infrared camera. A picture of the substrate mode and optical mode from one of the Faraday rotator waveguides is shown in Figure 4-3.
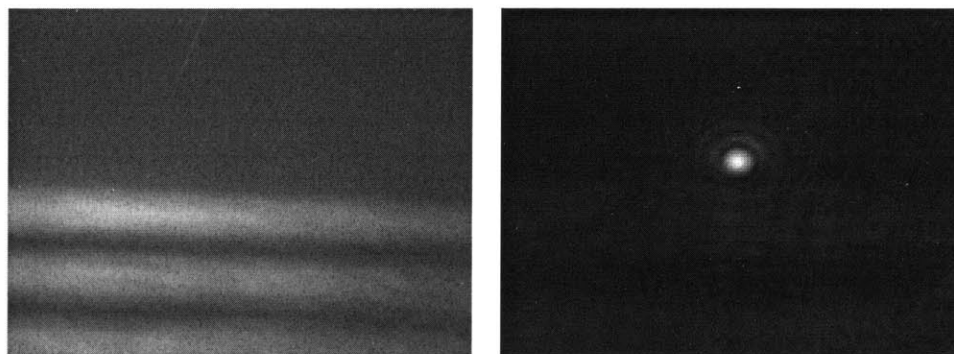
Figure 4-3: Substrate mode (left) and optical mode (right) of waveguide Faraday rotator

In order to easily find the mode, it is important to make sure that the end facet of the waveguide is properly imaged on the camera. When the mode is difficult to find, it is because the focus is incorrect. Once the light couples to the mode, measurements can be made on the waveguide.

The beam from the lensed fiber has a nominal radius of 1.25 μm. By approximating the beam as a Gaussian, the mode overlap of the beam with the mode can be expressed as

$$c = \frac{\iint e^{-\frac{x^2+y^2}{2s^2}} \phi(x,y)dxdy}{\iint e^{-\frac{x^2+y^2}{s^2}} dxdy} \qquad (4.24)$$

where ϕ is the waveguide mode profile normalized to have unity power and s is the beam radius. The power coupling efficiency of the beam with the waveguide mode, which is defined as c^2, is 26 %. The actual coupling efficiency for the waveguides is 2 %. This may be due to the actual beam radius being deviating from the nominal value. Damage to the fiber lens may be the cause of this deviation.

4.3.2 Controlling Input Polarization

For the Faraday rotation measurements, the input light must be linearly polarized at 45°. For bulk measurements this could be easily achieved with a polarizer. The difficulty in waveguide measurements is that the light comes from a fiber. Ordinary fibers are birefringent due to stress caused by bending. This birefringence will alter the state of the light and make it difficult to have any sort of polarization control. In order to solve the issue of stress induced birefringence, a polarization maintaining (PM) fiber is used. PM fiber is fiber that is already stressed so that the birefringence is fixed and will not be changed by any bending. The principle axes of PM fiber are also fixed. In order to have linearly polarized light at the output of the fiber, linearly polarized light must be launched into the fiber with its polarization aligned with one of the principle axes.
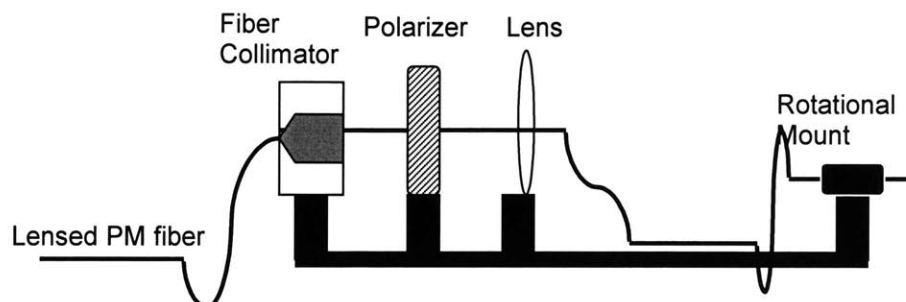
Figure 4-4: Setup for controlling polarization of light from PM fiber

The setup for coupling into the PM fiber is shown in Figure 4-4. The light is sent out of a fiber collimator and then passed through a polarizer with 50 dB of extinction. The polarizer can be rotated until it aligns with one of the principle axes of the fiber. Another lens is then used to couple the polarized light into the PM fiber. To control the angle of the polarization at the output of the fiber, a rotational mount is used to hold the fiber. It can then be rotated to any desired angle.

4.3.3 Detecting Output Power

There are two main difficulties associated with detecting the optical power from the waveguide. First, because of low coupling efficiency between the waveguide and fiber, the power is generally no larger than 1 μW. Second, any small drifting of the fiber will change the amount of power coupling into the mode, and creating an unstable power signal.

In order to measure the powers in the TE and TM modes, two photodetectors were built. The circuit diagram for the detectors is shown in Figure 4-5. They consist of an FDG05 Ge photodiode from Thorlabs, an LT1028 ultralow noise precision high speed op-amp from Linear Technology, and a feedback resistor.
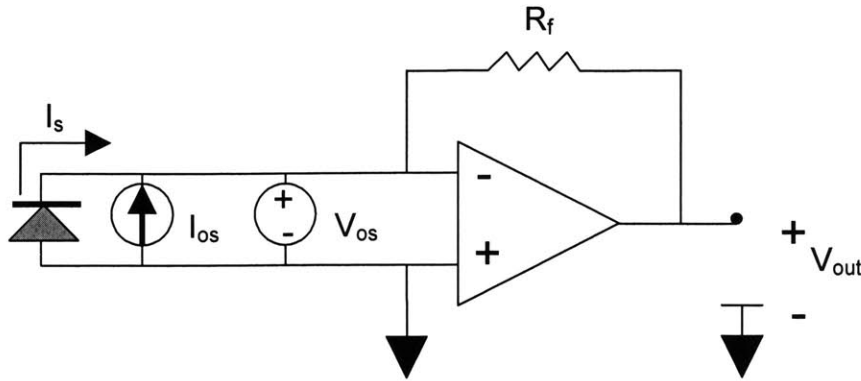
Figure 4-5: Circuit diagram for photodetector

The amplifiers were not ideal and had two important factors which affected the measurement: input offset voltage and input offset current. These can be modeled as a voltage source V_{os} and current source I_{os} across the inputs of the amplifier, as shown in Figure 4-5. The photodiode in Figure 4-5 has a signal current I_s and the value of the feedback resistor across the amplifier is R_f. The output voltage V_{out} of the amplifier will be given by

$$V_{out} = -I_s R_f + V_{os} - I_{os} R_f \qquad (4.25)$$

The voltage signal due to the power from the TE and TM modes of the Faraday rotator can be written as a Jones' matrix:

$$\overline{V_{out}} = \frac{1}{2}\begin{bmatrix} V_o(1 - \sin(2\theta)) + \delta_1 \\ V_o(1 - \sin(2\theta)) + \delta_2 \end{bmatrix} \qquad (4.26)$$

where δ_1 and δ_2 are the offset output voltages in the two amplifiers and V_o is the voltage due to the total optical power. The normalized difference in the two voltages is then

$$dV = \frac{-\sin(2\theta) + \dfrac{\delta_1 - \delta_2}{2V_o}}{1 + \dfrac{\delta_1 + \delta_2}{2V_o}} \qquad (4.27)$$

By subtracting the voltage differences for positive and negative magnetic fields, the resulting signal is

$$dV^+ - dV^- = \frac{-2\sin(2\theta)}{1 + \dfrac{\delta_1 + \delta_2}{2V_o}} \qquad (4.28)$$

In the limit where δ_1 and δ_2 are much smaller than the signal voltage V_o, this expression will reduce to the ideal case. However, if they are comparable to V_o, then the measured dV will be erroneous. Thus, it is desirable if the signal term I_sR_f is much larger than the other offset terms.

Typical values of I_{os} and V_{os} for the LT1028 op-amp are 20 μV and 18 nA. If a 100 kΩ resistor is used for R_f, then a 1 μW signal will result in a 100 mV signal, while the offset voltages will be less than 2 mV. Therefore, by using the LT1028 op-amp with a 100 kΩ feedback resistor, the optical signal can be accurately measured.

In order to eliminate the problems associated with coupling instabilities, the power measured in each mode was normalized by the total power from both modes. A data acquisition board (DAQ) was used to sample the voltages from the two detectors at a rate of 1 kHz for 3 seconds per sample. For each sample, the two signals' difference was divided by their sum in order to obtain a set of normalized dV samples. These samples were then averaged to obtain a mean value for dV for each sampling period. In this manner, changes to the total power will have no affect on dV because the Faraday rotation measurement is only dependent on the normalized power difference of the TE and TM modes and not the total power.

Polarization rotation measurements were made using a 50 dB extinction ratio polarizer in order to determine the minimum power for which the detector could measure and accurate rotation. The polarizer was aligned with the input polarization, which was at 45° with respect to the horizontal. For each measurement, the polarizer was rotated 1.10° in the positive and negative directions. The input power was attenuated and the rotation was measured at each attenuation level using the technique discussed in Chapter 2. Figure 4-6 shows the error in the measured rotation, defined as the absolute value of the difference between the measured rotation and actual rotation, versus the total output power (TE+TM). As can be seen, the detector can measure Faraday rotations for power levels as low as 100 nW with 0.02 ° error.
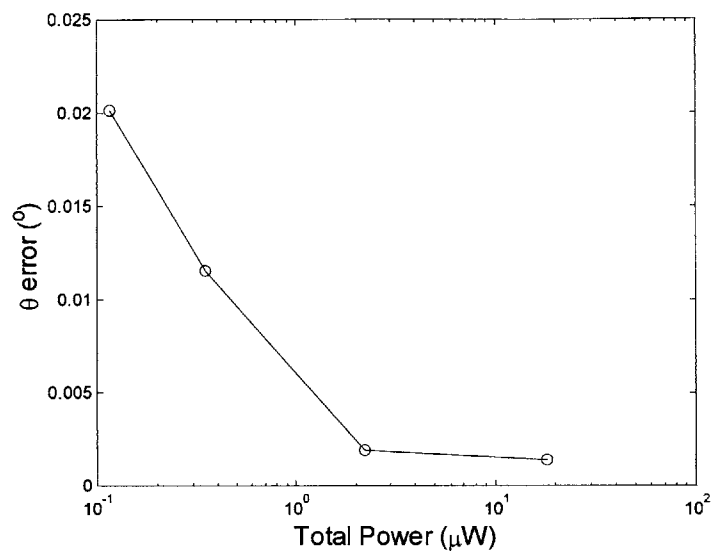
Figure 4-6: Error in measured polarization rotation vs total input power using balanced detector. The rotation angle is 1.10°

4.4 Experimental Results

4.4.1 Loss Measurement

The loss measurements were made for a Faraday rotator waveguide with length 1.1 mm and width 1.6 μm. Every 10 nm, a 1 nm wavelength scan was made to obtain the cavity spectrum. Figure 4-7 shows the cavity spectrum for the Faraday rotator waveguide at 1.55 μm.
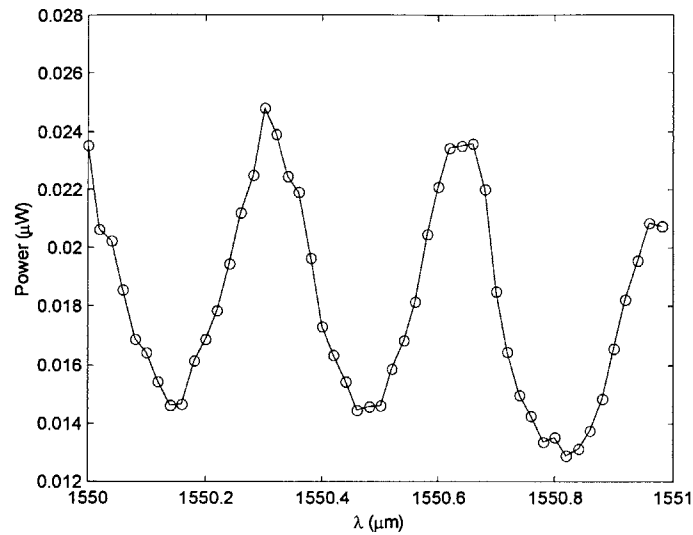
Figure 4-7: Cavity spectrum of Faraday rotator waveguide

The power on resonance and off resonance along with Equations 4.5, 4.6, and 4.16 were then used to calculate the loss. The error in the measured absorption coefficient α due to errors in the measured power can be expressed as

$$\left(\Delta\alpha\right)^2 = \left(\Delta P_{max}\right)^2 \left(\frac{\partial\alpha}{\partial P_{max}}\right)^2 + \left(\Delta P_{min}\right)^2 \left(\frac{\partial\alpha}{\partial P_{min}}\right)^2 \tag{4.29}$$

where

$$\frac{\partial\alpha}{\partial P_{max}} = \frac{-1}{l}\frac{\sqrt{\dfrac{P_{min}}{P_{max}}}}{P_{max} - P_{min}} \tag{4.30}$$

$$\frac{\partial\alpha}{\partial P_{min}} = \frac{-1}{l}\frac{\sqrt{\dfrac{P_{max}}{P_{min}}}}{P_{max} - P_{min}} \tag{4.31}$$

The error in the measured powers is 1 mV, and typical values for P_{max} and P_{min} are 20 and 10 mV, respectively. Using these values, the error in the absorption coefficient is 1.55 cm^{-1}.
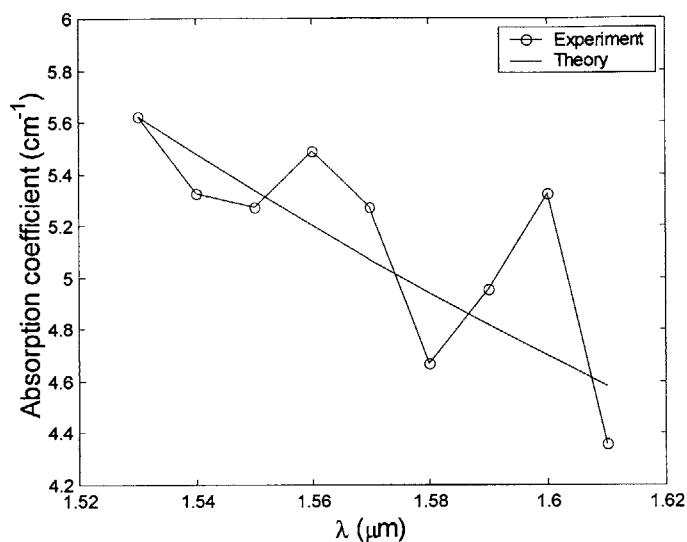
Figure 4-8: Absorption coefficient vs wavelength for 1.6 μm wide Faraday rotator waveguide

Figure 4-8 shows the measured loss for the waveguide. The increased losses at longer wavelengths may be due to scattering caused by sidewall roughness. If the walls are not smooth, then the light will be scattered and radiate out of the waveguide. Because the amplitude of the sidewall roughness is much smaller than the wavelength the scattering loss is expected to exhibit a λ^{-4} dependence [26]. The solid line in Figure 4-8 is λ^{-4} fit to the measured loss. As can be seen, the measured loss is close to the expected wavelength dependence, indicating that the dominant source for loss is sidewall roughness. Also, this sample had an accumulation of particles on its surface and sidewalls, which may have further increased the loss.

A previous measurement done on a 1.4 μm waveguide with cleaner surfaces using different photodetectors is shown in Figure 4-9.
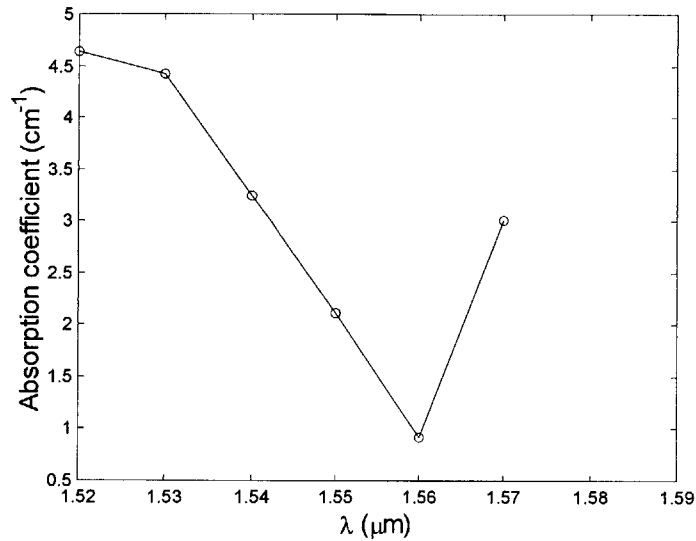
Figure 4-9: Absorption coefficient vs wavelength for 1.4 μm wide Faraday rotator waveguide with clean surfaces.

The loss is as low as 0.91 cm^{-1} and is larger at shorter and longer wavelengths because the input power is too low. This detector could not accurately measure the power minimum in the cavity spectrum at these wavelengths, making the measured loss too large.

4.4.2 Birefringence Measurement

The same waveguides used for the loss measurements were also used for the birefringence measurements. Once again, 1 nm wavelength scans were made at increments of 10 nm, but now the TE and TM light was separated with a polarizing beam splitter. The cavity spectrum for different center wavelengths is shown in Figure 4-10. As can be seen, the TE and TM peaks shift as the center wavelength changes and actually overlap at 1.54 μm, indicating that zero-birefringence has been achieved.
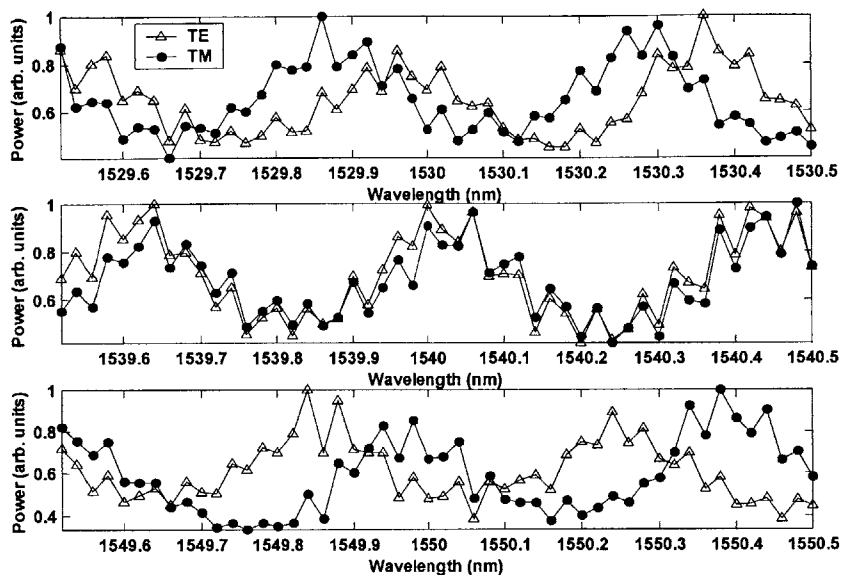
Figure 4-10: TE and TM cavity spectra for 1.4 μm waveguide centered at 1.53, 1.54, and 1.55 μm. The TE and TM peaks overlap at 1.54 μm, indicating that the birefringence is zero.
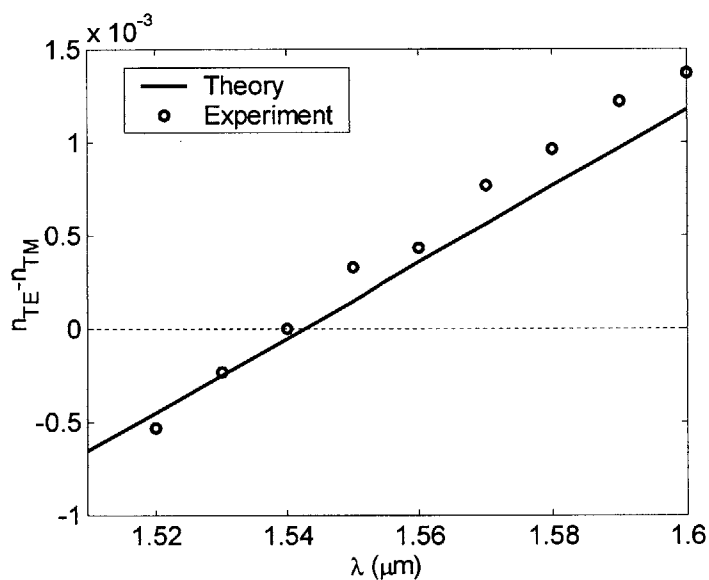
Figure 4-11: Experimental and theoretical birefringence vs wavelength for 1.4 μm wide Faraday rotator waveguide

Using Equation 4.13 and Equation 4.16, the birefringence was calculated for the center wavelength of each scan. The results are shown in Figure 4-11, along with the theoretical birefringence for a 1.4 μm waveguide. The measurements agree closely with

the theory. From the experimental data, it can be seen that the waveguide has zero-birefringence at 1.54 μm, which agrees with the theoretical zero-birefringence wavelength. The theoretical birefringence in Figure 4-10 was calculated using FIMMWave instead of the 2-D mode solver from Chapter 3. The 2-D mode solver predicts 1.55 μm for the zero-birefringence wavelength, while FIMMWave predicts 1.54 μm. This is the reason for the discrepancy between the zero-birefringence wavelength of Chapter 3 and this chapter.

4.4.3 Faraday Rotation Measurement

For Faraday rotation measurements, the setup for the birefringence measurements was used. In addition, a permanent magnet capable of providing fields of 0.2 T was mounted above the waveguides. The wavelength was scanned across the entire available spectrum (1.52 μm to 1.60 μm) in 1 nm steps and the TE and TM powers were measured. The measurement was done for both positive and negative magnetic fields.

The 1.4 μm waveguide facets were damaged after the birefringence measurements and could not be used for the Faraday rotation measurement. The next waveguide widths available were 1.6 μm and 1.8 μm. The waveguides are 1.1 mm long, the applied magnetic field is 0.18 T, and the Fe concentration in the InGaAsP cores is 8.0×10^{16} cm^{-3}.

To remove the rapid cavity oscillations, the measured Faraday rotation spectra for these waveguides were low pass filtered, as shown in Figure 4-12. Also shown in Figure 4-9 is the theoretical unfiltered and low-pass filtered Faraday rotation for the waveguides using the Verdet coefficient of -181.4 °/mm/T found in Table 2-1. The rotations show no large peak because the zero-birefringence wavelength is not within the measurement range.
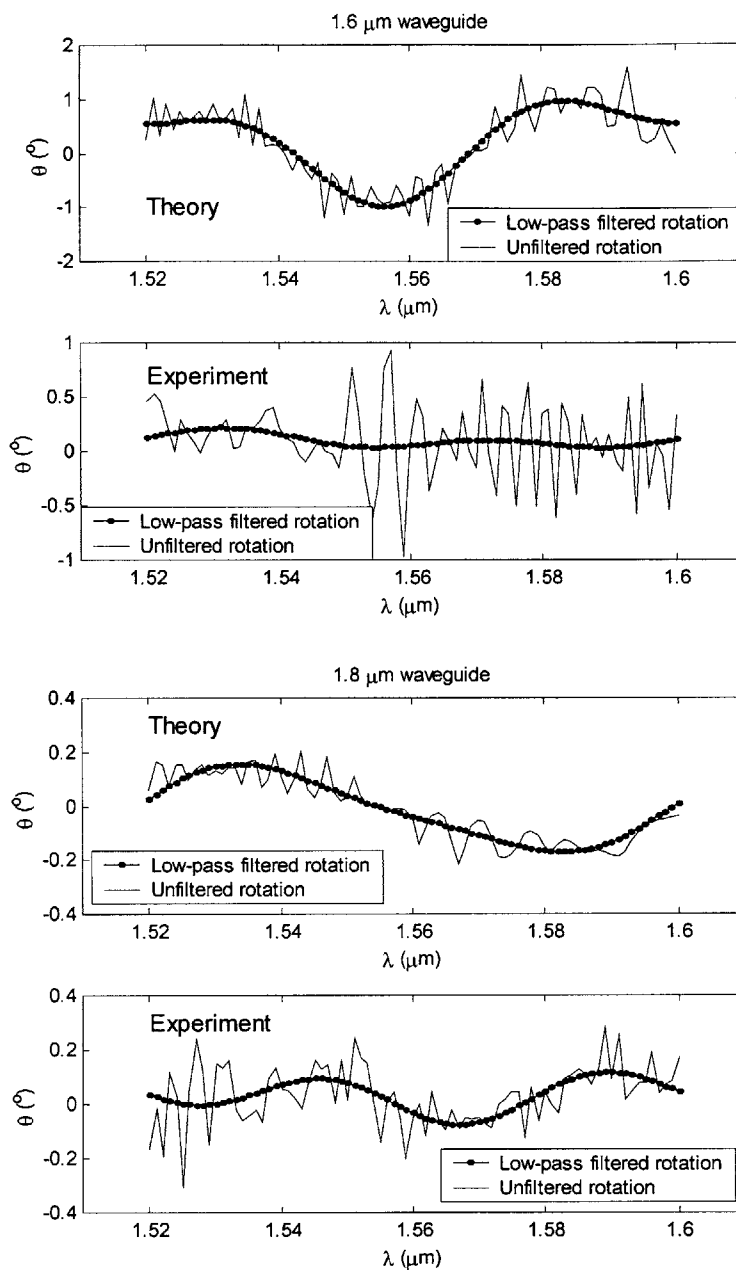
Figure 4-12: Measured and theoretical Faraday rotation of waveguides with width 1.6 μm (top) and 1.8 μm (bottom). The low-pass filtering removes the high frequency oscillations. The Fe concentration in the InGaAsP core is 8.0×10^{16} cm^{-3}, the waveguide length is 1.1 mm, and the applied magnetic field is 0.18 T. For the theoretical curve, the Verdet coefficient is assumed to be -181.4 °/mm/T.

In order to determine the Verdet coefficient of the waveguide, the low-pass filtered data was compared to simulations for different Verdet coefficients. This is shown in Figure 4-13. The maximum oscillation amplitude of the Faraday rotation is plotted

versus the waveguide width. Each line on the graph corresponds to a different Verdet coefficient, and the circles correspond to the measured oscillation amplitude.
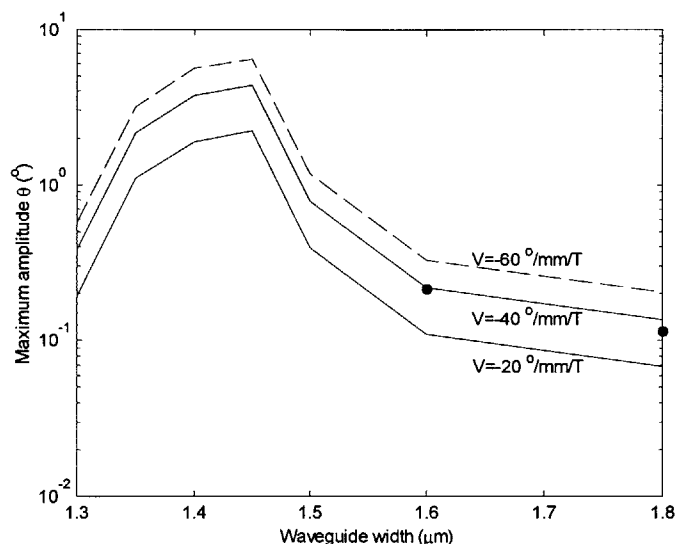
Figure 4-13: Maximum amplitude of Faraday rotation in wavelength range 1.52 μm to 1.60 μm vs. waveguide width for different Verdet coefficients. The waveguides are assumed to be 1.1 mm in length and the applied magnetic field is 0.18 T for the theoretical curves. The filled circles correspond to experimental data.

Based on the results shown in Figure 4-13, the absolute value of the Verdet coefficient for the waveguide is 40 °/mm/T, but the sign cannot be accurately determined. The Verdet coefficient for the bulk Fe:InGaAsP measured in Chapter 2 is -181.4 °/mm/T. The discrepancy may be due to errors in the Faraday rotation of the Fe:InP.

4.5 Summary

In this chapter, the experimental techniques for waveguide measurements were presented. Limitations of these techniques were also discussed. The experimental setup for the waveguide measurements was shown in detail. The important measurements made were waveguide loss, birefringence, and Faraday rotation.

The minimum measured waveguide loss was 0.91 cm^{-1}. The main source of the loss was sidewall roughness. By using the minimum measured loss, the waveguide

Verdet coefficient, and assuming a magnetic field of 1 T, the isolator figure of merit for this waveguide structure is

$$\frac{V}{\alpha} = \frac{40}{0.091} = 444 \qquad (4.32)$$

which is larger than the minimum required figure of merit of 195.

The birefringence was measured for the waveguide and was shown to agree closely with the theoretical birefringence. Therefore, the zero-birefringence waveguide needed for waveguide Faraday rotation has been achieved.

The zero-birefringence waveguides were damaged before Faraday rotation measurements could be made. Measurements made on waveguides with higher birefringence showed a suppressed rotation, with the suppression increasing for waveguides with higher birefringence.

Chapter 5
Conclusion

5.1 Summary

The goal of this thesis is to design and fabricate an optical isolator which can be monolithically integrated with semiconductor lasers used for telecommunications.

Chapter 2 studies the different contributions to Faraday rotation in semiconductors. Also in this chapter, the figure of merit for isolator materials, which is the ratio of the Verdet coefficient to optical loss, is established. It is found that free carrier Faraday rotation will not be suitable for an isolator because the free carrier loss is too high. For interband Faraday rotation, the strength of the rotation increases as the wavelength approaches the bandgap. By introducing magnetic dopants into a semiconductor, the Faraday rotation can be increased via an sp-d exchange interaction. Measurements show InGaAsP to have a Verdet coefficient of 98.7 °/mm/T and Fe:InGaAsP a Verdet coefficient as large as -181.4°/mm/T. The Verdet coefficient of Fe:InGaAsP can be made stronger by reducing the bandgap or increasing the Fe concentration. Based on these results, Fe:InGaAsP is selected as the material for the isolator because of its strong Faraday rotation and suitability for monolithic integration.

The design for the integrated isolator is presented in Chapter 3. The design consists of integrated Faraday rotators, half-wave plates, and multimode interferometers (MMI). The Faraday rotators were high-mesa etched structures whose widths were tuned to achieve zero birefringence. The half-wave plates had a notch placed on top of the waveguide core which coupled the TE and TM modes, creating new principal axes. By tuning the width of the notch, the angle of the principal axes could be controlled.

The maximum isolation is limited to 27 dB by the imbalance in the MMI. Simulations done on the isolator show it to have a maximum isolation of 24 dB at 1.55

µm. As the wavelength moves away from 1.55 µm, the isolation decreases. The factors which limit the bandwidth of the isolator are the birefringence in the Faraday rotators and the slow-axis angle of the half-wave plates. For Faraday rotators with a Verdet coefficient of 100°/mm, the isolator maintains a minimum isolation of 12 dB over 100 nm.

The waveguide Faraday rotator was fabricated using a reactive ion etch. Measurements were made on its loss, birefringence, and Faraday rotation. The loss had a minimum value of 0.91 cm^{-1}, and the birefringence was found to be zero at 1.54 µm. Because of damage to the waveguide facets, Faraday rotation measurements could not be made on the zero-birefringence waveguides. Measurements of high-birefringence waveguides showed suppressed Faraday rotation within the available wavelength range.

5.2 Future Work

5.2.1 Faraday Rotation Theory and Measurement

The interband Faraday rotation theory helped give intuition for how the bandgap affects the rotation strength. However, the theory was not very rigorous and did not agree with experimental results. First-order perturbation theory and k·p theory were used to calculate the energy splitting for the conduction and valence bands. To accurately calculate this splitting, a more complete theory is needed which finds the band structure under the influence of a magnetic field. The Faraday rotation is proportional to the difference in index of refraction for the right- and left-circular polarizations. In this thesis the index difference was calculated by Taylor expanding the index of refraction about the bandgap energy, and then using the difference in transition energy as the perturbation. Quantum mechanical expressions for the indices of refraction would give more accurate values for the Faraday rotation.

The theory presented for the magnetic dopant contribution to the Faraday rotation had two unknown parameters: the exchange integrals α and β for the conduction and valence bands. By knowing the exchange integrals for different semiconductor/magnetic dopant combinations, the Faraday rotation could be predicted more accurately. The

exchange integrals could be calculated if the Faraday rotation was measured in semiconductors with varying magnetic dopant concentrations.

It would be useful to measure Faraday rotation in different semiconductors. This would allow for further tests of the interband Faraday rotation theory. Faraday rotation measurements in InGaAsP samples of different compositions could be used determine what composition is ideal for a Faraday rotator.

5.2.2 Fabrication of Waveguide Components

The technique for fabricating the waveguide Faraday rotator has been demonstrated, however, the width has not been accurately controlled. The next steps are to fabricate the Faraday rotators with proper width, the MMI's, and the half-wave plates.

The masks used for the etching of the Faraday rotators can have smaller variations in width. For example, mask widths varying from 1.3 μm to 1.6 μm in 0.05 μm steps could be used. This way, it is more likely that the zero-birefringence width for the desired wavelength will be achieved.

The MMI's can be made using the same etch technique used to make the Faraday rotators. However, the half-wave plates are difficult because of the notch on top of the core. The notch requires a second etch aligned with the etch that defines the width of the half-wave plate. This can be accomplished using a dual mask etch process. Two masks are deposited on top of each other, the first is a nickel mask defining the width of the half-wave plate, and a second is a titanium mask defining the width of the notch. The etch is done for the first mask all the way to the substrate, and then the mask is removed. The etch done for the second mask only goes down to the waveguide core in order to define the notch on top of the half-wave plate.

5.2.3 Integration of Isolator with Laser

The isolator is designed to be monolithically integrated with a semiconductor laser. However, lasers are doped with free carriers to create gain, while the isolator was designed to be a passive structure. The challenge then, is to integrate a passive structure with an active structure. One way to do this is to use a design where the active structures are grown on top of passive structures, known as TWIN waveguides [27]. In these

structures, a lateral taper is used to squeeze the optical up from the passive layer to the active layer, or vice versa. This method can be used for the monolithic integration of the isolator with a semiconductor laser.

Appendix A

Jones' Matrices

This appendix aims to provide a better understanding for the Jones' matrix formalism used throughout this thesis. It begins with the derivation of a general Jones' matrix, and then goes on to calculate several common Jones' matrices.

A.1   Theory

The Jones' matrix formalism provides a systematic approach for analyzing complex optical systems where light propagates through polarizers, waveplates, and other optical elements. The first assumption for the Jones' matrix formalism is that the light propagates in the z direction, with the polarization being transverse to the propagation direction.
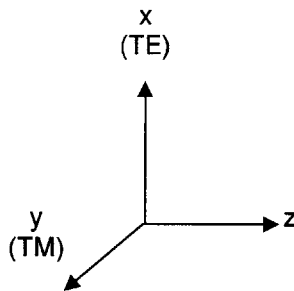
Figure A-1: Coordinate system for Jones' matrices in reference basis

The coordinate system defining the transverse electric (TE), transverse magnetic (TM), and propagation directions is shown in Figure A-1. This coordinate system will be

referred to as the reference basis. The polarization can be expressed as a two-component vector in this basis:

$$\overline{E} = \begin{bmatrix} x \\ y \end{bmatrix} \tag{A.1}$$

where x and y represent the TE and TM components of the polarization.

Optical media all possess eigenmode polarizations which have indices of refraction associated with them. These eigenmode polarizations are orthogonal and define the basis of the optical medium. The effect of the optical medium is to contribute a phase to each eigenmode polarization of the form

$$\phi_i = \frac{\omega}{c} n_i l \tag{A.2}$$

Here ω is the angular frequency of the light, l is the propagation length through the medium, c is the speed of light, and n_i is the index of refraction associated with eigenmode polarization i. This phase accumulation can be expressed with a diagonal matrix in the eigenmode polarization basis:

$$\overline{\overline{D}} = \begin{bmatrix} e^{-j\phi_1} & 0 \\ 0 & e^{-j\phi_2} \end{bmatrix} \tag{A.3}$$

By using a similarity transformation, this matrix can be expressed in the reference basis:

$$\overline{\overline{S}} = \overline{\overline{V}}\,\overline{\overline{D}}\,\overline{\overline{V}}^{-1} \tag{A.4}$$

S is the Jones' matrix of the optical medium in the reference basis and V is the matrix whose columns are the eigenmode polarization vectors v_1 and v_2. By knowing the eigenmode polarizations and corresponding phases, the Jones' matrix for any optical medium can be found.

A.2 Examples

A.2.1 Polarizer

A polarizer can be described with a Jones matrix where one eigenmode polarization is not transmitted at all (extinction axis), and one is transmitted without attenuation (transmission axis). The Jones matrix for a polarizer with transmission axis oriented at an angle θ with respect to the TE axis is

$$Pol(\theta) = \begin{bmatrix} \cos(\theta) & -\sin(\theta) \\ \sin(\theta) & \cos(\theta) \end{bmatrix} \begin{bmatrix} 1 & 0 \\ 0 & 0 \end{bmatrix} \begin{bmatrix} \cos(\theta) & -\sin(\theta) \\ \sin(\theta) & \cos(\theta) \end{bmatrix}^{-1} =$$
$$\begin{bmatrix} \cos^2(\theta) & \cos(\theta)\sin(\theta) \\ \cos(\theta)\sin(\theta) & \sin^2(\theta) \end{bmatrix}$$

(A.5)

A.2.2 Half-Wave Plate

A half-wave plate is a birefringent optical element with linear eigenmode polarizations. The polarizations are labeled as slow and fast axes: the slow axis corresponds to the polarization with the larger index of refraction, and therefore slower phase velocity. The key feature of a half-wave plate is that the phase difference between the slow and fast axes is π. By neglecting common phase factors, the Jones' matrix for a half-wave plate with its slow-axis oriented at an angle θ with respect to the TE axis is

$$HWP(\theta) = \begin{bmatrix} \cos(\theta) & -\sin(\theta) \\ \sin(\theta) & \cos(\theta) \end{bmatrix} \begin{bmatrix} 1 & 0 \\ 0 & e^{-j\pi} \end{bmatrix} \begin{bmatrix} \cos(\theta) & -\sin(\theta) \\ \sin(\theta) & \cos(\theta) \end{bmatrix}^{-1} =$$
$$\begin{bmatrix} \cos(2\theta) & \sin(2\theta) \\ \sin(2\theta) & -\cos(2\theta) \end{bmatrix}$$

(A.6)

A.2.3 Faraday Rotator

The eigenmode polarizations for a Faraday rotator of length l are right- and left-handed circular polarizations whose phase difference is 2Vl. Here V is the Verdet coefficient of the Faraday rotator. The Jones' vectors $v_{\pm}$ for the circular polarizations are

$$\overline{v_{\pm}} = \frac{1}{\sqrt{2}} \begin{bmatrix} 1 \\ \mu j \end{bmatrix}$$

(A.7)

By neglecting common phase factors, the Jones' matrix for the Faraday rotator then becomes

$$FR = \frac{1}{\sqrt{2}}\begin{bmatrix} 1 & 1 \\ -j & j \end{bmatrix}\begin{bmatrix} 1 & 0 \\ 0 & e^{-j2Vl} \end{bmatrix}\left(\frac{1}{\sqrt{2}}\begin{bmatrix} 1 & 1 \\ -j & j \end{bmatrix}\right)^{-1} = \begin{bmatrix} \cos(Vl) & -\sin(Vl) \\ \sin(Vl) & \cos(Vl) \end{bmatrix} \qquad (A.8)$$

As can be seen, the effect of a Faraday rotator is to rotate a polarization vector by an angle Vl.

Appendix B

Eigenmode Propagation

Code

This appendix aims to describe in detail the eigenmode propagation code used for the isolator simulation in Chapter 3. The MATLAB code for this eigenmode propagator is found at the end of this appendix.

B.1 General Description of Eigenmode Propagation Code

The code begins with an input mode incident on a waveguide structure, and then calculates the mode excitation coefficients using the two dimensional mode profiles of each structure:

$$c_m(0) = \frac{\int \overline{\psi^*(0) \cdot \phi_m} \, dA}{\int \overline{\phi_m^* \cdot \phi_m} \, dA} \tag{B.1}$$

ϕ_m is the electric field amplitude of the two-dimensional mode profile of the waveguide, $\psi(0)$ is the input mode profile, c_m is the mode excitation coefficient, m is the mode index, and the integral is done over the two-dimensional cross-section of the waveguide.

Because each mode order consisted of two orthogonal polarizations, Jones' matrices could be used to propagate these modes. The mode excitation coefficients are

defined as $c_m^i(0)$, where the subscript corresponds to the mode order, and the superscript corresponds to the polarization. After propagating a distance L, the excitation coefficients become

$$\begin{bmatrix} c_m^x(L) \\ c_m^y(L) \end{bmatrix} = \overline{\overline{S(L)}} \begin{bmatrix} c_m^x(0) \\ c_m^y(0) \end{bmatrix} \tag{B.2}$$

where S(L) is the Jones' matrix for the corresponding waveguide structure. The resulting mode after propagating distance L is then:

$$E^i(L) = \sum_m c_m^i(L) E_m^i \tag{B.3}$$

where E^i represents the ith polarization component of the mode. With this technique it is simple to incorporate non-reciprocal elements such as the Faraday rotator by using the Jones matrix formalism described in Appendix A.

To verify that the code worked properly, it was compared to commercial eigenmode propagation software (Fimmprop). The test structure was an MMI. Both Fimmprop and the eigenmode propagator were used to calculate the output power in one arm of an MMI as a function of the MMI length. The results are shown in Figure B-1. As can be seen, the eigenmode propagator code agrees closely with the commercial software.
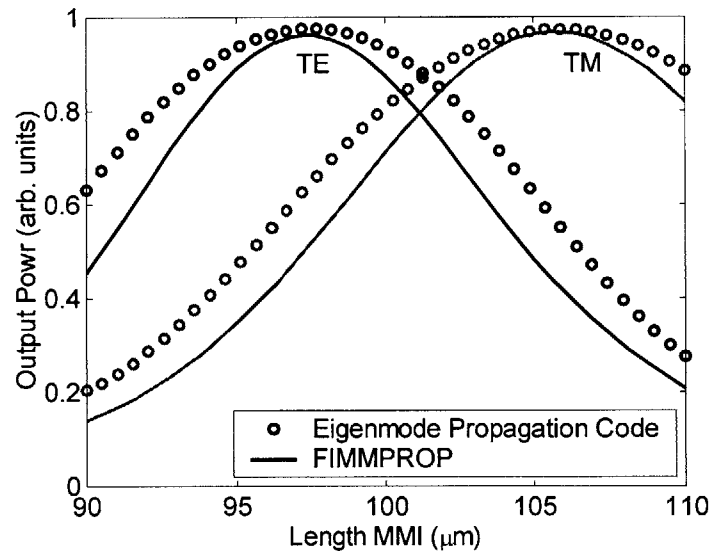
Figure B-1: Simulation of MMI done using Fimmprop and eigenmode propagation code written for this thesis

The 2-D mode profiles for each waveguide structure were calculated with a fully vectorial mode solver. These mode profiles were then loaded into MATLAB variables using the code fileopen.m. To simulate the isolator, five junctions were defined, as shown in Figure B-2. A script was written to calculate the propagate field at each junction. The functions jones and rot were used by these scripts to calculate the Jones' matrices for the different waveguide components.
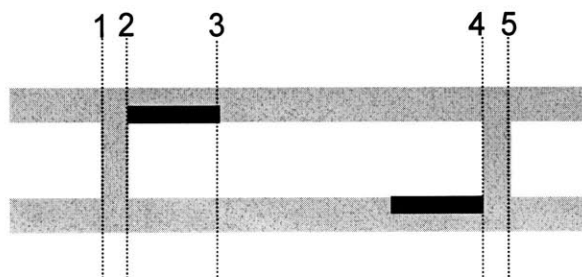
Figure B-2: Definition of junctions used in isolator simulation

B.2 MATLAB Code

bandwidth_sim.m

```
%Bandwidth simulation of isolator
w=[];          %wavelength array [um]
verdet=[.1]*ones(1,11);      %verdet coefficient array [deg/um]
l_hwp=157.5;                 %length of half-wave plate [um]
l_fr=45/.1;                  %length of Faraday rotator [um]
lmmi=52;                     %lenght of MMI [um]
input_pol=45*pi/180; %input polarization in rad
p_lp=[];    %positive verdet output power in left guide
p_rp=[];    %positive verdet output power in right guide
p_ln=[];    %negative verdet output power in left guide
p_rn=[];    %negative verdet output power in right guide

for j=1:11
   lambda=1.500+.01*(j-1);     %wavelength [um]
   w(j)=lambda;                %update wavelength array
   V=verdet(j);               %Verdet coefficient [deg/um]
   V1=0;                      %verdet for MMI and HWP
   wavelength=lambda*1e3
   cd (num2str(eval('wavelength')));  %change directory for each wavelength
```

```
    fileopen                    %load 2-D mode profiles into MATLAB variables
    isolator_sim                %run simulation with positive Verdet coefficient
    p_lp(j)=power_l;            %update left power array
    p_rp(j)=power_r;            %update right power array
    V=-verdet(j);              %negative Verdet coefficient
    isolator_sim                %run simulation with negative Verdet coefficient
     p_ln(j)=power_l;           %update left power array
    p_rn(j)=power_r;           %update right power array
end

isolation=10*log10(p_lp);      %isolation [dB]
insertion_loss=10*log10(p_ln);   %insertion loss [dB]
```

fileopen.m

```
%fileopen
%loads all 2-D mode profiles and mode effective indices into MATLAB varibales
%for isolator simulation

%%%%%%%%first Faraday rotator (FR)
cd fr_1
fid=fopen('Neff');
a=fscanf(fid,'%g',[1 inf]);
fclose(fid);
fr_1_n=a';

fid=fopen('ex0.dat');
a=fscanf(fid,'%g',[1 inf]);
fclose(fid);
fr_1_0_x=abs(a)';

fid=fopen('ey0.dat');
a=fscanf(fid,'%g',[1 inf]);
fclose(fid);
fr_1_0_y=abs(a)';

fid=fopen('ex1.dat');
a=fscanf(fid,'%g',[1 inf]);
fclose(fid);
fr_1_1_x=abs(a)';

fid=fopen('ey1.dat');
a=fscanf(fid,'%g',[1 inf]);
fclose(fid);
```

```
fr_1_1_y=abs(a)';

%%%%%%%%%%%%%%%second FR
cd ..
cd fr_r

fid=fopen('Neff');
a=fscanf(fid,'%g',[1 inf]);
fclose(fid);
fr_r_n=abs(a)';

fid=fopen('ex0.dat');
a=fscanf(fid,'%g',[1 inf]);
fclose(fid);
fr_r_0_x=abs(a)';

fid=fopen('ey0.dat');
a=fscanf(fid,'%g',[1 inf]);
fclose(fid);
fr_r_0_y=abs(a)';

fid=fopen('ex1.dat');
a=fscanf(fid,'%g',[1 inf]);
fclose(fid);
fr_r_1_x=abs(a)';

fid=fopen('ey1.dat');
a=fscanf(fid,'%g',[1 inf]);
fclose(fid);
fr_r_1_y=abs(a)';

%%%%%%%%%%%%%first half-wave plate (HWP)
cd ..
cd hwp_p

fid=fopen('Neff');
a=fscanf(fid,'%g',[1 inf]);
fclose(fid);
hwp_p_n=a';

fid=fopen('ex0.dat');
a=fscanf(fid,'%g',[1 inf]);
fclose(fid);
hwp_p_0_x=abs(a)';

fid=fopen('ey0.dat');
a=fscanf(fid,'%g',[1 inf]);
fclose(fid);
```

```
hwp_p_0_y=abs(a)';

fid=fopen('ex1.dat');
a=fscanf(fid,'%g',[1 inf]);
fclose(fid);
hwp_p_1_x=-abs(a)';

fid=fopen('ey1.dat');
a=fscanf(fid,'%g',[1 inf]);
fclose(fid);
hwp_p_1_y=abs(a)';

%%%%%%%%%%%%%second HWP
cd ..
cd hwp_n

fid=fopen('Neff');
a=fscanf(fid,'%g',[1 inf]);
fclose(fid);
hwp_n_n=a';

fid=fopen('ex0.dat');
a=fscanf(fid,'%g',[1 inf]);
fclose(fid);
hwp_n_0_x=abs(a)';

fid=fopen('ey0.dat');
a=fscanf(fid,'%g',[1 inf]);
fclose(fid);
hwp_n_0_y=-abs(a)';

fid=fopen('ex1.dat');
a=fscanf(fid,'%g',[1 inf]);
fclose(fid);
hwp_n_1_x=abs(a)';

fid=fopen('ey1.dat');
a=fscanf(fid,'%g',[1 inf]);
fclose(fid);
hwp_n_1_y=abs(a)';

%%%%%%%%%%%%Multimode interferometer (MMI)
cd ..
cd mmi

fid=fopen('Neff');
a=fscanf(fid,'%g',[1 inf]);
fclose(fid);
```

```
mmi_n=a';

fid=fopen('ex0.dat');
a=fscanf(fid,'%g',[1 inf]);
fclose(fid);
mmi_0_x=a';

fid=fopen('ey0.dat');
a=fscanf(fid,'%g',[1 inf]);
fclose(fid);
mmi_0_y=a';

fid=fopen('ex1.dat');
a=fscanf(fid,'%g',[1 inf]);
fclose(fid);
mmi_1_x=a';

fid=fopen('ey1.dat');
a=fscanf(fid,'%g',[1 inf]);
fclose(fid);
mmi_1_y=a';

fid=fopen('ex2.dat');
a=fscanf(fid,'%g',[1 inf]);
fclose(fid);
mmi_2_x=a';

fid=fopen('ey2.dat');
a=fscanf(fid,'%g',[1 inf]);
fclose(fid);
mmi_2_y=a';

fid=fopen('ex3.dat');
a=fscanf(fid,'%g',[1 inf]);
fclose(fid);
mmi_3_x=a';

fid=fopen('ey3.dat');
a=fscanf(fid,'%g',[1 inf]);
fclose(fid);
mmi_3_y=a';

fid=fopen('ex4.dat');
a=fscanf(fid,'%g',[1 inf]);
fclose(fid);
mmi_4_x=a';

fid=fopen('ey4.dat');
```

```
a=fscanf(fid,'%g',[1 inf]);
fclose(fid);
mmi_4_y=a';

fid=fopen('ex5.dat');
a=fscanf(fid,'%g',[1 inf]);
fclose(fid);
mmi_5_x=a';

fid=fopen('ey5.dat');
a=fscanf(fid,'%g',[1 inf]);
fclose(fid);
mmi_5_y=a';

fid=fopen('ex6.dat');
a=fscanf(fid,'%g',[1 inf]);
fclose(fid);
mmi_6_x=a';

fid=fopen('ey6.dat');
a=fscanf(fid,'%g',[1 inf]);
fclose(fid);
mmi_6_y=a';

fid=fopen('ex7.dat');
a=fscanf(fid,'%g',[1 inf]);
fclose(fid);
mmi_7_x=a';

fid=fopen('ey7.dat');
a=fscanf(fid,'%g',[1 inf]);
fclose(fid);
mmi_7_y=a';

cd ..
```

isolator_1_2.m

```
%Isolator simulation
%Propagate field from stage 1 to stage 2
%stage 1=input of first MMI
%stage 2=output of first MMI
k=2*pi/lambda;%wavevector

x_xpol=[-2.5:5/502:2.5]'; %define x coordinates for x polarization
y_xpol=[-2.5:5/501:2.5]'; %define y coordinates for x polarization
```

```matlab
[X_xpol,Y_xpol]=meshgrid(y_xpol,x_xpol); %create    coordinate    mesh    for    x
polarization
x_ypol=[-2.5:5/501:2.5]'; %define x coordinates for y polarization
y_ypol=[-2.5:5/502:2.5]'; %define y coordinates for y polarization
[X_ypol,Y_ypol]=meshgrid(y_ypol,x_ypol);%create coordinate mesh for y polarization

neffx=[mmi_n(2);mmi_n(4);mmi_n(6);mmi_n(7)];%effective index of x modes in MMI
neffy=[mmi_n(1);mmi_n(3);mmi_n(5);mmi_n(8)];%effective index of y modes in MMI
ax=cos(input_pol);%percent of input power in x direction
ay=sin(input_pol);%percent of input power in y direction


%coupling coefficients of x modes
cx0=(sum(fr_1_0_x.*mmi_1_x)+sum(fr_1_1_x.*mmi_1_x));
cx1=(sum(fr_1_0_x.*mmi_3_x)+sum(fr_1_1_x.*mmi_3_x));
cx2=(sum(fr_1_0_x.*mmi_5_x)+sum(fr_1_1_x.*mmi_5_x));
cx3=(sum(fr_1_0_x.*mmi_6_x)+sum(fr_1_1_x.*mmi_6_x));

%coupling coefficients of y modes
cy0=(sum(fr_1_0_y.*mmi_0_y)+sum(fr_1_1_y.*mmi_0_y));
cy1=(sum(fr_1_0_y.*mmi_2_y)+sum(fr_1_1_y.*mmi_2_y));
cy2=(sum(fr_1_0_y.*mmi_4_y)+sum(fr_1_1_y.*mmi_4_y));
cy3=(sum(fr_1_0_y.*mmi_7_y)+sum(fr_1_1_y.*mmi_7_y));

%imaged x field at stage 1
cx=[cx0; cx1; cx2; cx3];
cx=ax*cx/sqrt(sum(cx.^2));
ex=[mmi_1_x mmi_3_x mmi_5_x mmi_6_x];
field1x=ex*cx;

%imaged y field at stage 1
cy=[cy0; cy1; cy2; cy3];
cy=ay*cy/sqrt(sum(cy.^2));
ey=[mmi_0_y mmi_2_y mmi_4_y mmi_7_y];
field1y=ey*cy;


%propagation constant of each mode in MMI
beta_x_mmi=neffx*2*pi/lambda;
beta_y_mmi=neffy*2*pi/lambda;

%Jones matrix of each mode pair in MMI
phasemmi0=jones(beta_x_mmi(1),beta_y_mmi(1),V1,0,lmmi);
phasemmi1=jones(beta_x_mmi(2),beta_y_mmi(2),V1,0,lmmi);
phasemmi2=jones(beta_x_mmi(3),beta_y_mmi(3),V1,0,lmmi);
phasemmi3=jones(beta_x_mmi(4),beta_y_mmi(4),V1,0,lmmi);

%Phase and coupling coefficient for each mode pair
```

```
cl0=phasemmi0*[cx(1);cy(1)];
cl1=phasemmi1*[cx(2);cy(2)];
cl2=phasemmi2*[cx(3);cy(3)];
cl3=phasemmi3*[cx(4);cy(4)];


%x field at stage 2
clx=[cl0(1); cl1(1); cl2(1); cl3(1)];
field2x=ex*clx;
%y field at stage 2
cly=[cl0(2); cl1(2); cl2(2); cl3(2)];
field2y=ey*cly;
```

isolator_2_3.m

```
%Isolator simulation
%Propagate field from stage 2 to stage 3
%stage 2=output of first MMI
%stage 3=output of first half-wave plate (HWP) and Faraday rotator (FR)


%%%%%%%%%%%%%%%%%%%%%%%parameters for first FR%%%%%%%%%%%%%%%


%propagation constants for FR
beta_0_fr1=2*pi/lambda*fr_1_n(1);
beta_1_fr1=2*pi/lambda*fr_1_n(jj);


%coupling coefficients for first FR
c_fr1_0=sum(field2x.*fr_1_0_x)+sum(field2y.*fr_1_0_y);
c_fr1_1=sum(field2x.*fr_1_1_x)+sum(field2y.*fr_1_1_y);
c_fr1=[c_fr1_0;c_fr1_1]; %x-y-z basis

%Jones matrix for first FR
phasefr1=jones(beta_0_fr1,beta_1_fr1,V,0,l_fr);
c_fr1L=phasefr1*c_fr1;%x-y-z basis

%propagated field in first FR
field_fr1_x=c_fr1L(1)*fr_1_0_x+c_fr1L(2)*fr_1_1_x;
field_fr1_y=c_fr1L(1)*fr_1_0_y+c_fr1L(2)*fr_1_1_y;
```

```
%%%%%%%%%%%%%%%%%%%%%%parameters for first HWP%%%%%%%%%%%%%%%%%%%%%%

%%%%propagation constants for first HWP
beta_s_hwpn=2*pi/lambda*hwp_n_n(1);
beta_f_hwpn=2*pi/lambda*hwp_n_n(2);

%coupling coefficients for first HWP
c_hwpn_s=sum(field2x.*hwp_n_0_x)+sum(field2y.*hwp_n_0_y);    %slow axis mode
c_hwpn_f=sum(field2x.*hwp_n_1_x)+sum(field2y.*hwp_n_1_y);    %fast axis mode
c_hwpn=[c_hwpn_s;c_hwpn_f];%slow-fast-z basis

%Jones matrix for first HWP
phasehwpn=jones(beta_s_hwpn,beta_f_hwpn,V1,0,l_hwp);
c_hwpnL=phasehwpn*c_hwpn; %slow-fast-z basis


%propagated x field in first HWP
field_hwpn_x=c_hwpnL(1)*hwp_n_0_x+c_hwpnL(2)*hwp_n_1_x;
%propagated y field in first HWP
field_hwpn_y=c_hwpnL(1)*hwp_n_0_y+c_hwpnL(2)*hwp_n_1_y;

%%%%%%%%%%%%%%%%%%%%%%%%%%%%%%%%%%%%%%%%%%%%%%%%%
%x field at stage 3
field3x=field_frl_x+field_hwpn_x;
%y field at stage 3
field3y=field_frl_y+field_hwpn_y;
```

isolator_3_4.m

```
%Isolator simulation
%Propagate field from stage 3 to stage 4
%stage 3=output of first half-wave plate (HWP) and Faraday rotator (FR)
%stage 4=output of second half-wave plate (HWP) and Faraday rotator (FR)

%%%%%%%%%%%%%%%%%%%%%%%%parameters for second FR%%%%%%%%%%%%%%%%%%

%coupling coefficients for second FR
c_frr_0=sum(field3x.*fr_r_0_x)+sum(field3y.*fr_r_0_y);
c_frr_1=sum(field3x.*fr_r_1_x)+sum(field3y.*fr_r_1_y);
c_frr=[c_frr_0;c_frr_1]; %x-y-z basis

%Jones matrix for second FR
phasefrr=phasefrl;
c_frrL=phasefrr*c_frr;%x-y-z basis

%propagated field in second FR

%%%%%%%%%%%%%%%%%%%%%%%%%%parameters for first HWP%%%%%%%%%%%%%%%%%%
```

```
field_frr_x=c_frrL(1)*fr_r_0_x+c_frrL(2)*fr_r_1_x;
field_frr_y=c_frrL(1)*fr_r_0_y+c_frrL(2)*fr_r_1_y;


%%%%%%%%%%%%%%%%%%%%%parameters for second HWP%%%%%%%%%%%%%%%%%%%%%

%propagation constants for second HWP
beta_f_hwpp=beta_f_hwpn;
beta_s_hwpp=beta_s_hwpn;

%coupling coefficients for second HWP
c_hwpp_s=sum(field3x.*hwp_p_0_x)+sum(field3y.*hwp_p_0_y);
c_hwpp_f=sum(field3x.*hwp_p_1_x)+sum(field3y.*hwp_p_1_y);
c_hwpp=[c_hwpp_s;c_hwpp_f];%slow-fast-z basis

%Jones matrix for second HWP
phasehwpp=jones(beta_s_hwpn,beta_f_hwpn,V1,0,l_hwp);
c_hwppL=phasehwpp*c_hwpp; %slow-fast-z basis

%propagated field in second HWP
field_hwpp_x=c_hwppL(1)*hwp_p_0_x+c_hwppL(2)*hwp_p_1_x;
field_hwpp_y=c_hwppL(1)*hwp_p_0_y+c_hwppL(2)*hwp_p_1_y;


%%%%%%%%%%%%%%%%%%%%%%%%%%%%%%%%%%%%%%%%%%%%%%%%%%%%%%%%%%%%%%%%%%

%x field at stage 4
field4x=field_frr_x+field_hwpp_x;
%y field at stage 4
field4y=field_frr_y+field_hwpp_y;
```

isolator_4_5.m

```
%Isolator simulation
%Propagate field from stage 4 to stage 5
%stage 4=output of second half-wave plate (HWP) and Faraday rotator (FR)
%stage 5= output of second MMI

%coupling coefficients for x modes
cx1o=(sum(field4x.*mmi_1_x));
cx2o=(sum(field4x.*mmi_3_x));
cx3o=(sum(field4x.*mmi_5_x));
cx4o=(sum(field4x.*mmi_6_x));

cxo=[cx1o; cx2o; cx3o; cx4o;];
ex=[mmi_1_x mmi_3_x mmi_5_x mmi_6_x];

%coupling coefficients for y modes
```

```
cy1o=sum(sum(field4y.*mmi_0_y));
cy2o=sum(sum(field4y.*mmi_2_y));
cy3o=sum(sum(field4y.*mmi_4_y));
cy4o=sum(sum(field4y.*mmi_7_y));

%imaged y field at stage 4
cyo=[cy1o; cy2o; cy3o; cy4o;];
ey=[mmi_0_y mmi_2_y mmi_4_y mmi_7_y];

%Phase and coupling coefficient for each mode pair
cl1o=phasemmi0*[cx1o;cy1o];
cl2o=phasemmi1*[cx2o;cy2o];
cl3o=phasemmi2*[cx3o;cy3o];
cl4o=phasemmi3*[cx4o;cy4o];

%x field at stage 5
clxo=[cl1o(1); cl2o(1); cl3o(1); cl4o(1)];
field5x=ex*clxo;
%y field at stage 5
clyo=[cl1o(2); cl2o(2); cl3o(2); cl4o(2)];
field5y=ey*clyo;


%reshape fields for power calculations
f5y=reshape(field5y,503,502)';
f5x=reshape(field5x,502,503)';

%field in left guide
f5xl=f5x(yl_xpol,xl_xpol);
%field in right guide
f5xr=f5x(yr_xpol,xr_xpol);

%x power in right guide
powerf5xr=sum(sum(abs(f5xr).^2));
%x power in left guide
powerf5xl=sum(sum(abs(f5xl).^2));


%y field in right guide
f5yr=f5y(yr_ypol,xr_ypol);
%y field in left guide
f5yl=f5y(yl_ypol,xl_ypol);

%y power in right guide
powerf5yr=sum(sum(abs(f5yr).^2));
%y power in left guide
powerf5yl=sum(sum(abs(f5yl).^2));
```

```
%power in left guide
power_l=powerf5xl+powerf5yl
%power in right guide
power_r=powerf5xr+powerf5yr
```

jones.m

```
%function J=jones(beta_1,beta_2,V,theta,l)
%calculates Jones matrix for waveguide structure

%V=verdet coefficient in degrees/length
%beta_1 and beta_2 are propagation constants of 2 modes in rad/length
%theta=angle of principle axes in degrees
%l=device length in length
%J=Jones matrix of birefringent, magnetically active material
function J=jones(beta_1,beta_2,V,theta,l)
Vr=V*pi/180; %convert verdet into rad/length
delta=(beta_2-beta_1)/2;   %delta=(beta1=2-beta1)/2 in radians/length
alpha=sqrt((Vr)^2+delta^2);

R=rot(theta);

a=cos(alpha*l)-i*delta/alpha*sin(alpha*l);
b=-Vr/alpha*sin(alpha*l);
c=-b;
d=cos(alpha*l)+i*delta/alpha*sin(alpha*l);

D=[a b;c d];
J=R*D*inv(R)*exp(i*(beta_1+beta_2)*l/2);
```

rot.m

```
%a=function rot(theta)
%calculates rotation matrix for angle theta
%theta in degrees
function a=rot(theta)
theta1=theta*pi/180;
a=[cos(theta1) -sin(theta1);sin(theta1) cos(theta1)];
```

Bibliography

[1]   O. Hirota and Y. Suematsu, "Noise properties of injection lasers due to reflected waves," *IEEE J. Quantum Electron.*, vol QE-15, no. 3, pp. 142-149, 1979.

[2]   Image drawn by Gale Petrich, Research Scientist in the Research Laboratory for Electronics at the Massachusetts Institute of Technology

[3]   S. Yamamoto and T. Makimoto, "Circuit-theory for a class of anisotropic and gyrotropic thin-film optical waveguides and design of nonreciprocal devices for integrated optics," *J. Appl. Phys.*, vol. 45, no. 2, pp. 882-888, 1974.

[4]   J. Fujita, M. Levy, R. M. Osgood, Jr., L. Wilkens, and H. Dötsch, "Polarization-independent waveguide optical isolator based on nonreciprocal phase shift," *IEEE Photon. Tech. Lett.*, vol. 12, no. 11, pp. 1510-1512, 2000.

[5]   J. Fujita, M. Levy, R. M. Osgood, Jr., L. Wilkens, and H. Dötsch, "Waveguide optical isolator based on Mach-Zehnder interferometer," *Appl. Phys Lett.*, vol. 76, no. 16, pp. 2158-2160, 2000.

[6]   H. Shimizu and M. Tanaka, "Design of semiconductor-waveguide-type optical isolators using the nonreciprocal loss/gain in the magneto-optical waveguides having MnAs nanoclusters," *Appl. Phys. Lett.*, vol. 81, no. 27, pp. 5246-5248, 2002.

[7]   W. Van Parys, M. Vanwolleghem, D. Van Thourhout, R. Baets, J. Decobert, B. Dagens, B. Thedrez, R. Wirix-Speetjens, and L. Lagae, "InP-based monolithically integrated optical waveguide isolator with 32 dB/cm isolation," *Proc. of Conf. of Lasers and Electro-Optics*, pp. 386-387, 2004.

[8]   W. Zaets and K. Ando, "Optical waveguide isolator based on nonreciprocal loss/gain of amplifier covered by ferromagnetic layer," *IEEE Photon. Tech. Lett.*, vol. 11, no. 8, pp. 1012-1014, 1999.

[9]   R. Wolfe, J. Hegarty, J. F. Dillon, Jr., L. C. Luther, G. K. Celler, L. E. Trimble, and C. S. Dorsey, "Thin-film waveguide magneto-optic isolator," *Apply. Phys. Lett.*, vol. 46, no. 9, pp. 817-819, 1985.

[10]   N. Sugimoto, H. Terui, A. Tate, Y. Katoh, Y. Yamada, A. Sugita, A. Shibukawa, and Y. Inoue, "A hybrid integrated waveguide isolator on a silica-based planar lightwave circuit," *J. Lightwave Tech.*, vol. 14, no. 11, pp. 2537-2546, 1996.

[11]   N. Sugimoto, T. Shintaku, A. Tate, H. Terui, M. Shimokozono, E. Kubota, M. Ishii, and Y. Inoue, "Waveguide polarization-independent optical circulator," *IEEE Photon. Tech. Lett.*, vol. 11, no. 3, pp. 355-357, 1999.

[12]   M. Cardona, "Electron effective masses of InAs and GaAs as a function of temperature and doping," *Phys. Rev.*, vol. 121, no. 3, pp. 752-758, 1961.

[13]   A. K. Walton and T. S. Moss, "The infra-red Faraday effect in Germanium," *Proc. Phys. Soc.*, vol. 78, no. 6, pp. 1393-1406, 1961.

[14]   A. K. Walton and U. K. Mishra, "The infra-red Faraday effect in p-type semiconductors," *Proc. Phys. Soc.*, vol. 90, pp. 1111-1126, 1967.

[15]   B. Broberg and S. Lindgren, "Refractive index of $In_{1-x}Ga_xAs_yP_{1-y}$ layers and InP in the transparent wavelength region," *J. Appl. Phys.*, vol. 55, no. 9, pp. 3376-3381, 1984.

[16]   L. Roth, B. Lax, and S. Zwerdling, "Theory of optical magneto-absorption effects in semiconductors," *Phys. Rev.*, vol. 114, no. 1, pp. 90-104, 1961.

[17]   G. Bastard, C. Rigaux, and A. Mycielski, "Giant splitting induced by exchange interactions in $Hg_{1-k}Mn_kTe$ Mixed Crystal," *Phys. Stat. Sol. (B)*, vol. 79, pp. 585-593, 1977.

[18]   J. A. Gaj, J. Ginter, and R. R. Galazka, "Exchange interaction of Manganese $3d^5$ states with band electrons in $Cd_{1-x}Mn_xTe$," *Phys. Stat. Sol. (B)*, vol. 85, pp. 655-662, 1978.

[19]   D. U. Bartholomew, J. K. Furdyna, and A. K. Ramdas, "Interband Faraday rotation in diluted magnetic semiconductors: $Zn_{1-x}Mn_xTe$ and $Cd_{1-x}Mn_xTe$," *Phys. Rev. B*, vol. 34, no. 10, pp. 6943-6950, 1986.

[20]   R. Fornari and J. Kumar, "Infrared absorption spectra in bulk Fe-doped InP," *Appl. Phys. Lett.*, vol. 56, no. 7, pp. 638-640, 1989.

[21]   X. Wang, C. Chen, A. Liu, R. Wang, and K. Ma, "Effective interband g factors in dilute magnetic semiconductor $Cd_{1-x}Fe_xTe$," *J. Appl. Phys.*, vol. 80, no. 8, pp. 4421-4424, 1996.

[22]   H. Y. Ling, "Theoretical investigation of transmission through a Faraday-active Fabry-Perot etalon," *J. Opt. Soc. Am. A*, vol. 11, no. 2, pp.754-758, 1994.

[23]   A. Yariv, "Coupled-mode theory for guided-wave optics," *IEEE J. Quant. Elec.*, vol. QE-9, no. 9, pp. 919-933, 1973.

[24]   M. Kohtoku, H. Sanjoh, S. Oku, Y. Kadota, and Y. Yoshikuni, "Polarization independent semiconductor arrayed waveguide grating using a deep-ridge waveguide structure," *IEICE Trans. Electron.*, vol. E81-C, no. 8 , pp. 1195-1204, 1998.

[25]   L. B. Soldano and E. C. Pennings, "Optical multi-mode interference devices based on self-imaging: principles and applications," *J. Lightwave Tech.*, vol. 13, no. 4, pp. 615-627, 1995.

[26]   D. G. Hall, "Scattering of optical guided waves by waveguide surface roughness: a three-dimensional treatment," *Optics Letters*, vol. 6, no. 12, pp. 601-603, 1981.

[27]   P. V. Studenkov, M. R. Gokhale, and S. R. Forrest, "Efficient coupling in integrated twin-waveguide lasers using waveguide tapers," *IEEE Photonics Technology Letters*, vol. 11, no. 9, pp. 1096-1098, 1999.